Characterization of Underwater Target Geometry from Autonomous Underwater Vehicle Sampling of Bistatic Acoustic Scattered Fields

by

Erin Marie Fischell

Submitted to the Joint Program in Applied Ocean Science & Engineering
in partial fulfillment of the requirements for the degree of

Doctor of Philosophy

at the

MASSACHUSETTS INSTITUTE OF TECHNOLOGY

and the

WOODS HOLE OCEANOGRAPHIC INSTITUTION

June 2015

Author .....
Joint Program in Applied Ocean Science & Engineering
Massachusetts Institute of Technology
& Woods Hole Oceanographic Institution
March 27, 2015

Certified by .....
Henrik Schmidt
Professor of Mechanical and Ocean Engineering
Massachusetts Institute of Technology
Thesis Supervisor

Accepted by .....
David E. Hardt
Chairman, Committee for Graduate Students
Massachusetts Institute of Technology

Accepted by .....
Henrik Schmidt
Chairman, Joint Committee for Applied Ocean Science & Engineering
Massachusetts Institute of Technology
Woods Hole Oceanographic Institution

Characterization of Underwater Target Geometry from Autonomous Underwater Vehicle Sampling of Bistatic Acoustic Scattered Fields

by

Erin Marie Fischell

Submitted to the Joint Program in Applied Ocean Science & Engineering
Massachusetts Institute of Technology
& Woods Hole Oceanographic Institution
on March 27, 2015, in partial fulfillment of the
requirements for the degree of
Doctor of Philosophy

Abstract

One of the long term goals of Autonomous Underwater Vehicle (AUV) minehunting is to have multiple inexpensive AUVs in a harbor autonomously classify hazards. Existing acoustic methods for target classification using AUV-based sensing, such as sidescan and synthetic aperture sonar, require an expensive payload on each outfitted vehicle and expert image interpretation. This thesis proposes a vehicle payload and machine learning classification methodology using bistatic angle dependence of target scattering amplitudes between a fixed acoustic source and target for lower cost-per-vehicle sensing and onboard, fully autonomous classification. The contributions of this thesis include the collection of novel high-quality bistatic data sets around spherical and cylindrical targets in situ during the BayEx'14 and Massachusetts Bay 2014 scattering experiments and the development of a machine learning methodology for classifying target shape and estimating orientation using bistatic amplitude data collected by an AUV. To achieve the high quality, densely sampled 3D bistatic scattering data required by this research, vehicle broadside sampling behaviors and an acoustic payload with precision timed data acquisition were developed. Classification was successfully demonstrated for spherical versus cylindrical targets using bistatic scattered field data collected by the AUV Unicorn as a part of the BayEx'14 scattering experiment and compared to simulated scattering models. The same machine learning methodology was applied to the estimation of orientation of aspect-dependent targets, and was demonstrated by training a model on data from simulation then successfully estimating the orientations of a steel pipe in the Massachusetts Bay 2014 experiment. The final models produced from real and simulated data sets were used for classification and parameter estimation of simulated targets in real time in the LAMSS MOOS-IvP simulation environment.

Thesis Supervisor: Henrik Schmidt
Title: Professor of Mechanical and Ocean Engineering
Massachusetts Institute of Technology

Biography

Erin Fischell grew up in Fair Haven, NJ and attended High Technology High School in Lincroft, NJ. In high school she first discovered underwater robotics, and travelled to the MATE ROV national championships with ROVs she helped build in 2005 and 2006. Erin went on to Cornell University in Ithaca, NY to study Mechanical Engineering as a part of the class of 2010. At Cornell, she was a Dean's McMullen Scholar, a member of the Sphinx Head Honor Society and received the 2010 Walter Werring Excellence Studies Prize in Mechanical Engineering. With the Cornell University Autonomous Underwater Vehicle Team (CUAUV), she worked on design and construction of 4 AUVs for competition and research. She became team leader for CUAUV in 2008, and led the team to first place finishes at the 2009 and 2010 AUVSI RoboSub competitions. Erin graduated cum laude from Cornell University in 2010 with her Bachelor of Science degree in Mechanical Engineering.

Erin entered the Massachusetts Institute of Technology/Woods Hole Oceanographic Institution Joint Graduate Program in September 2010 with an interest in continuing her work with Autonomous Underwater Vehicles. Her Doctoral research, presented in this thesis, was the development of acoustic payload, vehicle behaviors and processing chains for fully autonomous underwater target characterization using AUVs. The demonstration of this technology with two field experiments was the highlight of her graduate work, and provided the data required for assessing the value of the methodology in the real world. Her current hobbies, used to maintain sanity during the process of completing this thesis, include hiking, cooking, gardening, music, reading, and thread crafts.

Acknowledgments

I would like to first thank my advisor, Prof. Henrik Schmidt, whose advice, support and guidance gave me the resources to complete this work. Thank you especially for suggesting a great thesis topic, helping me understand the acoustics, and giving me the chance to run field experiments to confirm simulation results. I had a great time working with you. I would also like to thank my thesis committee, Dr. James Lynch, Prof. Arthur Baggeroer, and Prof. Franz Hover, for their advice and assistance in turning a set of simulation and experimental results into a cohesive thesis. Thanks also to Pierre Lermusiaux for chairing my thesis defense.

I would like to thank all the members of the Laboratory for Autonomous Marine Sensing Systems that I have had the pleasure to work with during my time here. Special thanks to Toby, who wrote or supported much of the software that made sophisticated vehicle operations possible and who gave me many of the tools needed to build the payload timing system; Steph, whose technical support and mastery of the vehicle idiosyncrasies helped make the BayEx'14 experiment a success and whose friendship and advice sustained me from day one; Sheida, my study buddy, confidant and sanity checker for acoustic simulation; and Thom, who seemlessly took over Steph's operational responsibilities for the Massachusetts Bay experiment. Alon, Arthur, Nick and Tom: thank you for great conversations and an interesting boondoggle into surface vehicles. Thank you to Dr. Michael Benjamin for writing and maintaining the IvP Helm, used extensively to complete this thesis, and to Dr. Arjuna Balasuriya for early advice on AUV operations in SWAMSI. Lastly, thanks to Geoff Fox for providing organizational and administrative support.

I would like to acknowledge NSWC in Panama City, Florida, for all their help in organizing and conducting field trials for the GOATS'14: Adaptive and Collaborative Exploitation of 3D Environmental Acoustics experiment (referenced as BayEx'14 in this thesis), as well as for the use of rib boats and the PCS-12. In particular, I would like to thank Joe Lopes, Paul Wray, and Nicholas Abruzzini at NSWC for supporting the experiment and helping make everything happen in time. Especial thanks to Kevin Williams and his group at APL-UW for providing and setting up source and targets for our data acquisition during BayEx'14.

Bluefin Robotics was instrumental in the success of the experimental work described in this thesis and provided operational support for both experiments. For the Massachusetts Bay experiment, they provided the target and the ship that made data collection on different target aspects possible.

I would like to acknowledge the sponsors that funded my tuition, stipend, and research, including National Science Foundation Graduate Research Fellowship under Grant No. 0645960, The U.S. Office of Naval Research (ONR) under the GOATS'08 (N00014-08-1-0013), GOATS '11 (N00014-11-1-0097), SWAMSI (N00014-08-1-0011), and GOATS '14 (N00014-14-1-0214) projects, and APS under DSOP Subtasks 1.3 (11-15-3352-005) and 2.3 (11-15-3352-215).

I owe thanks to my friends near and far, for giving me good times and good advice over the last few years. You kept me laughing and thinking, and reminded me to get away from

my computer once in a while and talk to real people. I would also like to acknowledge all the wonderful teachers I have had through the years: you gave me the tools I needed to succeed.

Finally, I would like to thank my family for their continued love and support. Mom and Dad, thank you for teaching me to love building things, for your complete confidence that I would succeed, and for two lifetimes of systems engineering advice. Jen, thank you for helping me learn to explain all this to a non-engineer. Most of all, thank you to my husband Sam, whose love, understanding and good sense kept me buoyed and on track through the ups and downs of my PhD work. I can't wait for our next adventure together!

Contents

List of Figures

List of Tables

Chapter 1

Introduction

1.1 Motivation

A growing application for Autonomous Underwater Vehicle (AUV) technology is the localization, classification and mitigation of underwater hazards in shallow harbor environments. The classification problem has attracted particular attention in recent years with the development of visual and acoustic AUV-based sensors for remote data collection. Because visual inspection of targets can be difficult or impossible in murky harbors and requires precise target localization, acoustic sensors such as sidescan sonar and synthetic aperture sonar (SAS) are used more extensively for AUV-based Mine Countermeasures.

At the current level of technology, these techniques can provide rich images of targets and the environment but produce data that are difficult to use for real-time target classification. Sidescan sonar systems are generally too high frequency for buried target localization and classification. SAS images are usually computed in post-processing so that navigation corrections may be applied [1]. The current operational paradigm for the use of both technologies requires a human in the loop for expert image interpretation. In addition to these challenges to fully autonomous real-time classification of data from these systems, the sensors themselves are too expensive to be practical in multi-vehicle operations.

To achieve plausible, real-time AUV-based target classification that is expandable to distributed vehicle networks, two key advancements are required: an inexpensive sensing payload and a classification method that can be run in real-time on an AUV computer using onboard processing of sensor and navigation data. The advantages of such a sensing system would be the ability to deploy multiple AUVs to carry out the target localization

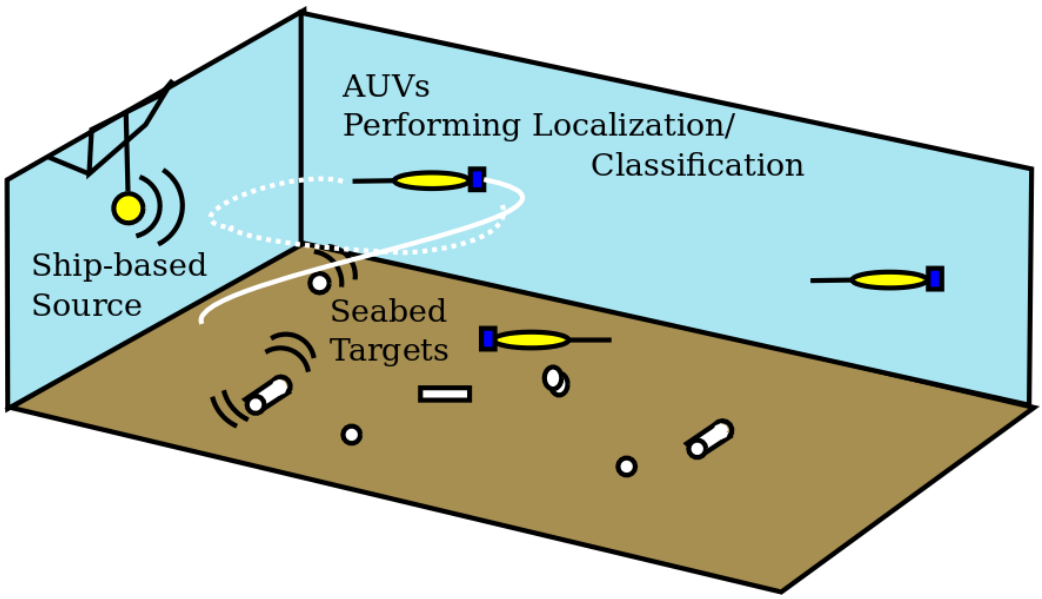

Figure 1-1: Multi-vehicle operation mission, where a fixed source insonifies a target field while multiple AUVs sample the bistatic scattering fields around various targets.

and classification missions with immediate classification and confidence estimates to inform prosecution decisions without having to recover and redeploy vehicles.

The goal for this thesis was to develop a payload and processing chain for target classification using only bistatic acoustic data collected on an AUV's linear hydrophone nose array cut for low-frequency acoustic sensing (1-15kHz). The bistatic configuration and hydrophone array were selected to limit sensing system cost: in the multi-vehicle scenario, a fixed acoustic source insonifies a target field while multiple vehicles with inexpensive payloads collect bistatic scattering data around targets, as shown in Figure 1-1.

This thesis presents the AUV payload required to perform bistatic acoustic data collection, real-world bistatic acoustic data sets collected around spherical and aspect-dependent seabed targets with that payload, and a machine-learning methodology that utilizes bistatic angle dependence of amplitude features from the scattered field to classify target shape and estimate the orientation of aspect-dependent targets. This approach was highly successful for the classification of spheres versus cylinders and for the estimation of target orientation. The results from real and simulated data for simple target geometries suggest that using features of the bistatic acoustic scattering radiation pattern for target classification in real time on AUVs is a plausible solution to the real-time target classification problem and warrants further study.

1.2 Historical Background

1.2.1 Bistatic Scattering from Seabed Targets

The vast majority of target scattering literature is focused on backscattering data from monostatic sensing. However, there is a small body of theoretical and experimental work looking at the bistatic scattering problem.

Bistatic scattering theory and models have been developed for simple target geometries (sphere, spheroid, cylinder) in simple environments. The theoretical and numerical work on bistatic scattering from spheres includes that by Gaunaurd and Uberall [2], which discusses the free field bistatic form function of spherical targets and gives an example numerical calculation. Hackman and Sammelmann describe the theoretical scattering from a spheroidal target in an ocean waveguide, and include numerical results for the bistatic case [3]. While the backscatter from finite cylinders for various aspects has been described analytically [4] [5], the additional dimensionality of the bistatic problem means that the approach to finding the bistatic scattered field is numerical. The analytical bistatic sphere scattering formulation and Rumerman's scattering model for cylinders [6] are used in the OASES-SCATT acoustic simulation package developed by Schmidt and Lee [7] [8]. This acoustic package was used to explore effects of environment, bottom composition and target geometry on bistatic acoustic fields in Lee's thesis, "Multi-static Scattering of Targets and Rough Interfaces in Ocean Waveguides" [9]. Virtual scattering experiments using the OASES-SCATT scattering simulator influenced this work by showing clear distinctions in bistatic target scattering field characteristics.

Most of the limited experimental work on bistatic target scattering has been conducted in the small scale, in water tanks and test ponds. For example, Baik, Dudley, and Marston conducted an experiment where they looked at the bistatic response of different cylinders in a test tank for the purposes of holographic imaging [10]. Kargl et. al. looked at the bistatic scattering response of aspect-dependent targets in a test pond as a part of the PondEx10 experiment [11].

These experiments used moveable arrays that are not easily adapted to a harbor environment, and there have been very few attempts to collect bistatic acoustic data in situ with AUVs. The GOATS'98 experiment is a rare example of a successful AUV-based bistatic scattering experiment: it included an AUV with a nose array, and produced data on the

bistatic scattered fields off of fully buried, partially buried and proud spheres. Lepage and Schmidt [12] and Edwards et. al. [13] describe the AUV experiment and using the array data for Synthetic Aperture Sonar imaging. Synchronization was achieved using a vehicle-based acoustic signal to trigger the source. The data was collected using lawnmower patterns through the target field, which had the disadvantage of giving non-uniform data quality and few data with the array at broadside to each target. The significant advances in many areas since 1998 made a new experiment to collect bistatic data with an AUV valuable. These areas of tremendous advancement include the computational power for real-time target tracking and classification, adaptive autonomy to allow more efficient data collection, the existence of small, low-power, high-accuracy clocks for synchronization timing, and vehicle navigation with less than 0.5% drift per distance travelled.

1.2.2 Target Classification

The more recent literature on using AUVs for Mine Countermeasures classification tasks focuses on the use of monostatic and imaging techniques, often in high frequency. Examples of these techniques include Synthetic Aperture Sonar (SAS) and sidescan sonar. These methods have been shown to be effective for many target types and circumstances, but the expense of developing and deploying these systems as well as the difficulty of using the resulting data for real-time classification justifies investigation into alternative methods. The AUV-based SAS work does not utilize the true bistatic field, but uses an array and source together on an AUV to get a synthetic aperture, simplifying navigational constraints. There are very few examples of using a SAS imaging approach with bistatic data: it was attempted by Edwards et. al. as a part of the GOATS'98 experiment [13] and discussed in a paper by Dudley and Marston, for experimental data collected using a rail source and receiver [14].

Monostatic target classification using probabilistic methods is discussed in [15], which attempts to classify targets using multiaspect backscatter, wave-based signal processing and Hidden Markov Models (HMMs). In this method, a model is trained and then used to classify new targets. This work demonstrates an empirical model-based approach to target classification with a geometric feature space, though methods described use only backscatter data, utilize a different aspect of the acoustic signal, and do not use a machine learning approach to the classification.

Several machine learning based target classification methods using backscatter information and a frequency or time-frequency analysis of the target return have been published. Kaminsky and Barbu looked at classification of buried cylindrical targets (such as cables) using simulated data and a discriminant analysis method applied to a time-frequency image [16]. Malarkodi et. al. investigated using Neural Networks for classification of target type using a features space that was a statistical representation of the target return power spectrum for a 40-80kHz Linear Frequency Modulation (LFM) chirp [17]. These techniques differ from those described in this thesis in that they use features that include temporal or phase information and only look at monostatic data.

1.3 Contributions

There are two important contributions of this thesis. The first is the bistatic data set collected during the BayEx'14 and Massachusetts Bay experiments and the development of the AUV payload for collecting that data. The second is the use of bistatic angle dependence of scattering amplitudes with a machine learning methodology for target characterization, which was demonstrated on simulated and real bistatic scattering data for the classification spheres versus cylinders and for the estimation of rotation angle for aspect-dependent targets and sand ripple fields.

Initial simulation studies provided the inspiration for using the relationship between scattering amplitude and bistatic angle as a basis for target classification. Chapter 2 explains some of the basic principles of target scattering, with supporting examples from simulation.

As discussed in the Historical Background section, very few bistatic scattering experiments have been conducted in real harbor environments with AUVs. The challenges to a successful AUV-based bistatic scattering experiment included timing, navigation, and collecting uniform-quality data. Chapter 3 describes the acoustic payload designed and built for precision timing of data acquisition on the AUV *Unicorn* for bistatic scattering experiments and the characterization experiments undertaken to ensure that timing requirements were met. Chapter 4 then explains the combination of hardware, signal processing, and vehicle behaviors used to collect dense, high-quality bistatic scattering data sets around spherical and simple aspect-dependent targets during the BayEx'14 and Massachusetts Bay experiments using the AUV *Unicorn*. The resulting data sets are presented and compared

to predicted scattering results from simulation. Chapter 5 explains the machine learning classification methodology developed to use the geometric pattern of bistatic scattering amplitudes to distinguish spherical from cylindrical targets. The results from applying this methodology on real and simulated data are then described, including features space and parameter selection algorithms.

Chapter 6 describes the extension of the machine learning classification methodology to regression problems for the estimation of cylinder rotation angles and seabed ripple field anisotropy.

Finally, Chapter 7 presents the conclusions of this thesis and suggestions for future work.

Chapter 2

Object Scattering In The Ocean

2.1 Overview

When a target on the ocean bottom is acoustically insonified, the target re-radiates the signal (Figure 2-1). This reradiation consists of multiple time delayed echos that interfere in the frequency domain.

For the problem of classifying underwater targets in real time using data collected on an AUV, it was critical to identify features that were robust to several meters of error in vehicle location, source location, and target location. The combined navigational uncertainty, plus the computations limitations for data processing on an AUV, made using sensitive time and phase information for target classification impractical. While these features are frequently used for SAS imaging, they would be difficult to use in real time on a bistatic AUV system because of the navigation errors inherent in an AUV system.

The interference of the time-delayed echos from target scattering result in frequency-dependent minima and maxima in the bistatic radiation pattern from the target. These scattering radiation patterns are distinct for different target types and are mostly dependent on the bistatic angle of an amplitude measurement, showing range and depth independence over meters or tens of meters. Bistatic angle is the angle between the source and the receiver relative to the target. The concept for the classification techniques discussed in this thesis is that these interference patterns in a given frequency band are stable and can be used to characterize seabed targets.

The technology required for getting data on the bistatic radiation pattern is an AUV with a linear hydrophone nose array, a data acquisition system, and signal processing software to

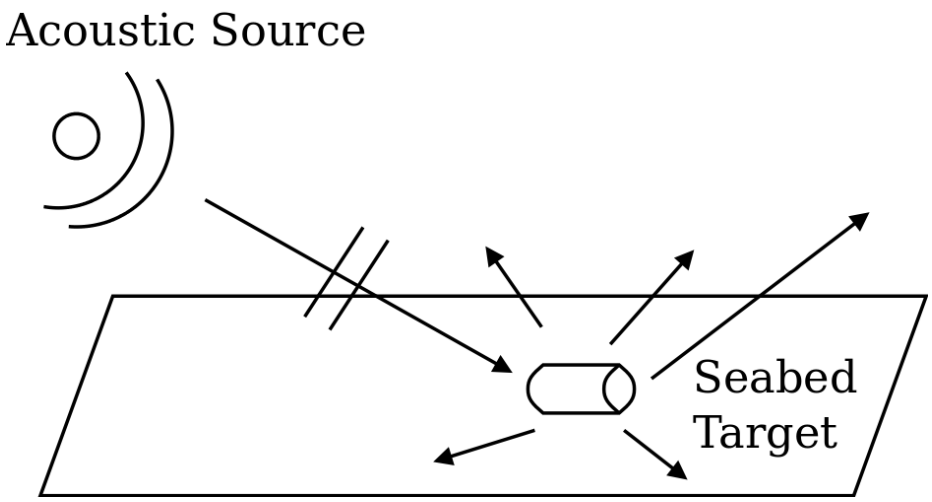

Figure 2-1: Insonification of a target results in acoustic scattering, as the target re-radiates the signal in multiple echos that interfere to form the radiation pattern exploited by the characterization techniques discussed in this thesis.

calculate target scattering amplitude as acoustic data is collected around a target. Imaging techniques are not required, as the dependence of scattering amplitude on bistatic angle can be analysed directly.

2.2 Modelling Target Scattering with Wavenumber Integration

The wavenumber integration computational approach involves decomposing the acoustic field in frequency and wavenumber, which makes it a good technique for propagation of target scattering fields, as the dependence of the scattering radiation pattern is in the frequency domain. While the models do not include multiple scattering or elastic scattering effects, real scattering data showed the simulations to be generally effective at predicting the radiation pattern for different targets and environments.

The OASES-SCATT scattering simulation package was used extensively in this thesis for modelling target and bottom roughness scattering fields [7] [8]. This simulation package uses the single scattering approximation [18], assumes an incident plane wave, and approximates the target as a virtual point source with a specific radiation pattern[9]. The single scattering approximation could be insufficient for accurately modelling temporal features of target scattering, but is adequate for modelling minima and maxima of the interference pattern,

of greatest interest in this thesis [7]. The plane wave approximation is appropriate for the scenarios considered here as the source is in the far field from the target. Effects due to layers in the medium are taken into account in the wavenumber integration approach, so waveguide effects are included in the resulting models.

The simulation package uses 2-D wavenumber integration to propagate a plane wave from the source to the target location. The equivalent virtual source radiation pattern is then calculated for the target. For spheres, a volume scatterer approximation is used to directly calculate the scattered pressure field from the incident pressure and boundary conditions. Rumerman's scattering model [6] is used to calculate the effective source function for finite cylinder shells. 3-D wavenumber integration is then used to compute the full 3-D scattering field from the spectral radiation pattern of the target at a set of ranges and depths for the specified environment. The final output includes the azimuthal Fourier orders for a series of ranges and depths from the target. In addition to target simulation, the scattering package can model rough bottom scattering. This was used for modelling of anisotropic sand ripple field bottom scattering to provide a second example of regression for parameter estimation Section 6.3.

To interface the scattering simulation package with classification and regression software, the custom AutoGen code was written. This code has a database back end that allows reconstruction of all simulation experiments based on input parameters, and was used for automatic generation of scattering fields based on target, source and environment configuration. Appendix C describes this code in detail.

2.2.1 Target Scattering

The target scattering simulator was used to generate scattering models for the simple target geometries used in this thesis. The assumptions about the target radiation patterns that underlie this thesis were based on simulation data. The most important of these are the persistence of radiation pattern features between ranges and depths for a given frequency. Figure 2-2 shows the simulated scattering amplitudes for spherical and cylindrical targets in a 6.5m deep waveguide for multiple depths, generated using the BayEx'14 configuration shown in Appendix A. The source is 3m deep, 8kHz, and 60m from the target. The simulated water depth is 8m, with a mud bottom over sand.

For both target types, the clearest and most robust features are the bistatic angles of

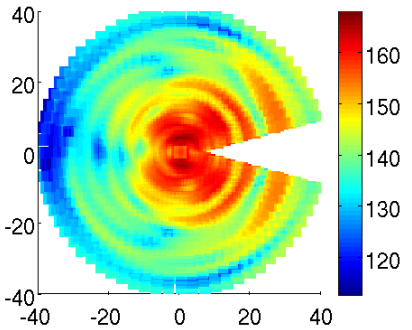

(a) Simulated scattered field amplitudes for sphere, depth=1m.

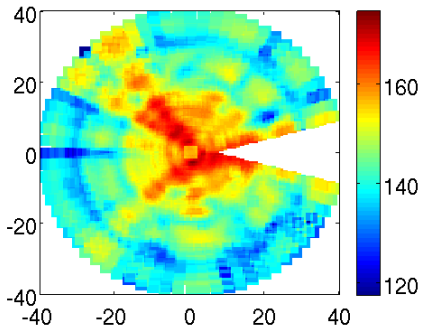

(b) Simulated scattered field amplitudes for cylinder, depth=1m.

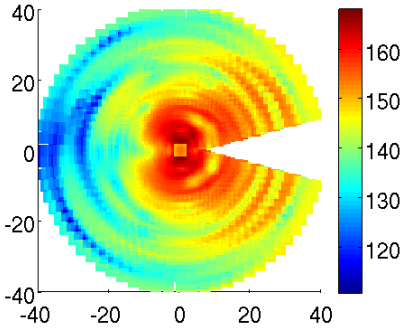

(c) Simulated scattered field amplitudes for sphere, depth=2m.

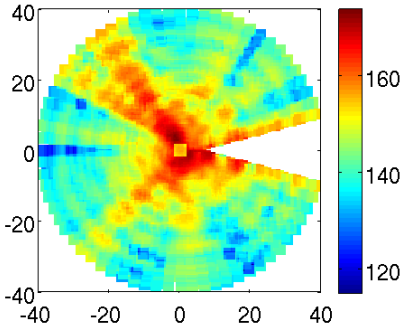

(d) Simulated scattered field amplitudes for cylinder, depth=2m.

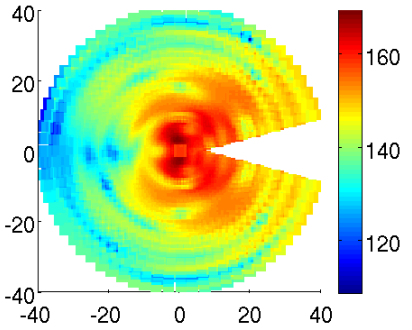

(e) Simulated scattered field amplitudes for sphere, depth=3m.

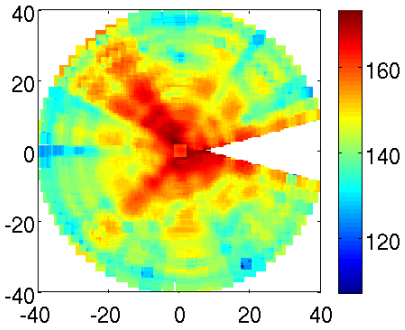

(f) Simulated scattered field amplitudes for cylinder, depth=3m.

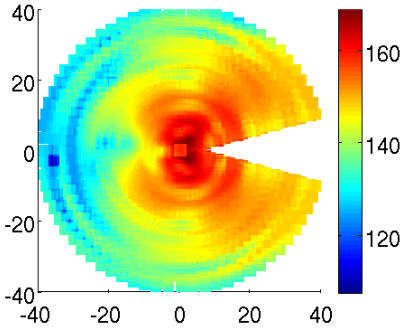

(g) Simulated scattered field amplitudes for sphere, depth=4m.

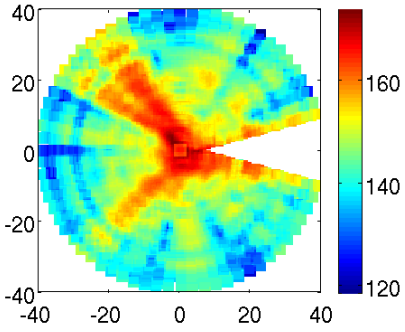

(h) Simulated scattered field amplitudes for cylinder, depth=4m.

Figure 2-2: Simulated scattered field data at several depths.

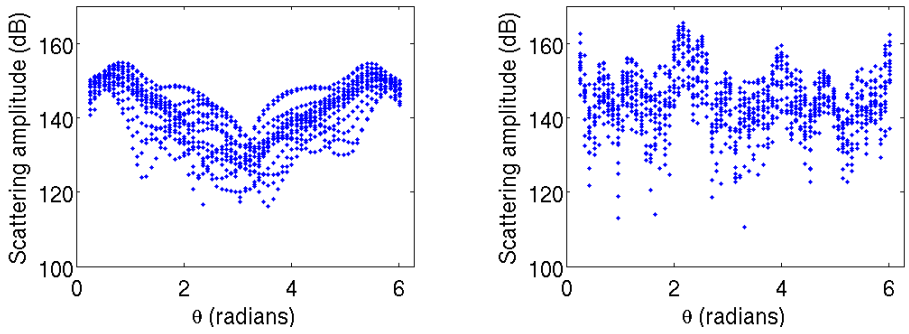

(a) Dependence of scattering amplitude between ranges of 20 and 40m for spherical target.

(b) Dependence of scattering amplitude between ranges of 20 and 40m for cylindrical target.

Figure 2-3: Simulated scattering amplitude dependence on angle θ for spherical and cylindrical targets. θ is calculated by setting the target at $(0, 0)$ and the source at $(-60, 0)$ such that the source is at 180^o.

amplitude minima and maxima in the scattered field. These features are only slowly changing with depth and generally consistent in range from the target. The lobes of the radiation pattern are also meters wide in the far field. Figure 2-3 shows the dependence of scattering amplitude on bistatic angle, θ, across all depths and 20-40m range for the sphere and cylinder case. The general location of minima and maxima within the pattern remains consistent with different depths and ranges. These properties would make sensing of the overall radiation pattern robust to several meters of AUV navigation error. Utilizing scattering amplitude information has the additional advantage of being more robust to noise and interference than temporal or phase information. Figure 2-4 shows the intensity-averaged radiation pattern for spherical and cylindrical targets versus bistatic angle. Represented in this fashion, the difference between the two target types is very clear, providing a good basis for AUV-based target classification.

The aspect-dependence of cylindrical targets also causes distinct features in the bistatic angle dependence of the radiation pattern. Figure 2-5 shows several cylinder rotations to aspect angle γ relative to the source and the resulting simulated radiation patterns versus azimuthal angle relative to the source. The location of minima and maxima shift with aspect angle, suggesting that the orientation of a cylinder could be estimated using a regression model.

2.2.2 Ripple Field Scattering

Similarly, the scattered fields from anisotropic bottom ripple fields have their most major features in azimuth, rather than range and depth. Figure 2-6 shows the impact on the radiation pattern of the anisotropy angle. Like with cylinder orientation, the radiation pattern shifts consistently in a way that suggests the anisotropy angle could be estimated using a regression model. These scattering simulations assumes a 100m waveguide with a source at 30m depth, 100m from the insonified bottom patch. Within a 20-50m set of ranges and 20m of depth, the location and strength of minima and maxima are consistent and persistent. The mean or median scattering amplitude dependence on anisotropy angle is distinctive.

2.3 Conclusions

Simulation experiments using a wavenumber integration-based scattering simulation package suggested that the dependence of target scattering amplitude on bistatic angle provides robust features that could be used for target characterization. The use of these features, rather than time or phase-based information, loosens navigation accuracy requirements to what is plausible on an AUV. Additionally, target scattering amplitudes can be calculated directly from acoustic data collected on a line array carried by an AUV. Utilizing the dependence of target scattering amplitude on the bistatic angle of sampling does not require sophisticated imaging techniques for classification, and could provide a basis for onboard target characterization.

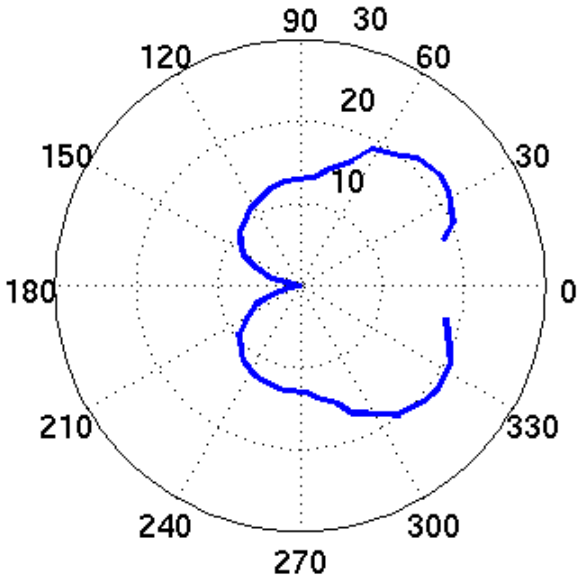

(a) Intensity-averaged radiation pattern, averaged over range and depth, for spherical target.

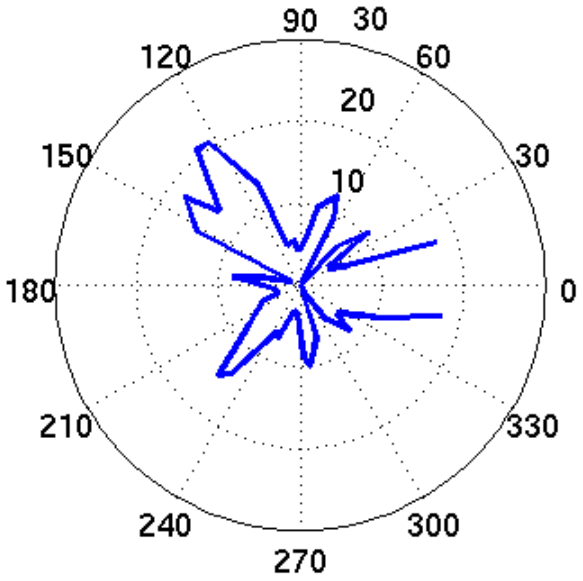

(b) Intensity-averaged radiation pattern, averaged over range and depth, for cylindrical target.

Figure 2-4: Simulated radiation patterns for spherical and cylindrical targets. The pattern was calculated by taking the mean intensity in each 5 degree azimuthal bin across range and depth (20-40m range, 1-4m depth), converting to dB and subtracting the minimum intensity. These polar plots are shown as looking from above on the target, with the target at (0,0) and the source at r=60, $\theta = 180^o$.

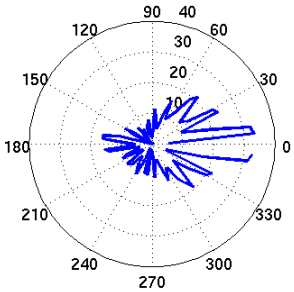

(a) $\gamma = 0^o$.

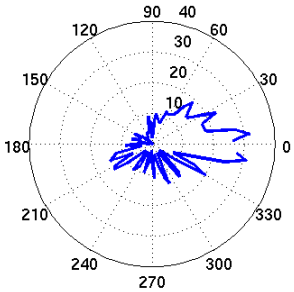

(b) $\gamma = 15^o$.

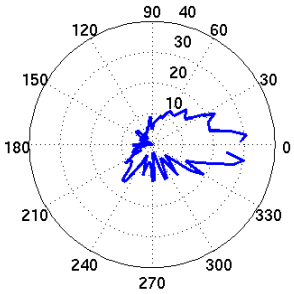

(c) $\gamma = 30^o$.

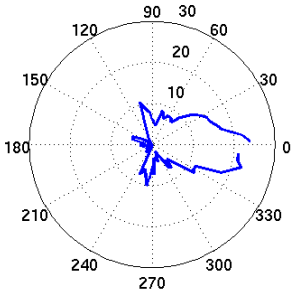

(d) $\gamma = 45^o$.

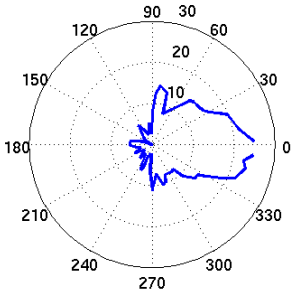

(e) $\gamma = 60^o$.

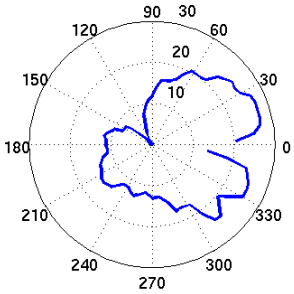

(f) $\gamma = 90^o$.

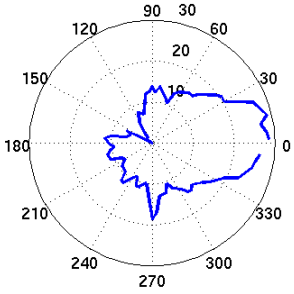

(g) $\gamma = 120^o$.

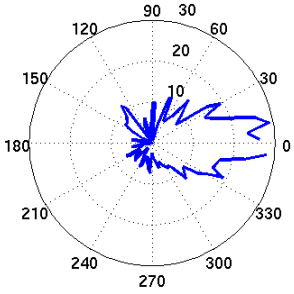

(h) $\gamma = 150^o$.

Figure 2-5: Mean radiation patterns for different cylinder rotations. The location of minima and maxima within the patterns shift with the angle γ.

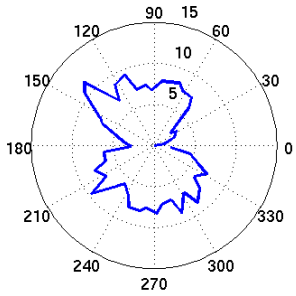

(a) Simulated scattered field amplitudes for anisotropic ripple field with $\gamma = 0^o$.

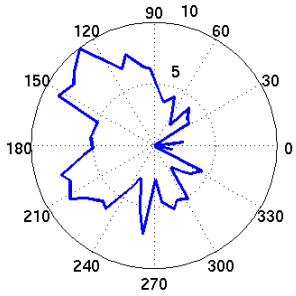

(b) Simulated scattered field amplitudes for anisotropic ripple field with $\gamma = 15^o$.

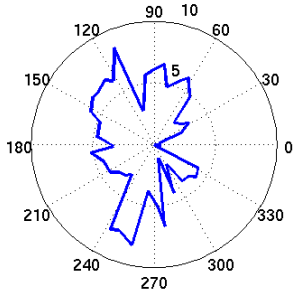

(c) Simulated scattered field amplitudes for anisotropic ripple field with $\gamma = 30^o$.

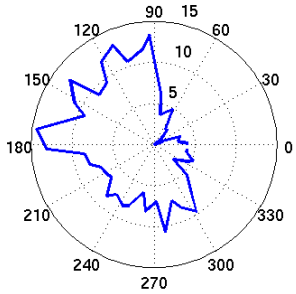

(d) Simulated scattered field amplitudes for anisotropic ripple field with $\gamma = 45^o$.

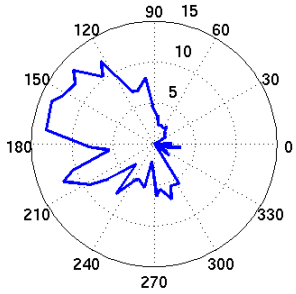

(e) Simulated scattered field amplitudes for anisotropic ripple field with $\gamma = 60^o$.

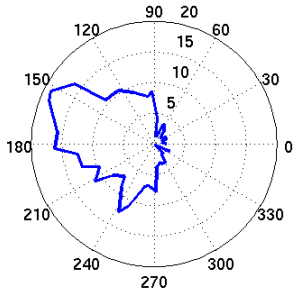

(f) Simulated scattered field amplitudes for anisotropic ripple field with $\gamma = 75^o$.

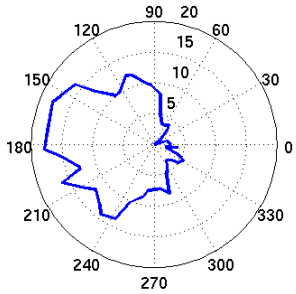

(g) Simulated scattered field amplitudes for anisotropic ripple field with $\gamma = 90^o$.

Figure 2-6: Intensity-averaged radiation patterns for acoustic scattering from anisotropic rough bottom patches with varying values of $\gamma = 45^o$, depths 10-50m, ranges 20-50m.

Chapter 3

Acoustic Payload

To show that reliable bistatic scattering data collection by an AUV was feasible, an acoustic payload had to be designed and built that solved the problem of time synchronization between the acoustic source and vehicle. There were a number of obstacles to achieving the required data logging accuracy. First, while many surface-based systems use global position systems (GPS) to synchronize a local clock to the satellite pulse-per-second (PPS) signal, this microsecond-precise clock was not available underwater. Second, the computer clock, even synchronized via Network Time Protocol (NTP) to a precise PPS signal, has accuracy only in milliseconds, and therefore could not be used to trigger data collection when desired accuracy was in microseconds. Third, delays introduced by analog filters and analog-to-digital conversion were in the tens to hundreds of microseconds, and had to be taken into account in system calibration to achieve sufficient system accuracy. This chapter presents the implementation of an accurate and precise data acquisition system for bistatic acoustic data collection on an AUV using off-the-shelf hardware and a set of test routines for calibration. First, the application is explained and the commercial off-the-shelf hardware is described. The payload architecture is then laid out, including hardware and software implementation needed for a functioning precision-timed data acquisition system. Next, the test procedures used in the characterization and calibration of the system to eliminate system delays are explained. Finally, the results and conclusions, including total system accuracy, are reported.

3.1 Background

In general, one of the greatest challenges to remote sensing in the ocean is the problem of maintaining adequate time synchronization between the shore and any submerged system [19]. Similarly, one of obstacles to the practical collection and use of bistatic scattering data was vehicle-source time synchronization. The absolute start time of each acoustic data file had to be known so that the target scattering signature could be identified within the time series. This required synchronizing the firing schedule of the acoustic source with the data acquisition system on-board the vehicle. There were two types of accuracy required of the data acquisition system for this acoustic experiment: accuracy in arrival time of a contact and accuracy in phase between channels in the hydrophone array. The desired resolution in range for this system was 0.1m, which corresponds to a 70 microsecond difference between the true and estimated time that the file begins recording. Less accurate time synchronization would results in poor resolution of target range, which could cause misestimation of target scattering strength by onboard signal processing. Similarly, the 16 channels need to start recording at the same time so that the phase shifting between the channels is introduced by the signal directionality rather than recording delays. The maximum permissible delay between channels in the system was one percent of a wavelength amount, approximately 1 microsecond at 9kHz, to ensure that phase shifts introduced by recording delays did not affect beamforming operations used to calculate the arrival direction of the signal.

3.2 Payload Architecture Overview

The acoustic payload used in the AUV *Unicorn* for this experiment consisted of the 16 element linear nose array used to collect acoustic data, a preamplifier for filtering and amplification on the raw signal, two 24DSI12-PLL data acquisition boards (DABs) [20] for analog-to-digital conversion and an Advantech 3363 computer [21] with Intel Atom dual core processor for data logging, signal processing, and vehicle autonomy. A Quantum Chip Scale Atomic Clock (CSAC) SA.45s provided an accurate on-board time reference, and was synchronized using the time reference from a Garmin 15xLW GPS while on the surface. Figure 3-1 shows how these parts of the data acquisition and timing system interact. The analog signals from the 16 elements of the hydrophone array were filtered and amplified by the preamplifier, then synchronously recorded as 24-bit digital by the DABs. This recording

was triggered by the rising edge of the CSAC PPS signal. The digital data is sent in the form of a first-in-first-out (FIFO) buffer over PCI bus to the Advantech 3363 computer, which ran a daemon that controls the DABs and logs the data to a timestamped file.

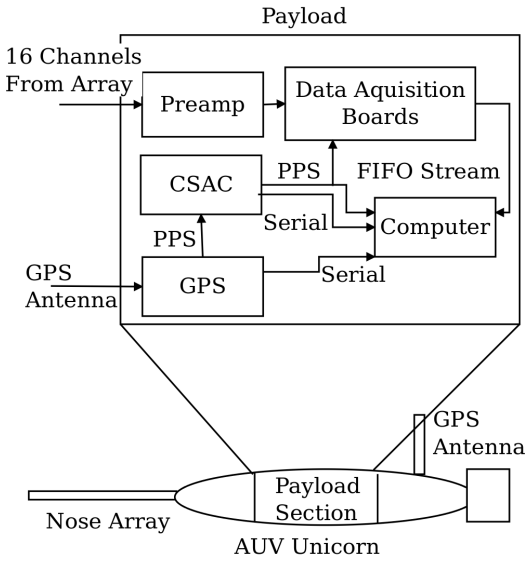

Figure 3-1: Block Diagram of the data aquisition and timing system.

3.2.1 Real-Time Clock Synchronization

The Quantum CSAC SA.45s is a high-precision, low-cost, low-power clock well suited for underwater sensing platforms, including autonomous underwater vehicles. A CSAC, properly aged, can be considered a reliable time source with precision limited by its drift rate and an accuracy limited by the accuracy of the global time source it uses as a synchronization reference. The aging rate of the CSAC is 3.0E-10/month [22], which far exceeds the requirements of this application, where vehicles are deployed for less than a day at a time.

A CSAC and CSAC development board were integrated with the computer and acoustic data acquisition systems in the AUV payload to provide a precision pulse-per-second time reference while the AUV was submerged. The addition of a Garmin 15xLW GPS to the payload, connected to an external GPS antenna, provided a time of day and PPS reference for CSAC synchronization on the surface. Synchronization set the rising edge of the CSAC Board's PPS output to match the rising edge of the GPS PPS so that the start-of-second time reference was the same.

This synchronization between the global time reference and the local time reference

was managed using a custom daemon, which ensured that the vehicle and source time references were the same. This daemon had two critical functions: to perform GPS-CSAC synchronization on startup (if satellites are available), and to provide a GPRMC NMEA message to the vehicle computer. The NMEA sentence was used by the generic NMEA GPS Receiver (reference clock 20 [23]) for setting the LinuxPPS [24] reimplementation of the NTP server on the computer. Since the timing of the recording relative to the start of the second was known, if the computer clock was on the correct second when the data was recorded the file's timestamp was correct.

A backup power system for the CSAC was built so that the system could remain continuously on. This was important because the CSAC's performance improves as it ages [22]. Four hot-swap circuits provided automatic switching between three power sources: an on-board battery pack containing 3 AA batteries, the regular vehicle power source, and an externally accessible CSAC-only 5V power line. In ordinary operations, the vehicle could be shut off and the external CSAC power then connected without opening the payload or removing it from the vehicle. The battery pack, which lasts for more than 24 hours as the only power source, kept the CSAC running during this changeover.

3.2.2 Data Acquisition

To achieve the level of accuracy in time synchronization required by this experiment, data recording and logging had to properly implemented, using the CSAC PPS as a hardware trigger. This was necessary because NTP provides, in the best-case, 1 millisecond accuracy due to the drift in the real-time clock and the general delays in a non real-time operating system.

8 channels from the preamplifier passed into each of the system's two DABs. These boards converted the analog voltages into 24 bit digital data at a sampling rate of 37500Hz, and wrote the resulting binary data to the PCI bus FIFO buffer to be read on the payload computer.

The DABs were configured to run synchronously across all channels and to use the GPS lock feature. This meant that all channels were recorded at the same time, such that the first 8 samples in the FIFO buffer correspond to the voltage level received on 8 elements in the same time bin. GPS lock mode guaranteed that exactly the configured samples per second were recorded each second, re-setting the lock state if there was a drift of more than

one sample and adding or subtracting a sample if a sample drift occurred. In this mode, after 3-5 seconds to confirm that a PPS signal was present, the buffer on each DAB was cleared and recording began on the rising edge of the PPS signal. Each second thereafter, the rising edge of the PPS signal was used to confirm that the number of recorded samples matched the desired sample rate. The bytes read by the computer from the DABs were tracked and the buffer never allowed to overflow so that the sample corresponding to the start of each second was known.

This sampling method made on-the-second data recording possible. Each second, the start of the data recording corresponded to the rising edge of the CSAC PPS signal used for GPS lock on the DABs. When the CSAC PPS signal was synchronized with the GPS PPS signal, this resulted in the first sample of each data recording corresponding to the time that the ping was sent out from the acoustic source.

3.3 Delay Characterization Methodology

The payload system, as described, would have resulted in precise data acquisition, but had accuracy limitations due to timing lags introduced by analog and digital systems. The analog filters in the preamplifier introduced some delay into the system, as did the analog-to-digital conversion in the DAB. These delays changed the estimated range to the source and targets, and were on the order of tens to hundreds of microseconds. To build a data acquisition system that was both precise and accurate, these delays had to be quantified so that they could be incorporated into data recording timestamps. Two sets of experiments were undertaken to characterize these delays: in the first, the magnitude of the delays was estimated using a PPS signal, and in the second a constant waveform (CW) was used to get a more precise estimate of the delays using phase. Additionally, the manufactuer claim of synchronous data acquisition was tested between channels on the DABs, as introduced lag between channels could significantly affect the phase information in the signal. These characterization steps resulted in estimates for analog delay, digital delay, and between-channel recording delay. Analog and digital delay estimates were used to calibrate the system by adjusting the time stamp on each recording. To further improve on this calibration, a method was developed for dynamically estimating the digital delay.

Table 3.1 shows the timing variables used to describe the system characterization. τ

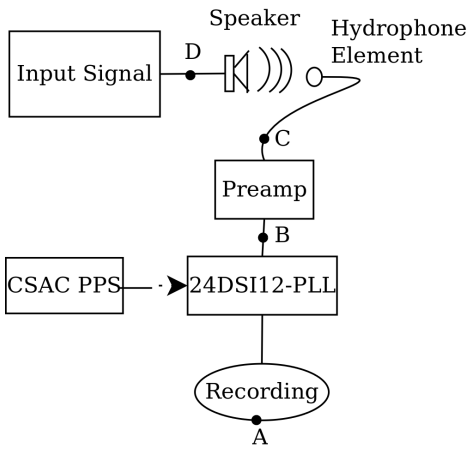

Figure 3-2: Experimental setup with test points.

variables describe delays, x variables represent time series data, k constants and ϕ phases. Subscripts indicate the location of measurements (either in reference to Figure 3-1 or channel) or are descriptive of a calculated quantity. Estimated quantities from measurements are indicated with a tilde, for example $\tilde{\tau}_{analog}$ would represent the estimated value of τ_{analog}.

An accurate estimate of the propagation time, τ_{prop}, was necessary for successful target localization in the bistatic scattering experiment. However, when the onboard signal processing chain estimated a target's location, it could not directly measure the value of τ_{prop}. Instead, it calculated the value of τ_A, the delay observed in the recording from the DAB. Three delays contributed to τ_A: the actual propagation delay τ_{prop}, the analog delay introduced by analog filtering in the preamplification stage τ_{analog} and the digital delay introduced by analog-to-digital conversion in the DABs, $\tau_{digital}$.

$$\tau_A = \tau_{prop} + \tau_{analog} + \tau_{digital} \tag{3.1}$$

One of the important factors in the payload implementation was therefore system calibration so that the propogation delay could be estimated from the value of τ_A such that the range resolution requirements were exceeded. In the final system, the estimated value of propagation delay, $\tilde{\tau}_{prop}$, had to be be within $70\mu s$ of the actual propagation delay.

$$|\tilde{\tau}_{prop} - \tau_{prop}| < 70\mu s \tag{3.2}$$

Table 3.1: Timing characterization variables

ϕ_0	Phase of constant waveform signal recorded on channel 0.
ϕ_1	Phase of constant waveform signal recorded on channel 1.
ϕ_A	Phase of a constant waveform signal at point A.
ϕ_B	Phase of a constant waveform signal at point B.
ϕ_C	Phase of a constant waveform signal at point C.
ϕ_D	Phase of direct input constant waveform signal.
τ_{analog}	Analog delay, introduced by pre-amplification.
$\tau_{digital}$	Digital delay, introduced by analog-to-digital conversion in the DABs.
$\tau_{digital,d}$	Dynamically estimated digital delay.
τ_{prop}	Propagation delay, introduced by the signal propagation between sound source and hydrophone element.
$\tau_{channel}$	Time delay between adjascent channels, introduced by the synchronous data recording on the DABs.
τ_A	Arrival delay of the signal at point A, includes propagation, analog and digital delays.
τ_B	Arrival delay of the signal at point B, includes propagation and analog delays.
τ_C	Arrival delay of the signal at point C, includes propagation delay.
k_{cal}	Calibration constant, used to eliminate mean analog and digital delays from the system.
$k_{cal,d}$	Calibration constant, calculated using dynamically estimated digital delay.
x	Time series recorded using Delta M44 audio card.
x_B	Time series of a recorded signal from point B.
x_C	Time series of a recorded signal from point C.
x_D	Time series of direct-recorded PPS signal.

That is, the shift in arrival time as the signal passes through the analog and digital systems had to be less than 70 μs after calibration to estimate analog and digital delays.

Figure 3-3 shows a visualization of the accumulating propagation, analog and digital delays as a PPS signal passes through the system from point D to C to B to A. In Figure 3-3a, the input PPS signal at point D is shown. The rising edge of this signal corresponds to the start-of-second reference at the acoustic source and onboard the AUV. Figure 3-3b then shows the normalized signal received at Point C. At this point, the signal has been delayed

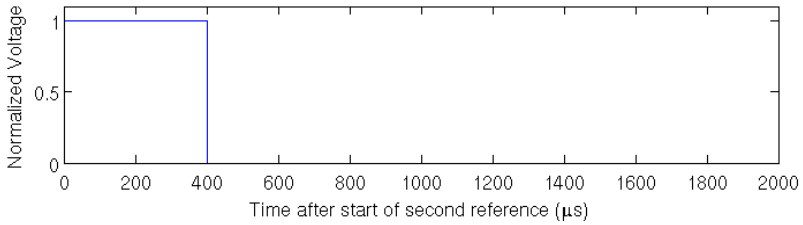

(a) Normalized input PPS signal (Point D). Rising edge of PPS signal occurs at the start of the recording.

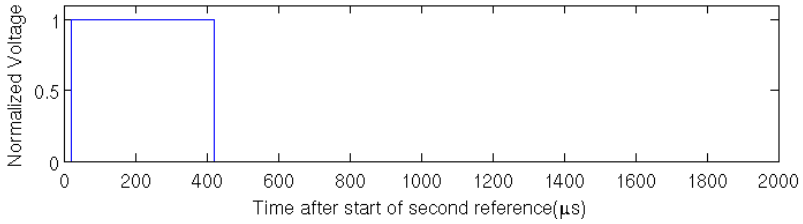

(b) Normalized signal after propagation delays (Point C). Rising edge of the recorded PPS signal occurs at $\tau_C = \tau_{prop}$.

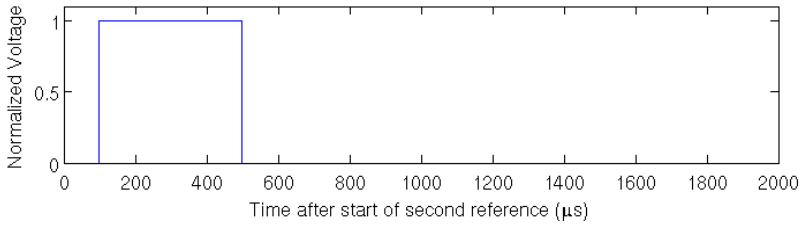

(c) Normalized signal after analog and propagation delays (Point B). Rising edge of the recorded PPS signal occurs at $\tau_B = \tau_{prop} + \tau_{analog}$.

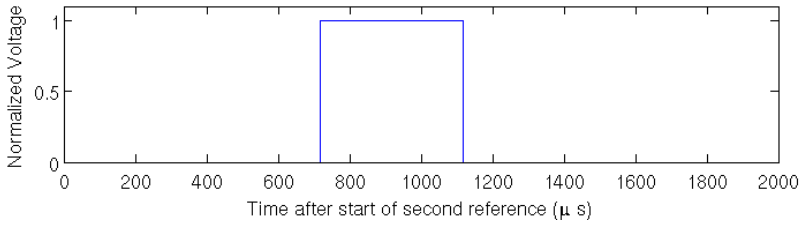

(d) Normalized signal after digital, analog and propagation delays (Point A). Rising edge of the recorded PPS signal occurs at $\tau_A = \tau_{prop} + \tau_{analog} + \tau_{digital}$.

Figure 3-3: PPS signal recorded starting at rising edge of PPS at points D, C, B and A.

by $\tau_C = \tau_{prop}$ relative to the PPS start-of-second reference. It is this delay that we would like to measure. However, the signal is further delayed by τ_{analog}, such that the rising edge of the PPS signal occurs at $\tau_B = \tau_{analog} + \tau_{prop}$ if a recording were made at point B, as shown in Figure 3-3c. Analog to digital conversion further delays the signal, such that in the recording on the DAB the PPS signal arrives with a delay of $\tau_A = \tau_{digital} + \tau_{analog} + \tau_{prop}$ after the PPS referenced start-of-second, as shown in Figure 3-3d.

We need to accurately estimate τ_{prop} using the measured value of τ_A and a calibration

constant such that the range resolution requirement is met(3.2). We therefore define the calibration constant k_{cal} to be:

$$k_{cal} = \tilde{\tau}_{analog} + \tilde{\tau}_{digital} \tag{3.3}$$

This value was used to estimate the propagation delay.

$$\tilde{\tau}_{prop} = \tau_A - k_{cal} \tag{3.4}$$

Two arrival time experiments were used to measure the values of τ_{analog} and $\tau_{digital}$ and therefore to estimate the calibration constant, k_{cal}, used to correct for the system delays in the estimation of τ_{prop}. A third experiment was used to demonstrate that the phase delay introduced by the DAB was small enough to meet the phase requirement, which can be directly expressed in terms of $\tau_{channel}$.

$$\tau_{channel} < 1\mu s \tag{3.5}$$

3.3.1 Delay Characterization with GPS PPS

To get a coarse estimate of analog and digital delays, a GPS PPS signal was played through a speaker and also connected directly into the DAB as an input. The arrival times of the input PPS signal were measured at the points noted in Figure 3-2, giving estimates for delays τ_A, τ_B and τ_C. These delays were used to calculate the system delays. The speaker was kept in the same location for all three measurements.

$$\tilde{\tau}_{prop} = \tau_C \tag{3.6}$$

$$\tilde{\tau}_{analog} = \tau_B - \tilde{\tau}_{prop} \tag{3.7}$$

$$\tilde{\tau}_{digital} = \tau_A - \tilde{\tau}_{prop} - \tilde{\tau}_{analog} \tag{3.8}$$

To calculate the analog and propagation delays through the system, the signals from points B and C were input into a Delta M44 audio card, along with the direct PPS signal. This resulted in time series showing the direct PPS signal, x_D, and either the time series from point B, x_B, or point C, x_C. A sampling frequency of 96kHz was used, and the channels recorded synchronously so that the time difference could be quantified. The digital delay through the Delta M44 could be neglected because it was the same for both channels.

The values of delays τ_C and τ_B were estimated using cross-correlations between the input PPS signal (x_D) and the signal measured at point B or point C (x_C or x_B)[25]. To get more samples, each signal was broken down into snapshots of length N samples, such that a snapshot started at index n and ended at index $n + N - 1$, where $n = 0, N/2, N....$ The cross-correlation was then taken between $x = x_C(n : n + N - 1)$ and $y = x_D(n : n + N - 1)$ to get the delay associated with propagation delay and between $x = x_B(n : n + N - 1)$ and $y = x_D(n : n + N - 1)$ to get the delay associated with the propagation plus analog delays. The two vectors used in calculating the cross-correlation R_{xy} are therefore $x = \{x_1, \ldots, x_i, \ldots, x_N\}$ and $y = \{y_1, \ldots, y_i, \ldots, y_N\}$.

$$R_{xy}(m) = \sum_{i=0}^{N-m-1} x_{i+m} y_i * \tag{3.9}$$

The maximum value of this cross-correlation was found for each snapshot, resulting in a maximum value for the correlation for the snapshot and an associated index number. This index number was multiplied by the sampling frequency to get the value of τ_B or τ_C. These values were then used to calculate $\tilde{\tau}_{prop}$ (3.6) and $\tilde{\tau}_{analog}$ (3.7). An example correlation plot is shown in Figure 3-4.

A similar method was used to calculate the full system delay, τ_A, and used to estimate the digital delay $\tau_{digital}$. Recordings from the DAB were used to determine the value of τ_A. The data recording each second was initialized using the rising edge of the CSAC PPS signal. One of the recordings used in this experiment is shown in Figure 3-5. Note that, while the recording starts on the second, and the PPS replica signal starts on the second, the AC coupled PPS signal shows up after some delay. This delay represents the combined analog,

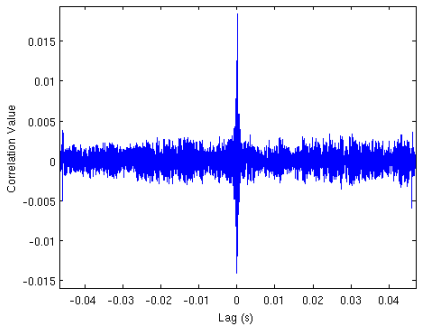

Figure 3-4: Example correlation plot showing the cross-correlation between the input PPS signal and signal at point C versus lag in seconds.

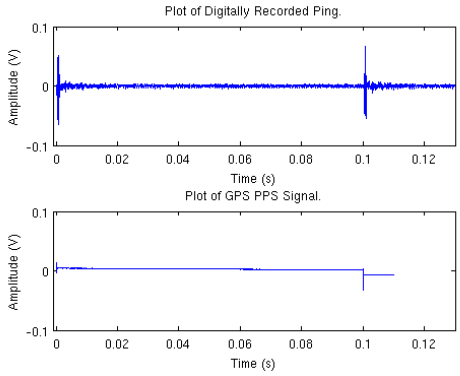

Figure 3-5: Example recording of signal measured at point A versus the direct PPS Signal.

digital, and transmission delays (3.1). To determine the combined delay, 250 recordings were taken, and the value of τ_A was determined by finding the maximum of the cross-correlation between the replica PPS signal and the recorded signal. Finally, the value of $\tilde{\tau}_{digital}$ was determined using (3.8).

3.3.2 Phase characterization with Constant Waveform

The precision of using the GPS PPS signal for calculating delays was limited to a sampling frequency bin. To get a better estimate, a CW with a frequency of $f_{CW} = 8$kHz was used as the input signal in Figure 3-2. Measurements were taken at points B and C and recorded using the Delta M44 audio card along with the input waveform. The phases were then calculated for each time series x.

$$\phi = \arctan(\frac{Im\{x\}}{Re\{x\}}) \tag{3.10}$$

The difference between the phases of the recorded 8kHz CW signal (ϕ_D) and the recorded signal measured at points B or C (ϕ_B, ϕ_C) was then used to calculate the phase shift introduced by the signal passing through the system to point B or C to get more accurate estimate for analog and propagation delays [25]. The measurement of τ_C using delay of the PPS signal as described in Section IV-A resulted in an estimate of 0, indicating that the delay was shorter than the recording bin size of $10.4\mu s$. The value of $\tilde{\tau}_{prop} = \tau_C$ was therefore estimated directly from the phase delay.

$$\tilde{\tau}_{prop} = \frac{\phi_C - \phi_D}{2\pi f_{CW}} \tag{3.11}$$

The analog delay, on the other hand, was longer and therefore was calculated as a phase difference plus some number of cycles M. The value of M that resulted in a value of $\tilde{\tau}_{analog}$ closest to that calculated in the PPS system characterization was chosen.

$$\tilde{\tau}_{analog} = \frac{2\pi M + \phi_B - \phi_D}{2\pi f_{CW}} - \tilde{\tau}_{prop} \tag{3.12}$$

3.3.3 Characterization Lags Between Channels

Characterizing the delays between channels recorded onto the DAB required the use of phase information because the delays of interest are much smaller than the size of the sampling bins on the analog to digital converter. To find $\tau_{channel}$, a CW of frequency f_{CW}=8kHz was input directly into two adjacent channels on one of the DABs, as shown in Figure 3-6.

The phase was then estimated for each channel using (6.5). The total time delay was then calculated using difference between the phases measured on channel 0 and channel 1.

$$\tau_{channel} = abs(\phi_0 - \phi_1)/(2\pi f_{CW}) \tag{3.13}$$

3.4 Results

The calculated delays and calibration constants are shown in Table 3.2. No error is noted for $\tilde{\tau}_{digital}$ because the measured variance of τ_A described the combined analog and digital delays, not the digital delay alone. A description of how these numbers were calculated

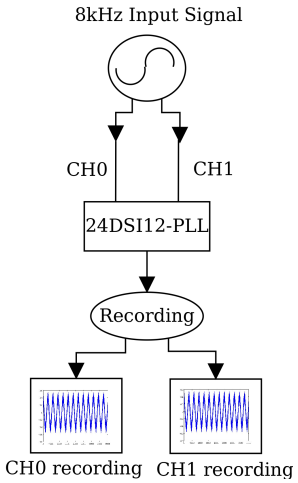

Figure 3-6: Measuring phase difference between channels.

Table 3.2: Delays and Calibration Constants

Variable	Mean $[\mu s]$	Error
$\tilde{\tau}_{analog}$	77.38	$< 1.75\mu s$, 95%
$\tilde{\tau}_{digital}$	620.0	
$\tilde{\tau}_{channel}$	0.0074	$< 0.000223\mu s$, 95%
k_{cal}	697.38	$< 21.2\mu s$, 95%
$k_{cal,d}$	77.38 + $\tilde{\tau}_{digital,d}$	$< 16.375\mu s$, 99.7%

follows.

3.4.1 Analog Delay

The value of the analog delay using the GPS PPS characterization was found to be 72.95 μs +/- 5.21 μs. There was zero variance in the measurement of τ_B and therefore $\tilde{\tau}_{analog}$ using this method, but the accuracy of the characterization was limited to half of a time bin, 5.21 μs.

A more accurate estimate of analog delay was calculated using (3.12). The resulting analog delay, $\tilde{\tau}_{analog}$, was found to be 77.38 μs with a standard deviation of 0.875 μs. This means that the calibrated system had a timing error introduced by the analog delays of less than 1.75 μs with 95% accuracy.

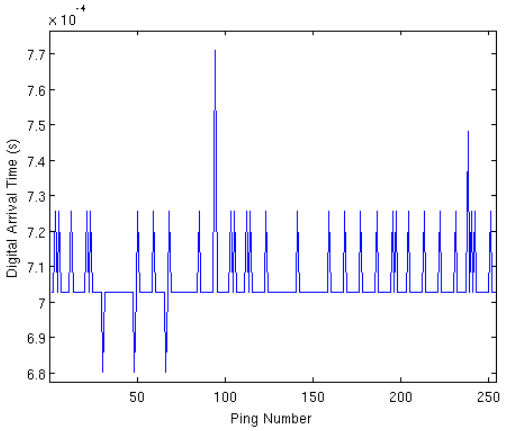

Figure 3-7: Plot of measured τ_A versus Ping Number.

3.4.2 Digital Delay

The digital delay was calculated using cross-correlations of recordings at point A to find the value of τ_A and then subtracting the analog and propagation delays. The value of τ_A is far more variable than the τ_B and τ_C, with a mean of 705.6 μs, a standard deviation of 9.00 μs and a range of 90 μs. Each measurement is only known to +/- 13.3 μs because of the digitization of the incoming data. A plot of the measured values of τ_A is shown in Figure 3-7. The mean digital delay, $\tilde{\tau}_{digital}$, was calculated from this as 620.0 μs.

3.4.3 Lag Between Channels

The lag between adjacent channels was found to have a mean of 7.40 ns and a standard deviation of 0.223 ns. This exceeds the requirement of $1\mu s$ phase accuracy, and confirms that the DAB board's synchronous data acquisition is adequately synchronous for this experiment.

3.4.4 Calibration

The value of k_{cal} was determined using these digital and analog delays. The standard deviation from the τ_A data for the digital delay estimation was used to calculate the error in the timing system, statically calibrated to eliminate the analog plus digital mean delays, as less than 21.2 μs with 95% accuracy. $\tilde{\tau}_{prop}$ therefore meets the requirement in (3.2). The calibration was performed by subtracting k_{cal} from the beginning of the second in the timestamps for the recorded acoustic files. The final timestamp, therefore, is corrected using the mean and has an error of less than 21.2 μs with 95% accuracy.

3.4.5 Calibration using Dynamic Estimation of Digital Delay

While the system error with static estimate of the digital delay exceeded the requirements for this system, it might be desirable to further reduce this error by dynamically estimating the digital delay and therefore reduce uncertainty. The large uncertainty in the digital delay was introduced by the process of analog-to-digital conversion on the DABs. Measurements showed that this process caused additional signal delays with a standard deviation of $9\mu s$ but with a range of 90 μs. Dynamic estimation was performed by passing the CSAC PPS signal directly into one of the channels on each DAB, running a cross correlation between the replica PPS and the recording, then finding the maximum correlation value in real-time. This dynamically estimated digital delay, $\tilde{\tau}_{digital,d}$, was then used in the calculation of $k_{cal,d}$ (3.14).

$$k_{cal,d} = \tilde{\tau}_{analog} + \tilde{\tau}_{digital,d} \tag{3.14}$$

With the two calibration steps, finding τ_{analog} and dynamically estimating $\tau_{digital}$, the range accuracy of the system becomes 16.375 μs with 99.7% accuracy, eliminating the source of the greatest time estimation error. This calculation can be done in real-time alongside the logging of data, and the data timestamp is adjusted to become the current second minus the dynamically estimated value of $k_{cal,d}$ to accommodate the relative timing.

3.5 Conclusions

Successful development of the described acoustic data acquisition system was dependent on the selection of a clock, synchronous analog-to-digital converter and amplification/filtering systems, and on the characterization of the delays inherent in those systems. The use of the Quantum CSAC SA.45s, synchronized to GPS, assures a clock precision of 10ps and a clock accuracy relative to GPS of $1\mu s$. The data acquisition of the DAB analog-to-digital converter is synchronous to within 7.4 ns, surpassing phase accuracy requirements for this application by several orders of magnitude. Characterization and calibration of the analog and digital delays in this system make the data acquisition accurate as well as precise. The measured analog delay was 77.38 μs. If this delay is not taken into account the range estimation will

be off by more than 0.1m. The digital delays were even more significant: 620.0 μs, which would result in a range error of nearly 1m. When the system was calibrated using a fixed estimate of the analog and digital delays, the system's arrival time error became less than 21.3μs with 95% accuracy. It was demonstrated that this accuracy can be further improved by using the static analog delay and a real-time dynamic estimation of digital delay, in which case the system's arrival time error became 16.375 μs with 99.7% accuracy. The precise and accurate timing in the final data acquisition system was one of the primary factors in the successful data collection in the BayEx'14 and Massachusetts Bay experiments, discussed in the next Chapter.

Chapter 4

Data

The goal of this research was to investigation the plausibility of characterizing underwater target geometry using amplitudes calculated by an AUV sampling the bistatic scattered field between source and target. Four data sets are used for this investigation: A bistatic scattering data set that includes spherical and cylindrical target data from the BayEx'14 experiment in May 2014, a bistatic scattering set that includes two aspects of a steel pipe from a Massachusetts Bay experiment in November 2014, and two scattering simulation data sets matched as closely as possible to the experiment conditions. In both real world experiments the Bluefin 21 AUV *Unicorn*, fitted with a 16 element nose array and payload described in Ch. 3, was used to collect acoustic data with the goal of finding target scattered radiation patterns like those discussed in Ch. 2.

This chapter first describes the hardware and software configurations on the AUV *Unicorn* used for the bistatic scattering experiments. The BayEx'14 experiment is then explained, including the environment, source, and vehicle deployment, and the resulting acoustic data set. Next, the Massachusetts Bay experiment and data set are described. Finally, the methods used to create the simulated acoustic scattering models are explained and the simulated scattered fields compared to the real-world data.

4.1 AUV Unicorn

The Bluefin 21-inch AUV *Unicorn* was used for data collection (Figure 4-1). *Unicorn* is a 3m long, 21 inch diameter AUV that was outfitted for these experiments with an acoustics and autonomy payload that included a 16 element nose array with 0.05m element spacing,

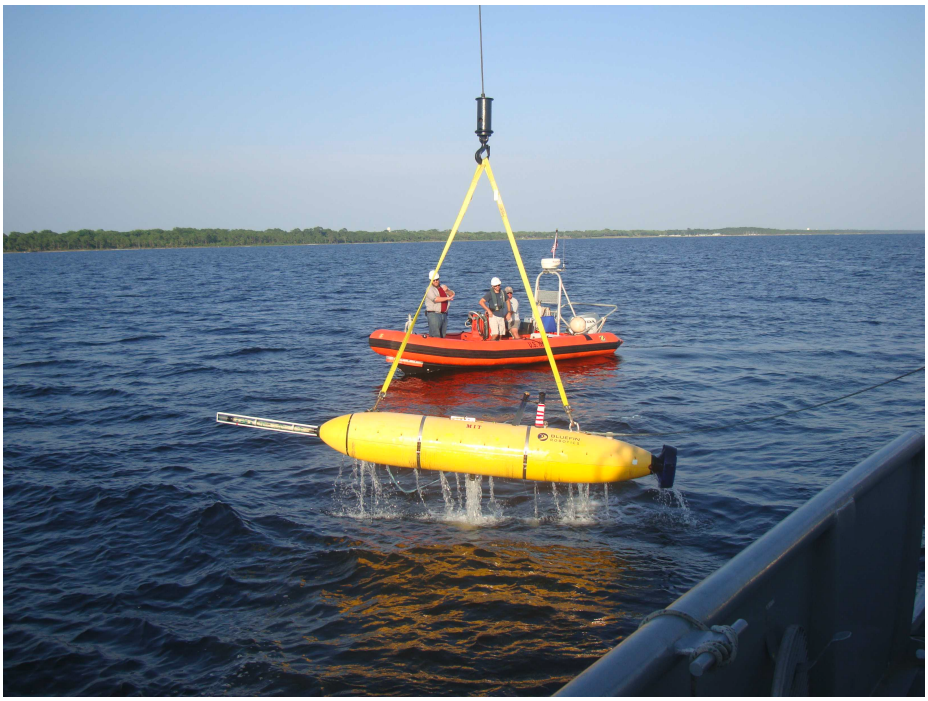

Figure 4-1: The AUV *Unicorn* being lifted from the water by the crane of the *PCS-12* during the BayEx'14 experiment.

calibrated precision timing/data acquisition hardware described in Ch. 3, and a computer for autonomy and signal processing. The vehicle also carried a Sea-Bird Electronics model SBE 37-SI CT sensor [26] and a pressure transducer used for depth measurements. The vehicle ran under a front-seat/back-seat control architecture, with basic navigation and sensor fusion handled by the front-seat computer and vehicle autonomy, acoustic communications, and acoustic processing handled on the back-seat computer with processes in MOOS, IvP Helm [27] and Goby [28].

4.1.1 Navigation

Good navigation and adaptive autonomy were critical for vehicle safety in the BayEx'14 experiment because the safe operational area was only 300 meters by 300 meters with a water depth of 6 to 7 meters, and the sampling area for each target less than 40 meters by 50 meters. The vehicle's navigation sensors included a Doppler Velocity Log (DVL), Global Positioning System (GPS), a Leica DMC-SX Magnetic Compass, and a Honeywell HG1700 Inertial Measurement Unit (IMU). The Honeywell IMU was recently installed to improve the navigation of the vehicle while submerged: the previous system resulted in

a navigational drift of 1% to 5% of distance travelled[29]. The navigational drift with the improved instrumentation was between 0.3% and 0.5% of the distance travelled between GPS fixes. The vehicle surfaced for GPS every 10 minutes to prevent drift from accumulating significantly.

4.1.2 Acoustic Payload

To collect high-quality acoustic bistatic data in these experiment, *Unicorn's* acoustic payload was updated and calibrated to ensure timing error of less than $70\mu s$. Precision timing was required for bistatic data collection because the source and vehicle are not co-located. The source was triggered directly by a GPS Pulse Per Second (PPS) signal, but GPS signal is not available underwater so *Unicorn* required a separate precise and accurate on-board time source for hardware-triggered data acquisition. A PPS signal indicates the start of a second with the rising edge of a duty-cycled square wave and is used as a trigger for clock synchronization.

The timing and data acquisition hardware included a Quantum SA.45 Chip Scale Atomic Clock (CSAC) [22], two 24DSI12-PLL analog to digital data acquisition boards (DABs)[20], and a Garmin 15LxW GPS for synchronization on the surface and is described comprehensively in Ch. 3. Binary files, including data from all 16 hydrophone channels, were recorded on the computer using this system. These files started exactly at the start of each second as triggered by the CSAC PPS signal. To further improve accuracy, the analog and digital delays in the system were characterized and used to calibrate the timestamps of the recorded binary files.

4.1.3 Signal Processing

The recorded data files on the Advantech computer were read into MOOS-IvP, which provided a convenient framework for signal processing in real time on the vehicle and for processing in simulation using navigation and acoustic data logged during an experiment. A MOOS process, pActiveTargetProcess, was used to extract the amplitudes for targets at specified locations from a recorded data files. The operations of this process are shown in Figure 4-2. The locations of the target and vehicle for each recorded data file are first used to identify a time window for processing. This time window is centered around the expected arrival time, with a length to either side determined by replica length, navigation uncer-

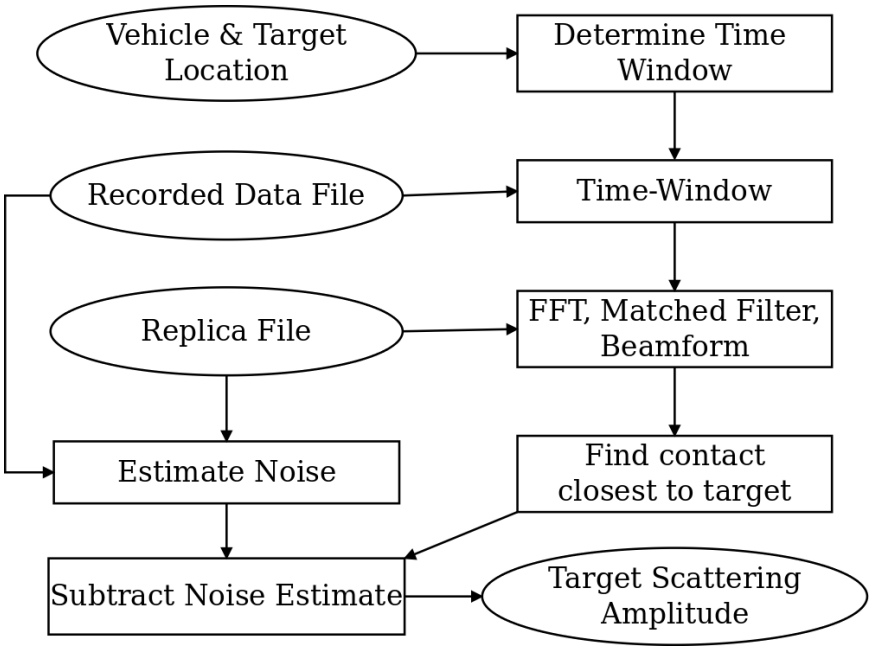

Figure 4-2: Processing in pActiveTargetProcess used to extract target amplitudes from the array time-series. The recorded data file, vehicle/target location information, and replica are used to estimate the target scattering amplitude.

tainty, and uncertainty in soundspeed estimate. The data from all 16 channels is windowed, then a Fast Fourier Transform (FFT) is taken using FFT length NFFT. Matched filtering with the source replica is used to identify contacts, and beamforming is used to determine the bearing to the targets and the error in that estimate. Thresholding eliminates some of these contacts. The process outputs the band-averaged amplitude from the contact with the location (based on bearing and arrival time) that is closest to the expected target position. If the vehicle is in the target's forward scatter region the target contact cannot be distinguished from the source's direct blast so the process does not produce an amplitude. If no target is located within 25m of the expected target location, no contact is reported.

The direct blast is always in the data file and the vehicle is always at least 30m from the source in this experiment, so ambient noise could be estimated as the band-averaged amplitude from the first NFFT samples in the 7-9kHz band. The estimated noise amplitude was subtracted from the estimated target scattering amplitude associated with each recording to get the estimated target scattering amplitudes used for analysis. This process was used to extract the full amplitude grid around each target from the recorded data.

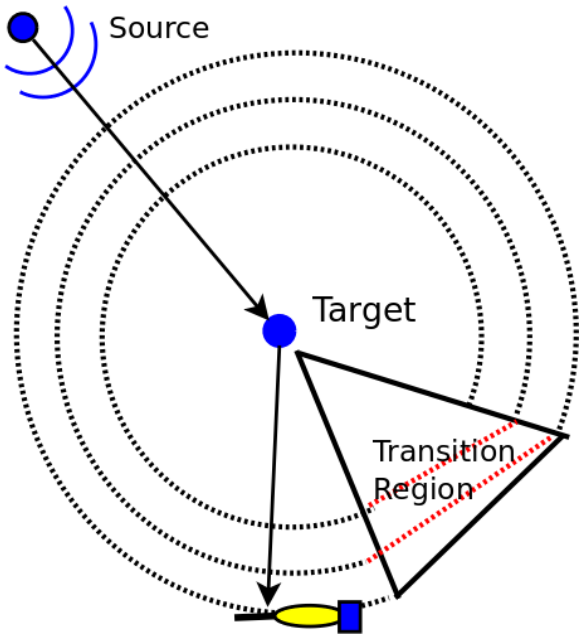

Figure 4-3: Full field sampling behavior used with the vehicle *Unicorn* for collecting target bistatic data sets. The vehicle circles the target, changing radius in the direct forward-scatter direction.

4.1.4 Vehicle Sampling Behavior

One of the limitations in previous attempts to collect real-world bistatic scattering data with AUVs was the non-uniformity of the acoustic data set. Conventional AUV behaviors, such as lawnmower patterns, are poorly suited for acoustic data acquisition around targets, as the target's contact moves from endfire to broadside and back to endfire. This results in inefficient data collection. To correct this, a behavior was written to collect a full grid of bistatic amplitudes around a target in depth, range, and azimuth. The vehicle completes a sequence of concentric circles with decreasing radii. By transitioning in radius only in the forward scatter direction, the vehicle goes out of broadside in the region where the target contact cannot be distinguished from the direct blast from the source. This sampling layer is repeated at multiple depths to complete data collection on a target. Figure 4-3 shows how a single layer of the vehicle path is constructed for this behavior. The behavior is configured using the number of layers sampled, the number of radii sampled, the minimum and maximum depths, the minimum and maximum radii, the minimum permitted distance to the operational boundary, the target location and the source location.

This behavior was made adaptive to prevent the vehicle from leaving the operational

Table 4.1: Target Geometry.

Spherical Shell		
	Diameter	$0.6m$
	Material	Steel
	Shell density	$7.975g/cm^3$
	Shell bulk compressional speed	$5.773\text{x}10^5 cm/s$
	Shell bulk shear speed	$3.100\text{x}10^5 cm/s$
	Shell thickness (thicknessx100/radius)	5.1
Solid Cylinder		
	Diameter	$0.3m$
	Length	$0.9m$
	Material	Aluminum

area. While the vehicle is following a circle, small changes in heading are made to correct the vehicle's location so it remains at the appropriate radius. However, if the vehicle is within a configurable distance from the bounding box, these corrections cannot include an increase in radius. In addition, if the specified maximum radius is greater than the distance from the target to within 10m of the bounding box or an obstacle, the behavior automatically rescales to fit within the safe region.

4.2 BayEx'14 Experiment

4.2.1 Experiment Parameters

The geometry of the BayEx'14 experiment site on May 21 is shown in Figure 4-4. Two targets, a 0.66m diameter spherical shell and a 1 foot diameter, 3 foot long solid aluminum cylinder, were deployed about 60m from the ends of the source rail. See table 4.1 for the target geometric and material properties. The *RV Sharpe* was anchored in a four point moor, and provided a reference point for the source rail. The directional source was set at the north end of the rail for the morning to insonify the sphere and the south end of the rail for the afternoon to insonify the cylinder. The source was set to fire a 10ms, 7-9kHz LFM chirp on a 1Hz schedule synchronized to GPS PPS. The water depth at the test site was 6-7m, with a mud bottom over sand.

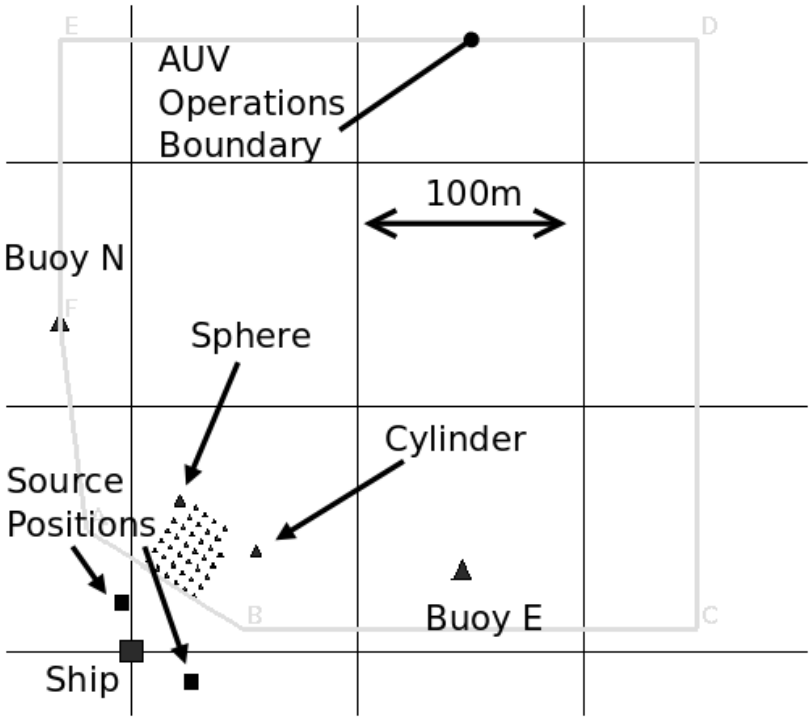

Figure 4-4: Experimental configuration, with source positions, target positions, and AUV operational box.

4.2.2 AUV Deployment

The AUV *Unicorn* was deployed off of the *PCS-12*, which was anchored on the north end of the operational area shown in Figure 4-4. To ensure *Unicorn* did not hit anything while operating in the tight region between the targets and the source rail, an operation area and obstacle avoidance points were selected to keep it away from the buoys and other collision dangers. In addition, the acoustic sampling behaviors kept the vehicle moving perpendicular to intersection with and at least 10m away from the operational boundary. Altitude safeties prevented the vehicle from nosing into the bottom by aborting the mission when *Unicorn* measured an altitude of less than 2m. The MIT LAMSS MOOS-IvP [27] infrastructure with Goby [28] interface to acoustic communications meant that new commands could be sent without recovering the vehicle to improve sampling or increase vehicle safety in the tight operational area.

4.2.3 Data Description

During the experiment, *Unicorn* was successfully commanded to 15 target sampling missions over the course of the day, 5 for sphere sampling in the morning and 10 for cylinder sampling in the afternoon. As the vehicle trim was not very good and the salinity varied greatly in the operating area, the vehicle's depth control was not precise, so the data was collected from multiple depths at each circle around the targets. To adjust, 3 depth levels were used in sampling and 5 radii, and the full data collection was repeated at least twice around each target. Commanding data sampling deeper than 3.5m resulted in a depth abort because of the shallow water depth, so the commanded depths were between 1.5m and 3.5m. Figure 4-5 shows the locations of all acoustic data files collected around both targets in the original coordinate system. CTD data was collected continuously on the vehicle during acoustic sampling, resulting in a temporally diverse environmental data set between 0 and 5m depth.

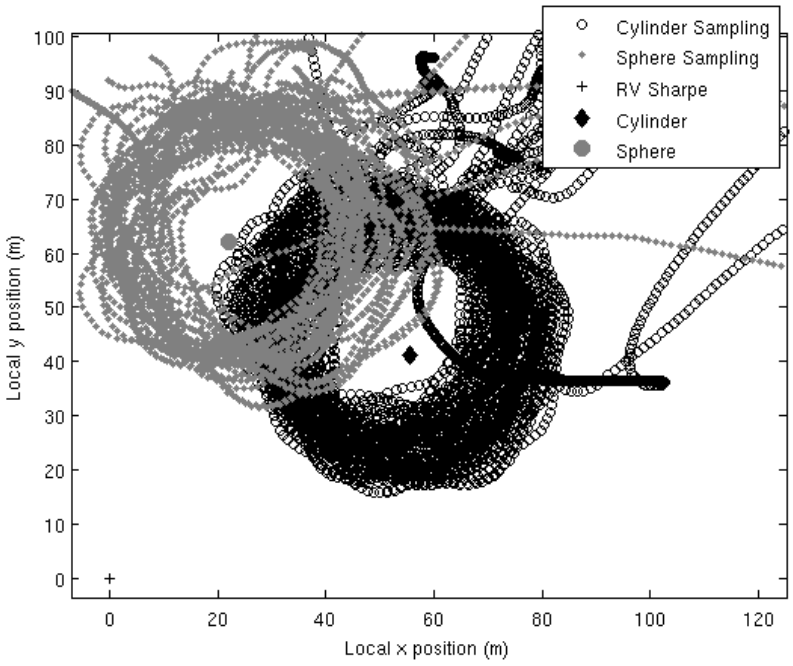

Figure 4-5: Locations of collected acoustic data files in x and y relative to the position of the *RV Sharpe*.

Environmental Data

Difficulties with vehicle trimming resulted in a yoyo-like depth behavior in the vehicle. While this was not optimal for uniform sampling of scattering amplitudes, it did provide an excellent look at the pycnocline through the day and continuously sampled in depth.

Hysteresis was observed in the temperature and salinity measurements taken during the experiment, seen in the large changes that occur on a single yoyo through the halocline/thermocline. This is identical behavior to that observed in the temperature data collected in the GLINT'10 experiment as described by Petillo and Schmidt[29], and is due to the slow acquisition time of the temperature and salinity sensors as compared to the depth sensor. To correct for this, the environmental data was divided into upward-going data and downward-going data sets. The two are correlated then averaged to find a corrected depth value for each measurement. The final salinity, temperature, and soundspeed data are shown in Figures 4-6, 4-7 and 4-8. These figures show the changes in the profiles through time. Each line in each subplot shows the hysteresis-corrected, averaged profile over a 1 hour interval. The time on each subplot is the UTC time in the corresponding log file from the experiment. The average of this collected soundspeed profile was used for replicating experiment conditions in simulation.

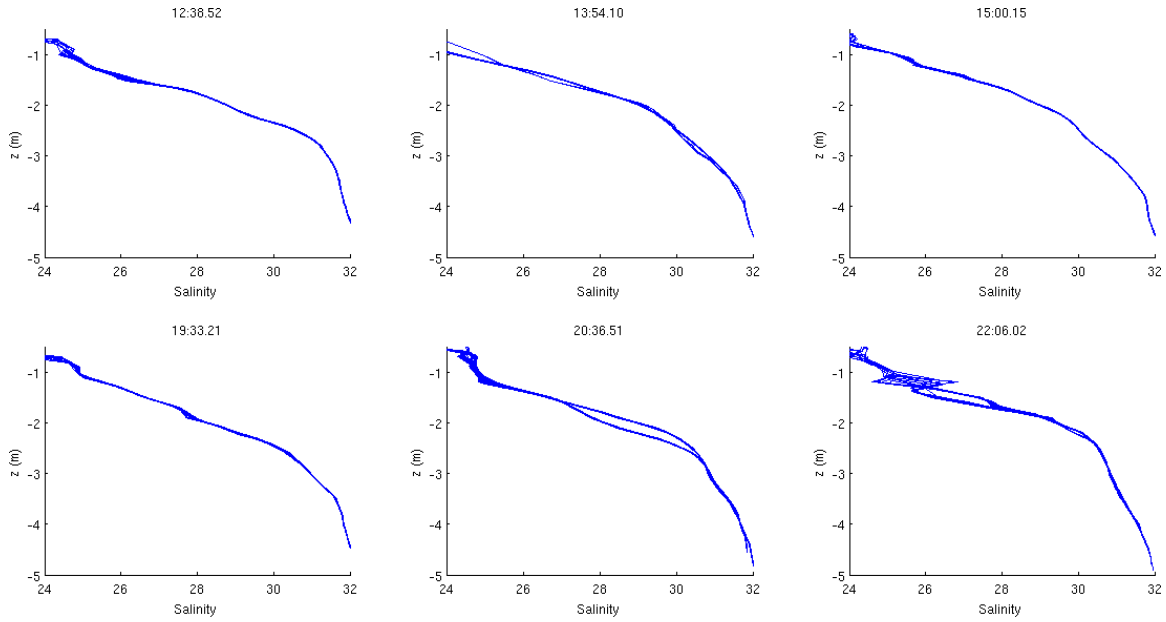

Figure 4-6: Salinity data collected with *Unicorn* on May 21 during the BayEx'14 experiment.

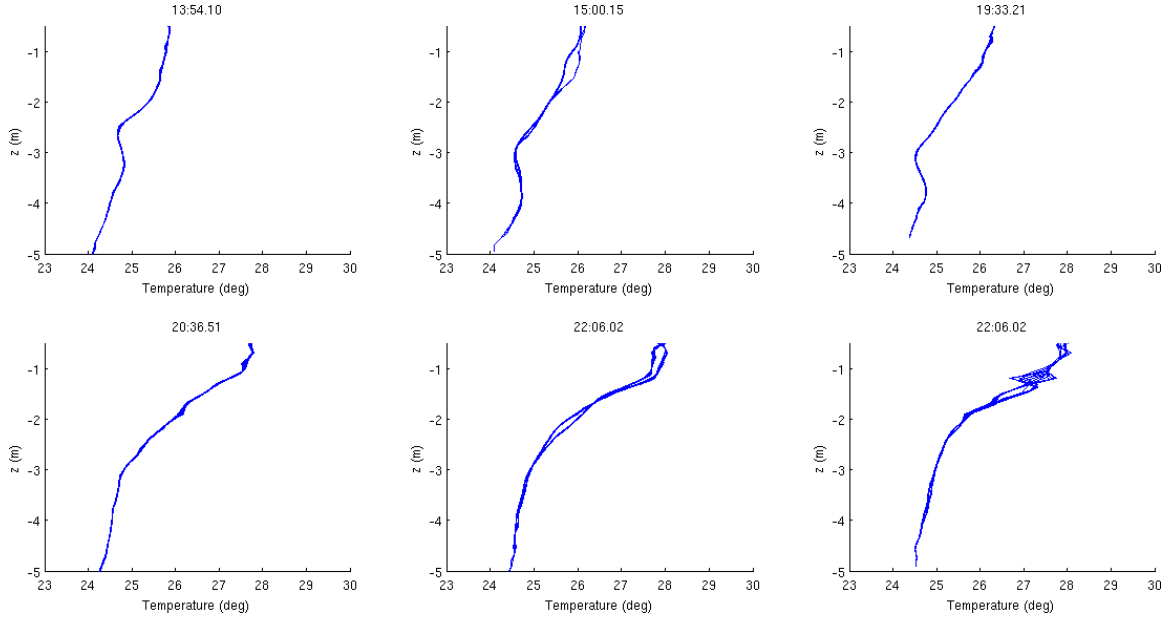

Figure 4-7: Temperature data collected with *Unicorn* on May 21 during the BayEx'14 experiment.

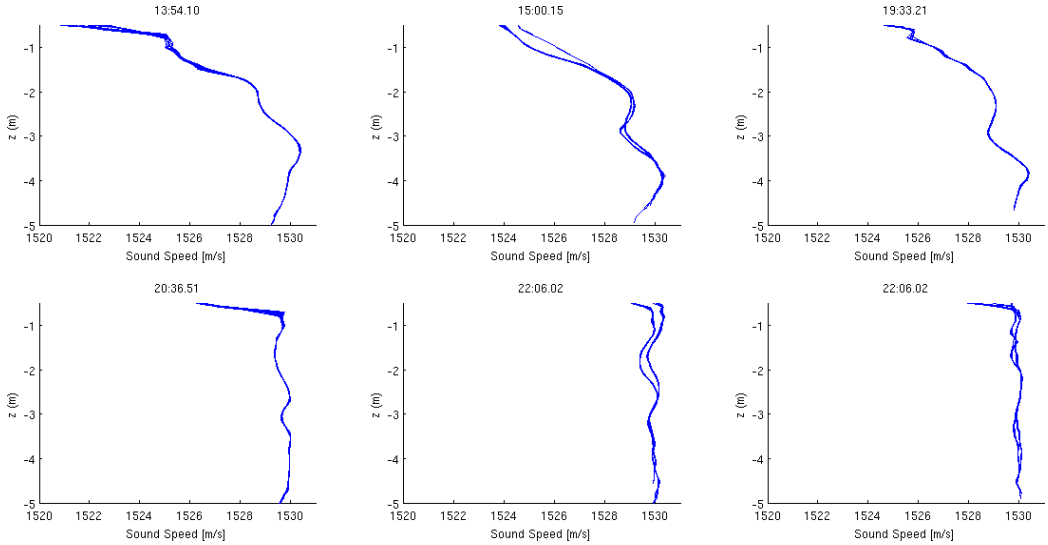

Figure 4-8: Sound speed data collected with *Unicorn* on May 21 during the BayEx'14 experiment.

Acoustic Scattering Data

Each of the collected acoustic data files starts at the beginning of the second with the firing of the source, and therefore includes the direct blast. The sampling rate on the DABs was set to 37500Hz, and each data file contained 8000 samples for the 16 channels. 15 of the 16 channels worked properly during the experiment. The data from the broken element was

ignored during processing.

The noise amplitude was estimated from first NFFT samples in each recording in the 7-9kHz frequency band and subtracted from the target amplitude to correct for varying noise levels. This correction reduced the effect of noise, including periodic noise, on the data. The most significant periodic noise source was introduced by the firing of the acoustic modem every 40 seconds.

The final data sets included 2162 usable scattering amplitude points around the sphere and 4784 usable points around the cylinder. This excludes data in the forward scatter direction indistinguishable from the direct blast, data made noisy by surface transport of the vehicle by the rib boat, data when the vehicle is far from the target, data when the source is off and data made unusable by other noise sources. The lower number of data points from the sphere is a result of high levels of noise in approximately one third of the sphere data set, caused by a line wrapped in the vehicle's tail cone.

Each scattering amplitude represents the processing of an acoustic file consisting of 16 channels of data the MOOS application pActiveTargetProcess. pActiveTargetProcess time-windows the data around the expected arrival time, performs matched filter and beam-forming operations, and finally selects the contact coming from the correct direction. For processing, NFFT was set to 1024, 30 beams were used, and the matched filter operation was performed with a 90% overlap for high time resolution. The band-average amplitude over the 7-9kHz frequency band was reported.

The processed scattering amplitudes provided a dense grid between 1.5m depth and 3.5m depth and between 10m radius and 35m radius from the target. There is a region within +/-10 degrees of the forward scatter direction where the target amplitudes are not calculated because the direct blast is not distinguishable from the target contact. The following target scattering plots use a coordinate system that puts the target location (x'_t, y'_t) at $(0, 0)$ the source at $(x'_s, y'_s) = (-r_s, 0)$, where r_s is the distance between the source and target. Constructing the coordinate system in this manner allows the scattering fields to be compared between the two target types and with the scattered fields from the scattering simulation package for similar target types and environments.

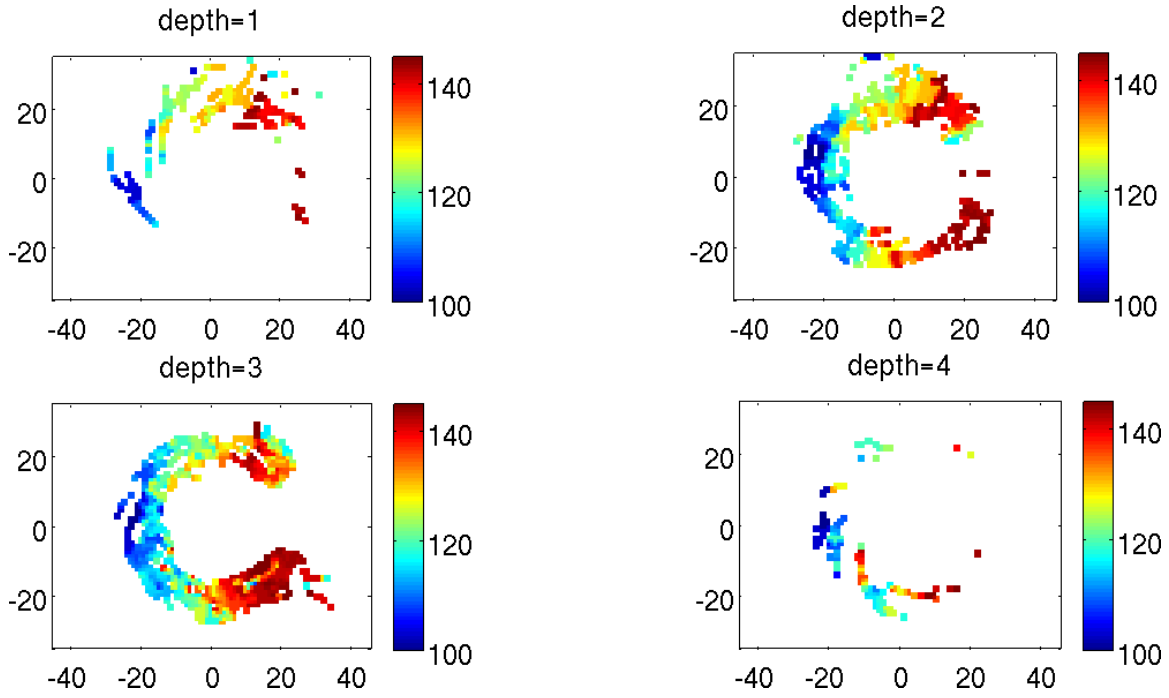

Figure 4-9: Sphere scattering amplitudes for depths 1m to 4m versus position in target-centric coordinate system.

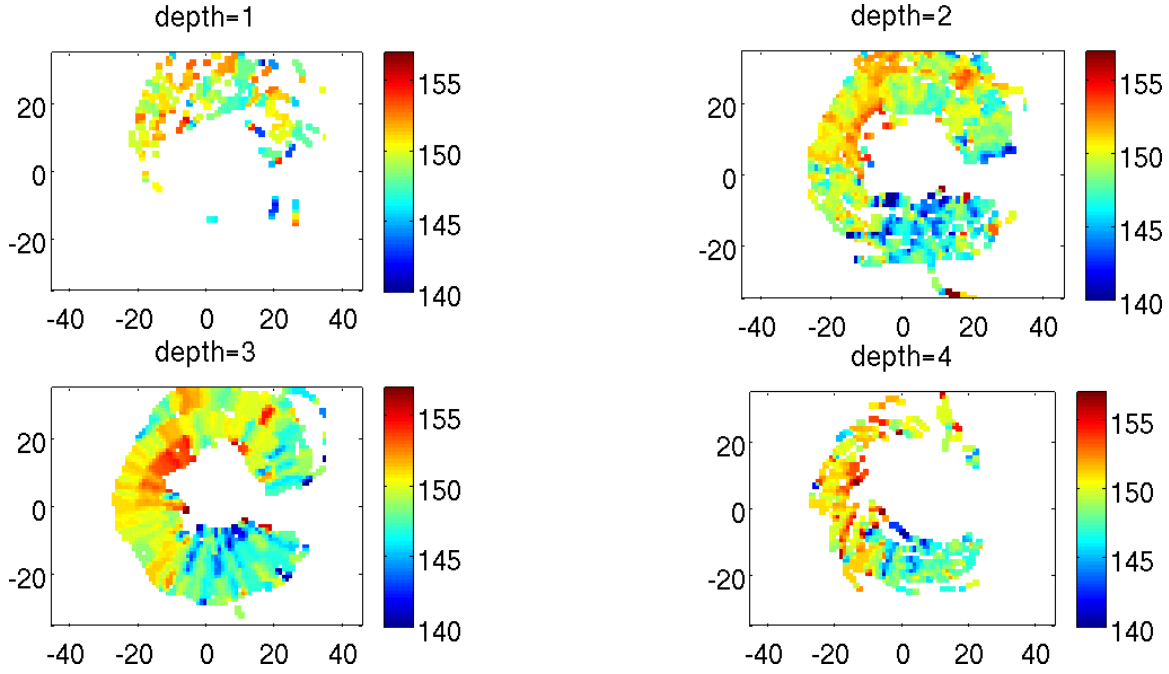

Figure 4-10: Cylinder scattering amplitudes for depths 1m to 4m versus position in target-centric coordinate system.

The scattered field grids for the full set of depths are seen in Figure 4-9 for the sphere

and 4-10 for the cylinder. Depths of various samples are binned in 1m increments to get a view of the shape of the collected scattered field data, such that data from 0.5m depth to 1.5m depth are plotted together in the 1m depth plot, data from 1.5 to 2.5m is plotted together in the 2m depth plot, and so on. This comprehensive scattering data set shows the minima-maxima pattern around the respective targets and the depth dependence of that pattern.

Looking just at the densest of these grids in Figure 4-11, showing the 3m depth slice, gives a better sense of the angular dependence of the radiation pattern for the sphere versus cylinder target. Additional comparisons were carried out by looking only at the angular dependence of the scattering amplitudes. Figure 4-12 shows radiation pattern polar plots of mean amplitude minus minimum amplitude for the real spherical and cylindrical scattering grids at 3m depth. The amplitude values were binned in angle using 5 degree increments and averaged in intensity to determine the amplitude value at each bistatic angle.

The color and polar radiation pattern plots are valuable for comparing the overall patterns in the scattering fields of the targets. Most importantly, the sphere and cylinder data are easily told apart based on these bistatic scattering patterns, which was the purpose of collecting this bistatic data set.

The sphere data shows a nearly symmetric pattern, with overall intensity is lower in the backscatter direction than the forward scatter direction. Maxima are present at 130/230 degrees and 150/210 degrees, with a strong minima at 180 degrees in the direct backscatter direction. This dip is the Faran-type minima predicted by Gaunaurd and Uberall for $ka = 10.9$ in their form function versus ka plot in figure 8A for free space bistatic scattering from a spherical target [2]. $ka = 10.9$ occurs for the geometry of the 0.33m diameter spherical target at a frequency of 7.878kHz, near the center frequency of the LFM chirp used in this experiment.

The cylinder shows a clear specular glint around 45 degrees, a strong lobe at 240 degrees and stronger backscatter than the sphere. The glint and the source signal should have equal angles from broadside to the main cylinder axis. The cylinder axis is at 24 +/- 5 degrees in the experiment, which puts broadside at 114 +/- 5 degrees. This means that the predicted glint should be at 48 +/- 5 degrees, where it is observed in the data.

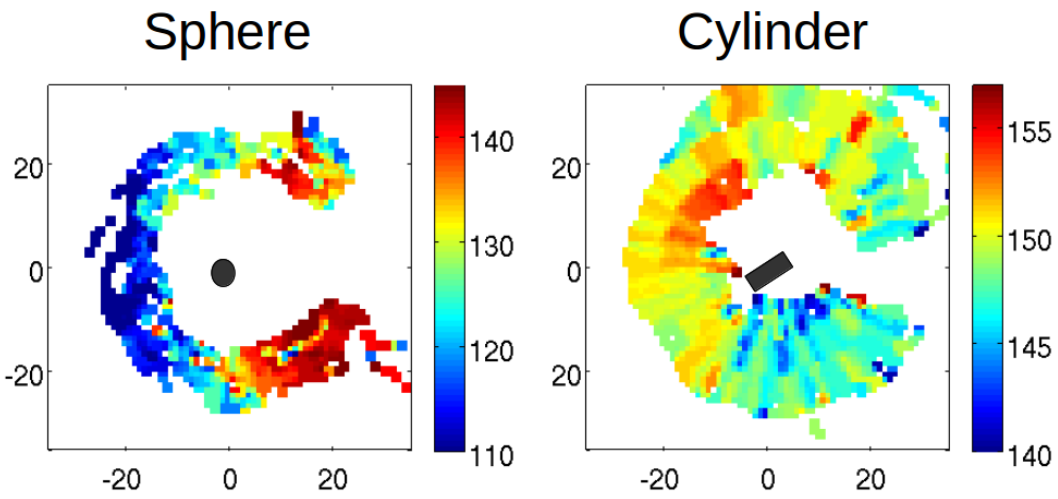

Figure 4-11: Scattering amplitude grid around spherical and cylindrical targets, including target positioning and cylinder rotation. Amplitudes were averaged between 2.5 and 3.5m in depth. Note the distinctive specular glint in the cylinder data around 45 degrees caused by reflection.

Ambient Noise

The data collection vehicle behavior gave a excellent means for determining the directionality of ambient noise in the local environment. The calculated noise in the 7-9kHz range at the various vehicle headings was plotted versus the beamforming angle (i.e. broadside to the vehicle heading) to get a noise "rose" for the region where data was collected. If the surface effects are ignored (i.e. data from depths less than 1m are neglected), the ambient noise is nearly omnidirectional for these frequencies, as seen in Figure 4-13.

4.3 Massachusetts Bay Experiment

On November 10, 2014 a second bistatic scattering experiment was conducted in Broad Sound of Massachusetts Bay using the AUV *Unicorn*, a 147dB omnidirectional Lubell source,

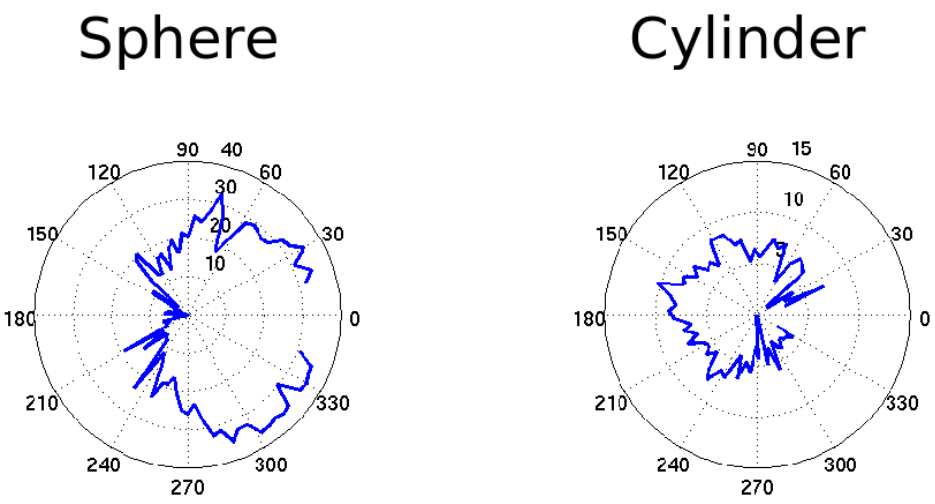

Figure 4-12: Polar plot showing angle dependence of mean target scattering amplitude for spherical and cylindrical targets. Difference between intensity-averaged amplitude and minimum amplitude is plotted on the r-axis and angle in the source-target coordinate system on the θ axis.

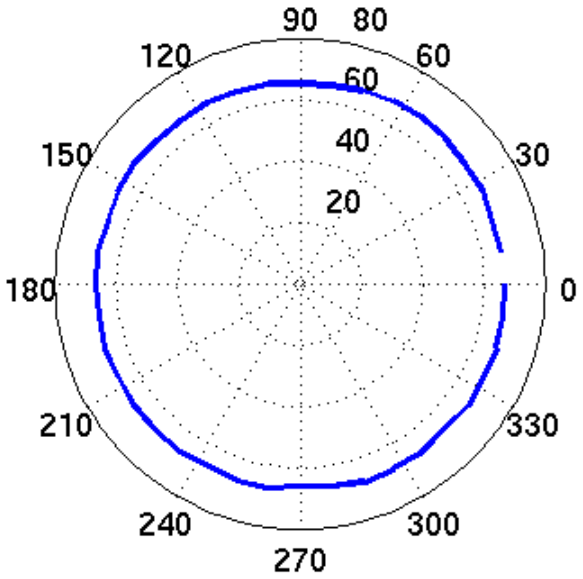

Figure 4-13: Ambient noise in dB re 1 μPa versus beamforming direction in degrees, where beamforming is always conducted broadside to the AUV array. For example, the measurement at 0 degrees represents the noise to the east, 90 degrees to the north, and so on. The resulting noise "rose" shows nearly omnidirectional ambient noise in the 7-9kHz range.

and an open-ended steel pipe target deployed off of the R/V *Resolution*. There were three main goals of this experiment:

1. Demonstrate feasibility of bistatic scattering data acquisition in a more challenging configuration, with a ship-based, low-power omnidirectional source and large target location uncertainty.

2. Collect bistatic scattering data sets around an aspect-dependent target at different orientations.

3. Run sampling behavior in a location without a target to collect a null bistatic scattering set to compare with scattering when a target is present.

4.3.1 Experiment Parameters

The configuration for this experiment is shown in Figure 4-14. The ship was first anchored to the north of the target to collect the null data set and bistatic data for the first target aspect. The ship was then moved to the south and west of the target to collect bistatic data for the second target aspect.

Environment

The part of broad sound used for this experiment has a sand bottom and was between 15 and 18 meters deep while we were collecting data.

Target

The 1.5 foot diameter, 5 foot long steel pipe was dropped at an approximate local coordinate position of $(x_t, y_t) = (170, 155)$ (Figure 4-15). The location was estimated using ship position when the target was dropped, but was only accurate within 10-15m. The orientation of the target was unknown.

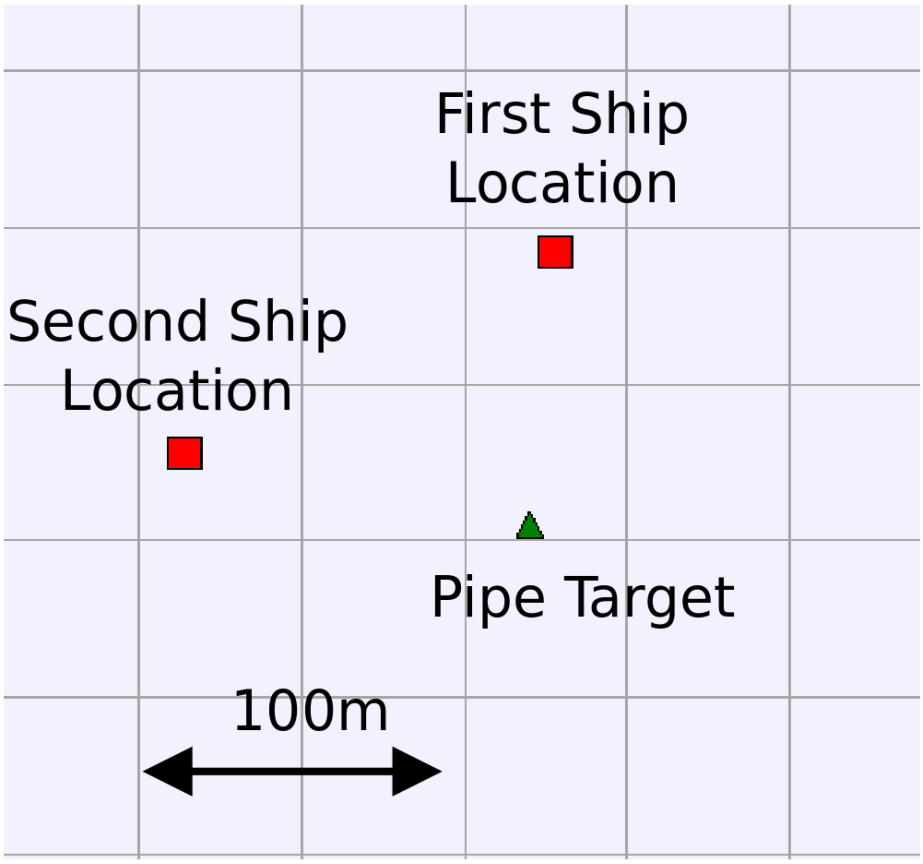

Figure 4-14: Configuration for Massachusetts Bay experiment, including source and target positions. The R/V *Resolution*, with the Lubell source deployed at 3m depth, was first anchored about 100m north of the target, then moved to approximately 100m west of the target.

Figure 4-15: Open-ended steel pipe used as a target during the Massachusetts Bay experiment, sitting on the deck of the R/V *Resolution*. The pipe is 1.5 feet in diameter and 5 feet long.

Source

A Lubell 916 acoustic source was used to insonify the steel pipe from the ship [30]. The Lubell source is an omnidirectional underwater speaker capable of outputting 200Hz-20kHz in frequency. The source level was calculated as 147dB for this experiment. It was deployed at 3m depth off of the bow of the R/V *Resolution*. A CSAC-based PPS software triggering system was used to fire a 10ms, 7-9kHz chirp from the Lubell each second. Characterization of this system showed that it fired within 5ms of the start-of-second PPS signal. The jitter in firing was caused by the USB-to-Serial converter used to communicate with the CSAC. While this was not ideal, and a hardware triggering system should be developed for future scattering experiments using this source, the additional uncertainty provided a good test of the robustness of the signal processing chain to navigation and timing error.

4.3.2 AUV Deployment

The R/V *Resolution* was first anchored to the north of the target to collect a null scattering set and bistatic scattering from the first aspect on the target. It was then moved south and west so that *Unicorn* could collect a bistatic scattering set from the second aspect of the target. Like in the BayEx'14 experiment, the vehicle was commanded using MOOS-IvP and Goby over the WHOI MicroModem.

4.3.3 Data Description

Figure 4-16 shows the AUV sampling, ship and target locations for the three data collection sequences. In the first, the AUV collects a null data set by sampling about $(x, y) = (170, 120)$. The AUV was then commanded to circle several points near local coordinate $(x, y) = (170, 155)$, the final estimated target location. Our estimate of the actual target location changed as the experiment continued, so that the vehicle was giving a sampling center progressively further north over the course of the experiment.

The second DAB board malfunctioned during data collection, so only the first 8 hydrophones could be used for data processing. This was not a major impediment to characterizing the radiation pattern from the two target aspects, as there was still enough resolution and aperture to distinguish the target contact. In total, 2065 usable acoustic amplitudes were collected about the first target aspect and 4363 about the second target aspect. Pro-

cessing of the null data set output only 650 acoustic amplitudes as many pings did not contain a strong enough contact coming from within 25m of $(x, y) = (170, 120)$. A moderately dense grid was collected from depths of 3 to 7 meters and from radii of approximately 15 to 40m to each target. Target location uncertainty means that the exact radii to the target were unknown, so there is some variation in this between the sampling for the two target aspects.

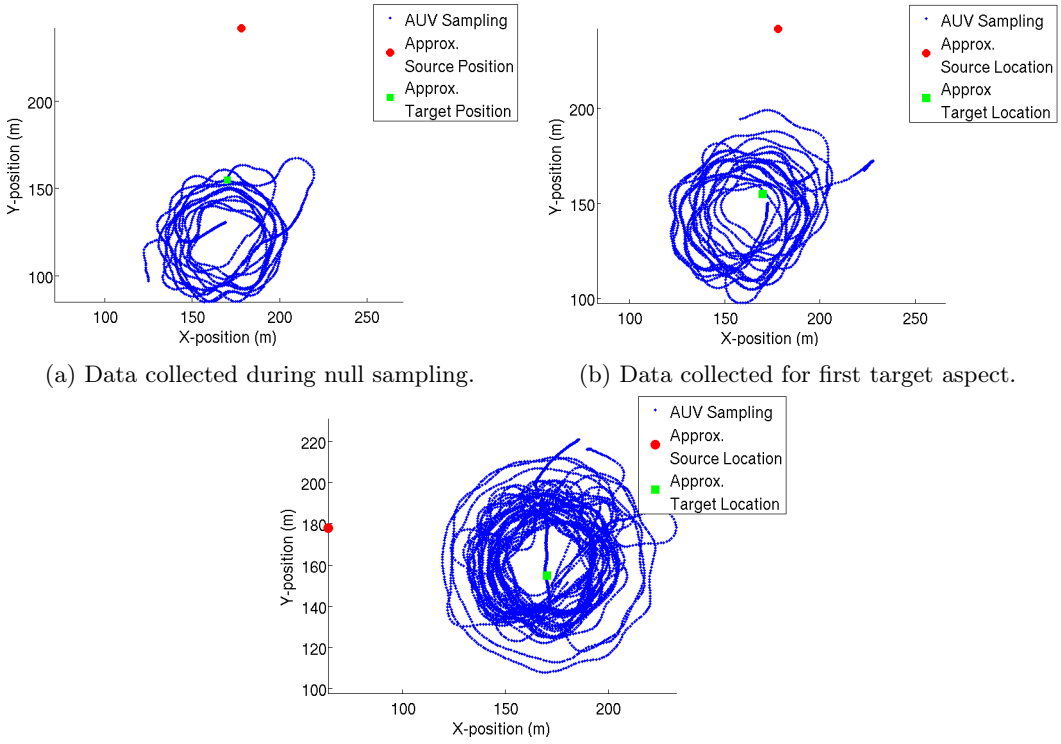

(a) Data collected during null sampling.

(b) Data collected for first target aspect.

(c) Data collected for second target aspect.

Figure 4-16: Sampling for null, first and second target aspect bistatic scattering acoustic data sets.

Aspect dependent bistatic scattering

The amplitude grid for the two aspects, orientation 1 and orientation 2, are shown in Figure 4-17. The radiation pattern polar plots are shown in Figure 4-18.

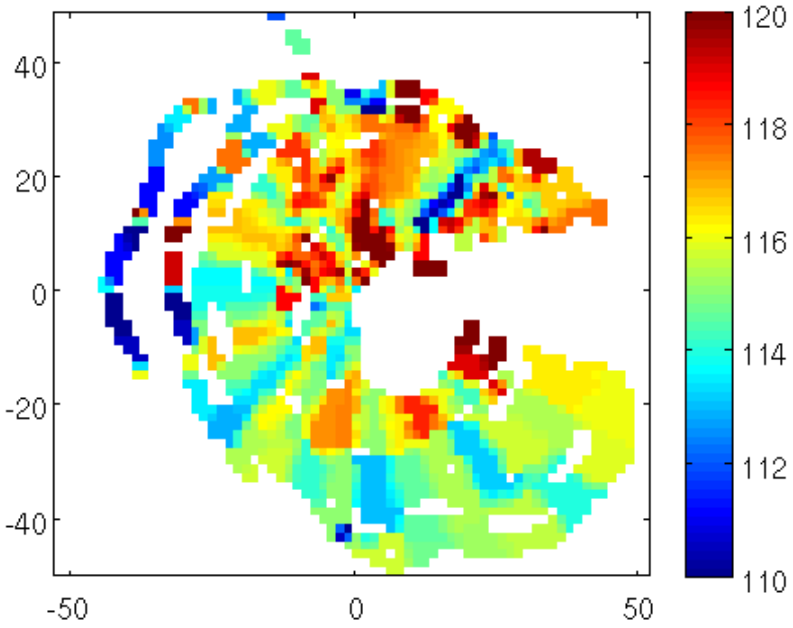

(a) Scattering amplitude map for first target aspect.

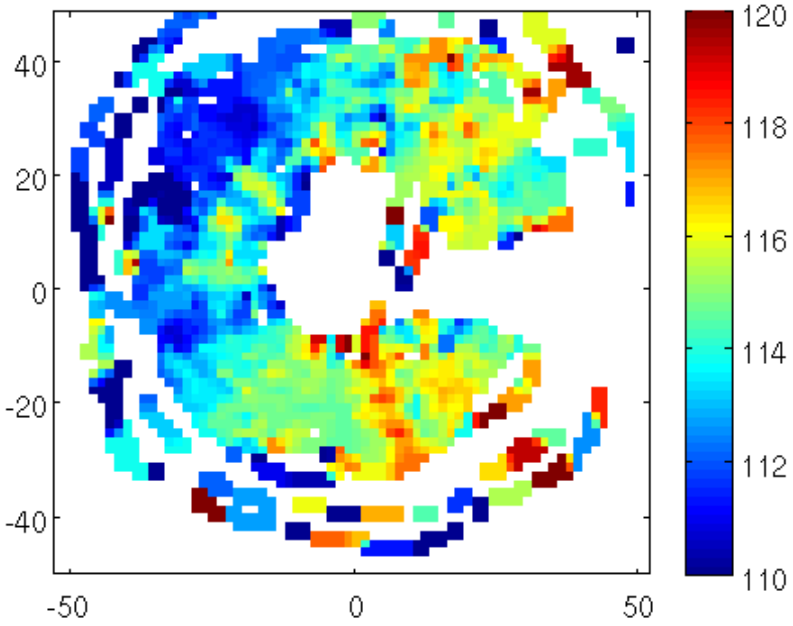

(b) Scattering amplitude map for second target aspect.

Figure 4-17: Unnormalized scattering amplitude maps for 5m depth for the two target aspects during the Massachusetts Bay experiment. For both plots, target is located at (0,0) and source is located at approximately (-100,0).

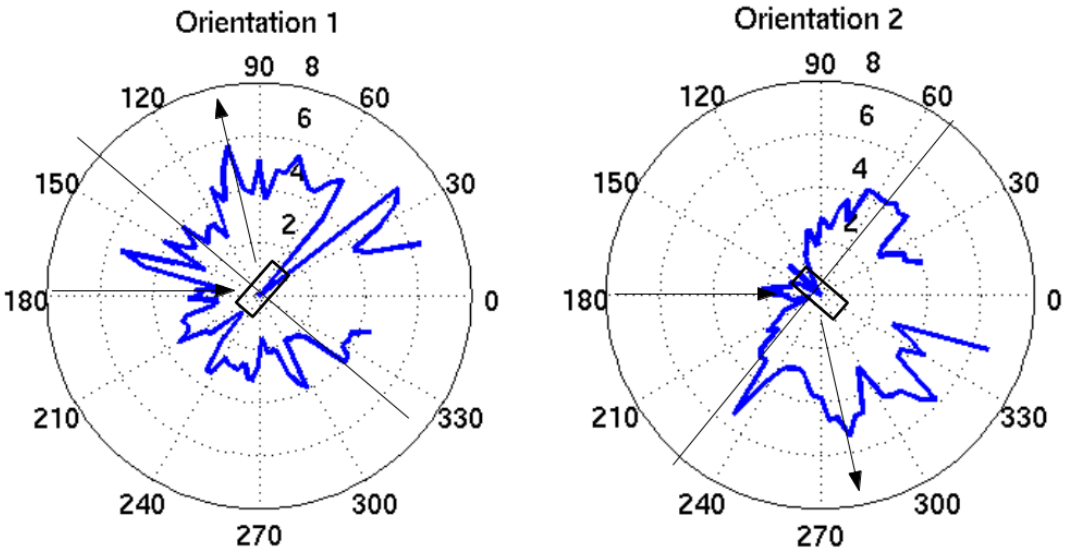

Figure 4-18: Radiation pattern for two target aspects sampled during the Massachusetts Bay experiment. Arrows denote the source arrival and expected glint direction based on reflection.

Null bistatic scattering

The bistatic scattering pattern calculated for the region circled for null data collection was significantly different than that for the two target aspects. The contact amplitudes reported for the region with no target were between 30 and 40dB lower than for the region approximating the location of the steel pipe. The variation in amplitudes was also much smaller. Figure 4-19 compares the unnormalized scattering amplitudes between the first target aspect and the null data set.

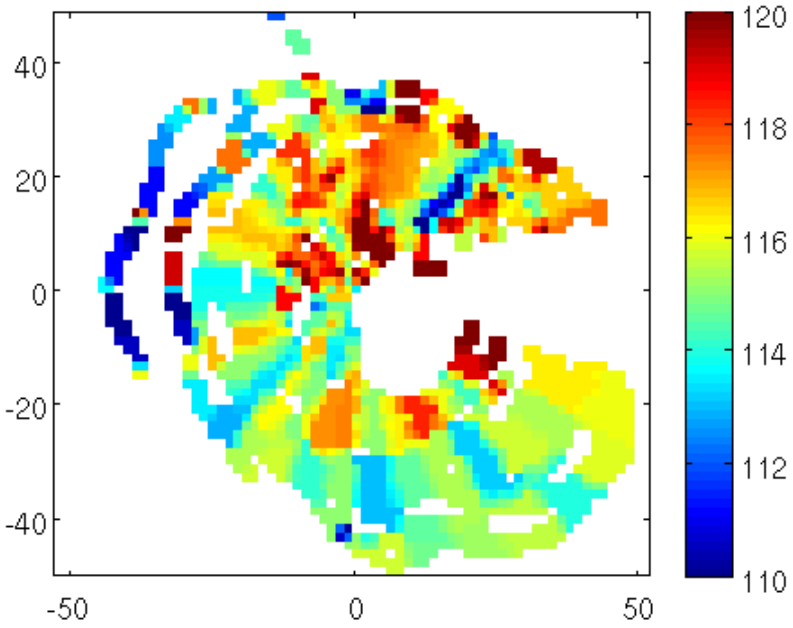

(a) Scattering amplitude map for first target aspect.

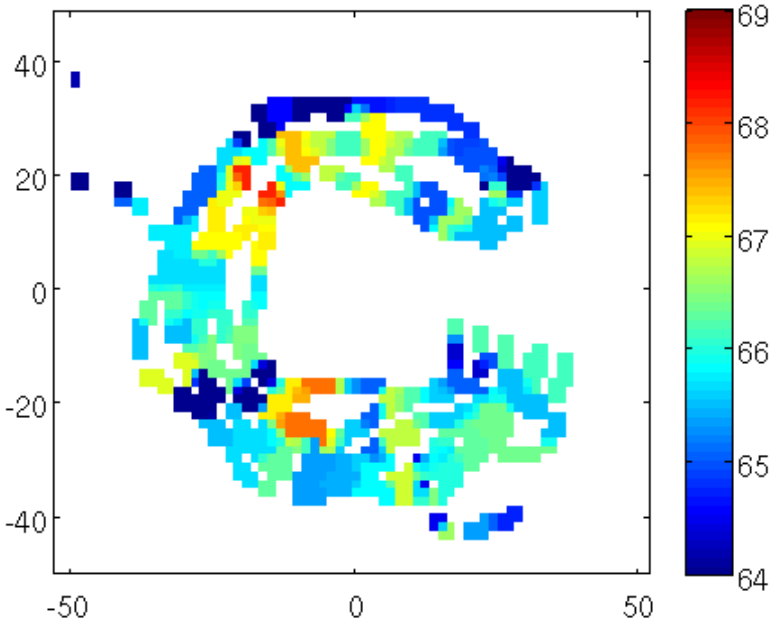

(b) Scattering amplitude map for the null data set.

Figure 4-19: Unnormalized scattering amplitude maps for 5m depth for the first target aspects during the Massachusetts Bay experiment and a region without a target present. For both plots, "target" is located at (0,0). The source is located at approximately (-100,0) for the first target orientation and at (-130,0) for the null target.

4.4 Comparison to Simulation

The scattering simulation package was used to model the expected bistatic scattering fields for the BayEx'14 and Massachusetts Bay experiments. Experiment conditions, source and target geometry were matched as closely as possible given the modelling limitations of the simulator. These simulations were used to develop signal processing and target characterization algorithms in anticipation of real data, to sanity check the measurements collected in the field, and to train regression and classification models to show robustness between simulation and real world.

The range-invariant environment was configured as a series of depth layers. Source frequency, range, and depth are also configured. Bottom parameters were estimated based on diver descriptions of bottom conditions in the BayEx'14 experiment and based on the guess that the bottom was sand in the Massachusetts Bay experiment using values from Table 1.3 in Computational Ocean Acoustics [31]. Water column sound speeds were matched to CTD data collected by the AUV.

4.4.1 BayEx'14 Data Comparisons

The scattering simulation package was used to model the approximate expected scattering fields for the sphere and cylinder in the BayEx'14 experiment. The simulation environment was matched to the mean recorded soundspeed during the experiment, with a 0.5m deep mud layer over sand bottom. The sphere model was a steel shell with characteristics exactly matching those of the sphere in the actual experiment. The scattering simulation package does not currently include an elastic cylinder model, so the real cylinder data could not be exactly compared to simulation. A rigid cylinder model with dimensions and angle relative to the source matching those in the experiment was used instead. The scattering simulation package simulated scattering amplitudes at the locations that *Unicorn* sampled during the experiment around the spherical targets were used to create simulated target scattering data sets.

Figure 4-20 shows a comparison of scattering amplitudes in the 3m depth bin in simulation and real data. The normalized amplitudes are similar for real and simulated data for both the sphere and cylinder, and the cylinder is overall louder. The range of scattering amplitudes is larger for the real sphere than the simulated, and the opposite is true for the

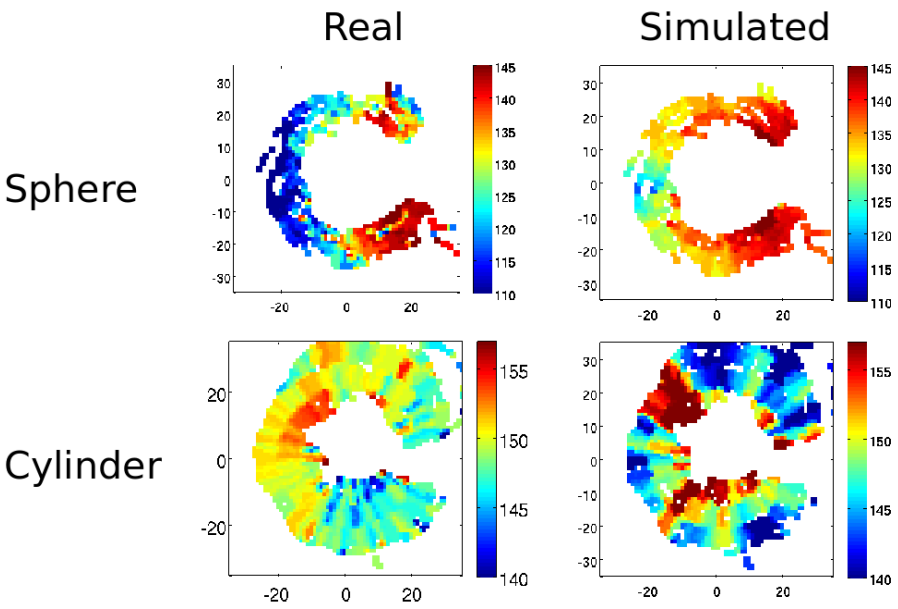

Figure 4-20: Comparison of real versus simulated scattered fields between 2.5 and 3.5m depth for spherical and cylindrical targets.

cylinder.

The sphere real data set shows nearly identical locations of maxima and minima to the simulation. Important features appear in common to both simulation and real models, such as the +/-150^o maxima, 180^o minima and the general pattern from forward to backwards scattering directions.

The cylinder simulation is less similar to the real data, though general location of minima and maxima are consistent between the model and the real data. For example, the glint at 45^o, the maxima around 240^o, the relative maxima at 180^o and 120^o and relative minima at 30^o and 130^o degrees is present in both real and simulated scattered fields. The most obvious difference between the patterns is the greater backscatter intensity in the real cylinder's scattered field relative to the forward scatter intensity. This difference is caused by elastic effects not properly simulated with the rigid cylinder model and multiscatter effects neglected in simulation.

4.4.2 Massachusetts Bay Data Comparisons

The true orientation of the steel pipe in the Massachusetts Bay Experiment was unknown during the experiment: the pipe was dropped off of the R/V *Resolution* without any rotation control. The orientation for each of the two target aspects was instead estimated using

the cylinder orientation regression methodology, described in Section 6.2. In this method, a regression model was trained using scattering simulations of fluid-filled cylinders with aspects of 0 to 180 degrees in 5 degree increments. The angles are measured clockwise when looking at the target from above. The simulation-based regression model was then used to estimate the orientation of the pipe for the two target aspects. The radiation pattern for the first orientation, compared to a field for a simulated 5 foot long, 1 foot diameter water-filled cylinder with a 35^o degree angle, is shown in Figure 4-21. The radiation pattern for the second orientation, compared to a field for a simulated 5 foot long, 1 foot diameter water-filled cylinder with a 110 degree angle, is shown in Figure 4-22. The model's match to the real data is far closer for the 35^o orientation than the 110^o orientation. While the forward-scatter behavior of the scattering pattern diverged in both cases between the simulated closed-ended cylinder and the real, open-ended pipe, the general radiation pattern in the backscatter direction has common features. The simulated scattering fields were generated using a fluid-filled cylinder model, which is only an approximation to the scattered field from a steel open-ended cylindrical shell. The exact bottom type and depth for the experiment site were also unknown, as was the pitch of the target. However, the match between simulated and real data was sufficiently close for a regression model trained on simulation data to be used to estimate the orientation of real data.

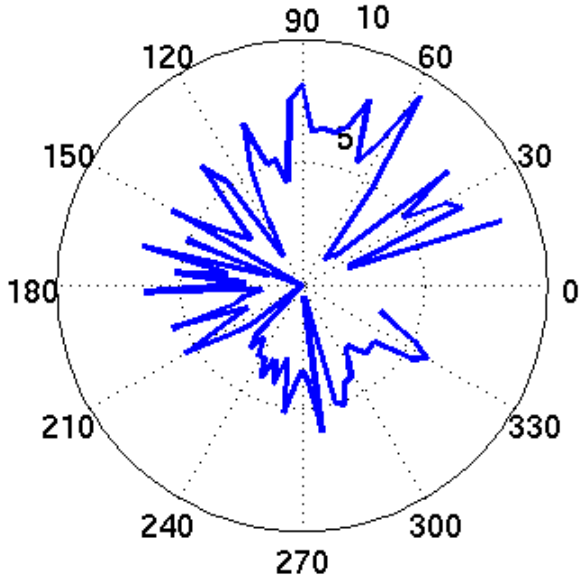

(a) Real scattering field data for target orientation 1.

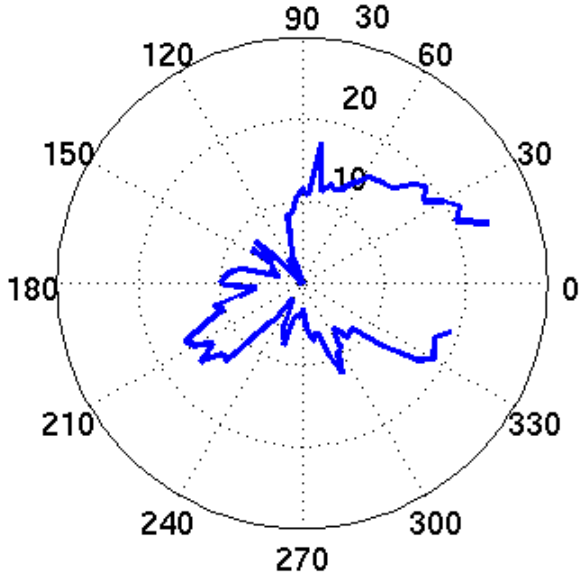

(b) Simulated scattering field data for target orientation 1.

Figure 4-21: Radiation pattern for the first aspect of the real steel pipe, estimated to have rotation 110^o, versus a simulated fluid-filled cylinder with a rotation of 110^o. The match is visually not very close, though there are some similarities visible in the positioning of minima and maxima. The SVM regression model was, despite the differences, able to determine that the real steel pipe was closest in orientation to the modelled 110^o fluid-filled cylinder.

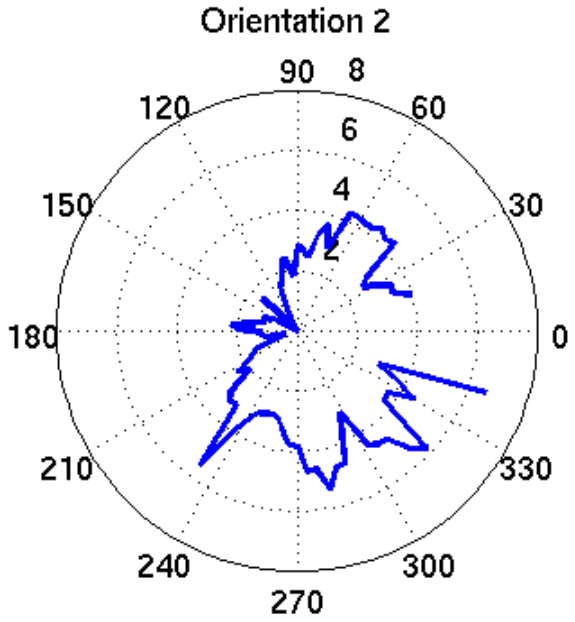

(a) Real scattering field data for target orientation 2.

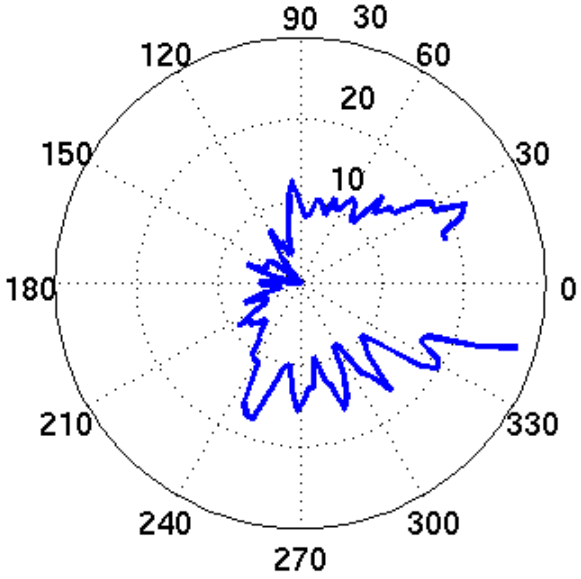

(b) Simulated scattering field data for target orientation 2.

Figure 4-22: Radiation pattern for the second aspect of the real steel pipe, estimated to have rotation 36 degrees, versus a simulated fluid-filled cylinder with a rotation of 35 degrees.

4.5 Summary

The two scattering experiments demonstrated the navigation, timing, and vehicle behaviors necessary for high quality 3D bistatic scattering data collection by an AUV. Navigation problems were addressed with a new IMU that improved drift to less than 0.5% of distance travelled, and by surfacing frequently for GPS. The time synchronization issues were solved using a Chip Scale Atomic Clock as a time source, a Phase Locked Loop data acquisition system, and characterizing all delays to achieve better than $70\mu s$ accuracy. Finally, AUV sampling behaviors were developed to keep the vehicle broadside to the target, resulting in more uniform data quality through the sampling region.

The final system was successfully deployed in two experiments with different environments, source configurations, and targets. During the BayEx'14 experiment, the vehicle acquired sufficient sphere and cylinder scattering data in one day of data collection to compare real data to existing bistatic scattering models. Additional aspect-dependent data was successfully collected in Massachusetts Bay on a steel pipe target using a more realistic configuration, with a ship-based, software triggered omnidirectional source 100m from the target and large uncertainties in target and source locations. The similarity of the real-world processed amplitude data from both experiments to scattering simulation models gave additional confidence that the experimental work was valid. These successful bistatic scattering experiments demonstrated the viability of the AUV payload and behaviors for bistatic acoustic data acquisition in the real ocean and provided real-world data for the classification and regression work discussed in Chapters 5 and 6.

Chapter 5

Classification

As described in the Introduction for this thesis, one of the long term goals of AUV mine-hunting is to be able to deploy a number of inexpensive AUVs in a harbor and have them autonomously classify hazards. Schmidt and Lee [7] showed using simulations that there are distinguishing characteristics of bistatic scattered fields from different targets. These distinctive radiation pattern features were also observed in the data collected during the BayEx'14 experiment between the spherical and cylindrical targets. This chapter describes the methodology and results of a supervised machine learning approach to target classification that uses geometric mapping based on bistatic angle of scattered acoustic amplitudes collected by an AUV between a fixed source and the target. The classification process was demonstrated for sphere versus cylindrical targets with data collected by the MIT Bluefin 21" AUV *Unicorn* as a part of the BayEx'14 experiment conducted in St. Andrews Bay off of Shell Island near Panama City, FL in May 2014.

This chapter first discusses the methodology for classification, consisting of an offline training and analysis phase and the subsequent onboard classification of targets. Simulation and real-world procedures are then presented, along with feature selection and confidence estimation methods. The results are shown from applying this methodology for the classification of real-world spherical versus cylindrical targets using machine learning models generated with data from the BayEx'14 experiment and simulation.

5.1 Methodology

The goal of this research was to demonstrate the plausibility of classifying underwater using bistatic scattered amplitudes calculated by an AUV from acoustic data collected between the source and target. Two data sets were used for this demonstration, a real bistatic scattering data set collected around spherical and cylindrical targets during the BayEx'14 experiment (see section 4.2), and a simulation data set matched as closely as possible to the experiment conditions (see section 2.2).

5.1.1 Machine learning approach

Supervised machine learning was selected to address the challenge of classifying targets using amplitude-only bistatic acoustic data. In a machine learning approach data is represented using example vectors in a particular feature space, and used to train a model that can be used to classify subsequent data. This approach has drawbacks and benefits. Because the method is dependent on well-represented data instead of a physical model, it can be more susceptible to 'garbage in, garbage out', and poor independent testing can lead to misleadingly good results. However, with sufficient care in problem construction and validation machine learning can be very powerful, as it accounts for effects that show up in real data but are neglected in conventional models.

For this problem, I selected a type of supervised machine learning called support vector machines (SVMs). SVMs were selected for this problem for several reasons. They handle large feature spaces easily, adapt well to different kernels, and have well-implemented off-the-shelf optimization packages. Perhaps most importantly for this real time application, while SVMs can take significant time and memory to train, classification using an existing model is fast. SVM classification of an example vector also results in a margin which is an indication of the strength of the classification.

SVM classification works by maximizing the minimum euclidean distance from a separating hyperplane to the set of training vectors. The soft-margin SVM classification formulation, originally derived by Vapnik [32], is used:

$$\underset{\mathbf{w},\xi,b}{\operatorname{argmin}} \frac{1}{2}\|\mathbf{w}\|^2 + C\sum_{i=1}^{l}\xi_i$$
$$s.t. \begin{cases} y_i(<\mathbf{w}, \mathbf{x_i}> +b) \geq \xi_i \\ \xi_i \geq 0 \end{cases} \tag{5.1}$$

where $\mathbf{w}$ is the normal vector to the separating hyperplane that defines the binary classification, ξ is the slack variable that allows the optimization to deviate from perfect classification in the selection of a solution, C is used to adjust the trade-off between the size of $\|\mathbf{w}\|$ and the tolerance for misclassification, and b is the offset from the origin of the classification solution. $\mathbf{x_i}$ is the i^{th} example vector and y_i its label (1 or -1).

A training data set, $\mathbf{X_t}$, for the SVM is represented as:

$$\mathbf{X_t} = (\mathbf{x_1}, y_1), ..., (\mathbf{x_l}, y_l) \subset \chi x \mathbb{R}. \tag{5.2}$$

where χ represents the space of the input, such that $\chi = \mathbb{R}^d$ if there are d features.

This optimization selects a separating hyperplane that maximizes the minimum distance, or margin, from the nearest training data points to the hyperplane, subject to the set of conditions.

The SVM-Light[33] software package was used for this optimization. The trained SVM model can be represented by $\mathbf{w}^*$, which is the normal vector to the separating hyperplane selected by training. This separating hyperplane can be used to classify new data.

Any new data, $\mathbf{x_i}$, is classified by comparing it to the separating hyperplane. This results in a margin, a, which is the euclidean distance from the test example to the separating hyperplane, and is calculated as the dot product of $\mathbf{w}^*$ and the new example $\mathbf{x_i}$.

$$a =< \mathbf{w}^*, \mathbf{x_i} > +b \tag{5.3}$$

If $a > 0$, the class is positive, if $a < 0$, the class is negative. A larger margin indicates that the model ascribes greater confidence to an example vector. For the purposes of this thesis, a_+ will be used to represent margins from examples that come from the positive

class (spheres), and a_- will be used to represent margins from examples the come from the negative class (cylinders).

Performance Metrics

Assessing the validity of a given model is very important to the success of this methodology. Two metrics are used in this paper: test accuracy and test minimum margin ratio. Test accuracy is simply the accuracy of classification of the examples in the test set. The test set is independent of the training set and the validation set used in selecting SVM model parameters. Positive margin ratio is the ratio between the largest true positive margin and the largest false positive margin, i.e. the ratio between the strongest true sphere classification and worst false sphere classification. The minimum margin ratio is the minimum of positive and negative margin ratios:

$$\beta_{min} = min \left\{ \frac{max(\mathbf{a}_+ > 0)}{max(\mathbf{a}_- > 0)}, \frac{max(\mathbf{a}_- < 0)}{max(\mathbf{a}_+ < 0)} \right\} \tag{5.4}$$

If β_{min} is less than 1, a classification can always be wrong no matter how large the margin. The larger the value of β_{min}, the greater the utility of classification and the better the confidence model.

A number of steps were required to go from a scattering data set to a SVM-trained model being used on an AUV. The approach taken for classification of spherical versus cylindrical targets has two parts: an offline training and analysis segment, and the onboard target classification, conducted in real time.

5.1.2 Training and Analysis

The training and analysis procedure breaks into several parts, as shown in Figure 5-1. This process was demonstrated using both simulated and real data.

Data Acquisition

The first step in training and analysis was acquiring or generating data for that full 3D scattered field used to generate classification and confidence models.

In the real world experiment, the grid of amplitude data was collected around each target using the AUV *Unicorn* following a sampling behavior developed for collecting the best

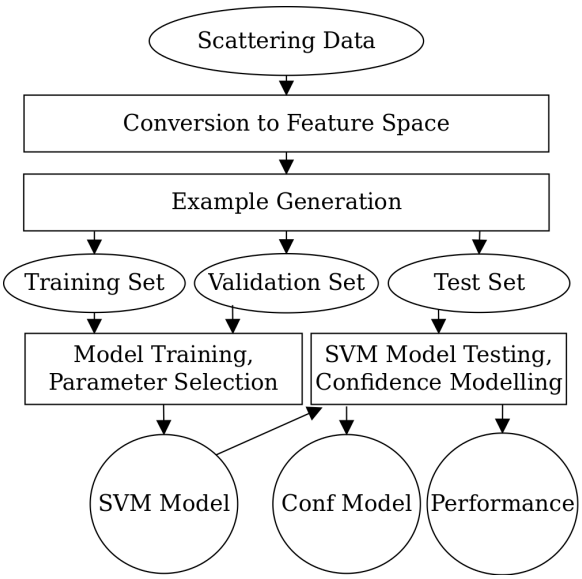

Figure 5-1: Training and analysis process for machine learning methodology. Acoustic scattering amplitude data is converted to a feature space and used to construct example vectors. Independent example vectors form training, validation, and test data sets. Classification model training is conducted on the training set, and the validation set is used in the selection of model parameters. The test set is then used to determine the model's generalization performance and construct a confidence model, used to estimate the probability of correct classification given the number of samples and the classification margin.

possible bistatic data set. In this full-field sampling behavior, the vehicle followed concentric circles around the target so that it remained fully broadside to the target, transitioning in range in the forward-scatter direction in the region where sampling results in the poorest target scattering data. This was repeated at a sequence of depths. Each second, the vehicle's calibrated data acquisition system began recording exactly on the second. The onboard signal processing chain then extracted the amplitude for each target of interest from the recorded acoustic data file, subtracting the ambient noise. The signal processing used to go from 16 elements of array data to an acoustic amplitude is shown in Figure 4-2. This process uses time windowing based on vehicle/target location, matched filtering, beamforming, and selection based on estimated contact location to determine the target's scattering amplitude. The result was a grid of bistatic scattering amplitudes in range, depth and azimuth around each target.

In simulation, the 3D data was generated using the OASES-SCATT acoustic package to simulate the scattered fields of both target types in the frequency range of the LFM chirp used in BayEx'14. Appendix A shows the parameters used in generating the data from OASES-SCATT. The sphere parameters were able to be matched very closely using an elastic fluid-filled shell in the model. However, OASES-SCATT does not currently include a elastic cylinder model, so the cylinder was modelled as rigid with the same dimensions and orientation as the real solid aluminum cylinder. This gave the closest result given the limitations of the simulation package. The outputs of this process were files containing the azimuthal Fourier orders for the sphere and cylinder scattered fields. This data was converted into a grid of amplitude values in range, depth, and azimuth. It is this grid that was used in SVM example generation.

Feature Selection

The presentation of the data is one of the critical aspects for successfully using machine learning for this problem. For SVMs, this takes the form of the feature representation used for example vectors.

Image-based and other complex feature representations were rejected for this problem because a sparse sampling from the scattered field had to be effective for classification and because classification had to take place in real time. Instead, each sample is mapped to a feature number based on the bistatic angle of the sample. This feature space was motivated

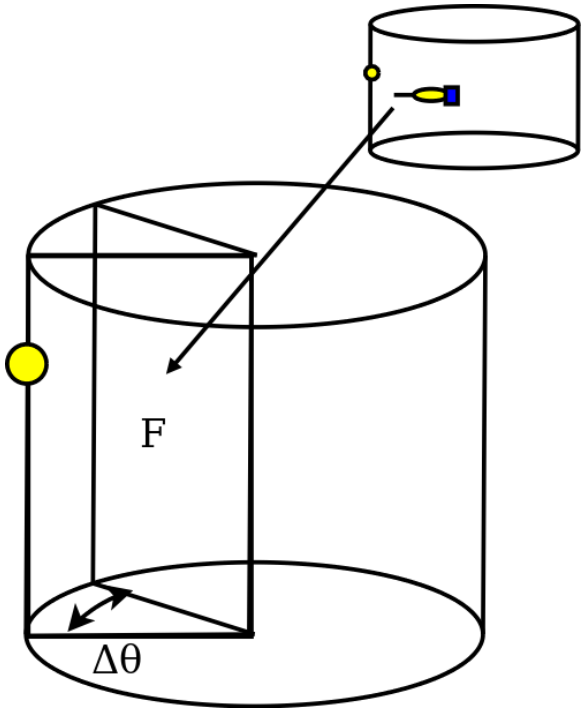

Figure 5-2: Angularly dependent feature space, configured using parameter $\Delta\theta$.

by the observation that the greatest difference between scattering patterns output by the scattering simulator was in the angular location of minima and maxima within the radiation pattern. Amplitudes are mapped to features using the bistatic angle of the samples, allowing the model to exploit the differences between different angles. This feature space was defined in purely spatial terms, meaning that the model does not take into account sampling order. A representation of the angular feature space is shown in Figure 5-2.

Each example vector consisted of a sequence of feature-value pairs, where each value is the median scattering amplitude sampled within the angular region defined by the feature number. The feature number, F_n, was calculated as a function of the location of a sample's angle relative to the source-target line, (θ_s), and a bin size in azimuth, $\Delta\theta$.

$$F_n = \lfloor \tfrac{\theta_s}{\Delta\theta} \rfloor \ . \tag{5.5}$$

When multiple samples are collected from the same feature, the median amplitude is taken. For example, if there are three samples at points that map to feature F_n, the value A_n will be the median of the three amplitude values. This calculation is performed for each geometric point the AUV has sampled, such that the feature vector is composed of a number

of feature-value pairs and the label y_i is the target's class.

$$\mathbf{x_i} = \{[F_1, A_1], ..., [F_N, A_N]\}$$
$$y_i = \begin{cases} 1\, if\ sphere \\ -1\, if\ cylinder \end{cases} . \tag{5.6}$$

This is a rapid calculation that can easily be performed on an AUV. The value of parameter that describes the feature space, $\Delta\theta$, was selected using a design of experiment (DOE) search shown in Algorithm 1.

Algorithm 1 Calculate $\mathbf{\Delta}\theta^*$

$i \leftarrow 0$
$\boldsymbol{\Delta\theta_0} \leftarrow [\Delta\theta_{0,min}, \Delta\theta_{0,min} + (\Delta\theta_{0,max} - \Delta\theta_{0,min})/2, \Delta\theta_{0,max}]$
while $max(\boldsymbol{\theta_{step,i}}) - min(\boldsymbol{\theta_i}) > 1$ **and** $\mathbf{\Delta}\theta^*_\mathbf{i}! = \mathbf{\Delta}\theta^*_{\mathbf{i-1}}$ **do**
  $\Delta\theta^*_i = FindBestPoint(\boldsymbol{\Delta\theta_i})$
  $\boldsymbol{\Delta\theta_{i+1}} = RefineGrid(\boldsymbol{\Delta\theta_i}, \Delta\theta^*_i)$
  $i = i + 1$
end while

Algorithm 2 $FindBestPoint(\boldsymbol{\Delta\theta_i})$

$V_{max} \leftarrow 0$
for $\Delta\theta$ in $\mathbf{\Delta}\theta_\mathbf{i}$ **do**
  $V = Value(\theta)$
  if $V > V_{max}$ **then**
    $\Delta\theta^* \leftarrow \Delta\theta$
  end if
end for
return $\Delta\theta^*$

Algorithm 3 $RefineGrid(\mathbf{d_i}, d^*_i)$

$\Delta = max(\mathbf{d_i}) - min(\mathbf{d_i})$
if $d^*_i + \Delta/2 \leq max(\mathbf{d_i})$**and** $d^*_i - \Delta/2 \geq min(\mathbf{d_i})$ **then**
  $\mathbf{d_{i+1}} = [d^*_i - \Delta/4, d^*_i, d^*_i + \Delta/4]$
else if $d^*_i + \Delta/2 \geq max(\mathbf{d_i})$**and** $d^*_i - \Delta/2 \geq min(\mathbf{d_i})$ **then**
  $\mathbf{d_{i+1}} = [d^*_i - \Delta/4, d^*_i, d^*_i + \Delta/2]$
else if $d^*_i + \Delta/2 \leq max(\mathbf{d_i})$**and** $d^*_i - \Delta/2 \leq min(\mathbf{d_i})$**and** $d^*_i - \Delta/2 \geq 0$ **then**
  $\mathbf{d_{i+1}} = [d^*_i - \Delta/2, d^*_i, d^*_i + \Delta/4]$
else
  $\mathbf{d_{i+1}} = [d^*_i - \Delta/4, d^*_i, d^*_i + \Delta/4]$
end if
return $\mathbf{d_{i+1}}$

Additional feature spaces were explored but are not discussed here because they resulted in models vastly inferior to those produced using the angularly dependent feature space. The algorithms for these additional feature spaces, and a comparison of performance of different feature spaces, are described in Appendix B.

Example Generation

Once the full grid of scattered field amplitude data is represented in terms of the feature space, training, validation and test example vectors are constructed. Each example should represent the data collected by an AUV approximately circling a target for some time τ. Because the vehicle collects one acoustic file each second, this involves collecting $N = \tau$ samples. To properly simulate this while constructing example vectors for simulation data, each angular feature is sampled either m, $m-1$ or $m+1$ times, where $m = \lceil N/n_F \rceil$ if n_F is the number of features in the feature space defined by $\Delta\theta$. The median is taken when more than one sample is taken for a particular feature. The full set of example vectors was split into three independent data sets, such that 50% of examples were used for training set $\mathbf{X_t}$, 25% for validation $\mathbf{X_v}$ and 25% for testing $\mathbf{X_x}$ as suggested by Hastie et. al. in The Elements of Statistical Learning [34].

For real data, the data set collected during the BayEx'14 experiment for the sphere and cylinder targets was used to directly create example vectors. The data set was broken into three parts: half for training, a quarter for validation and a quarter for testing. Examples were then created from each set by selecting N sequential data points at a time. If the set of amplitudes designated for training is represented by $\mathbf{A_t} = [(\theta_0, A_0), (\theta_1, A_1), ...(\theta_M, A_M)]$ the first example would be created using the data $[(\theta_0, A_0), (\theta_1, A_1), ...(\theta_N, A_N)]$ and the second example would be created using the data $[(\theta_1, A_1), (\theta_2, A_2), ...(\theta_{N+1}, A_{N+1})]$. This process is repeated until $N+i = M$. The training, validation, and test data are kept entirely independent, such that if the full sphere data set consisted of 2000 data points the first 1000 data points would be used for training, the next 500 for validation and the final 500 for testing. This ensures that performance is tested realistically, on sequential data collected by the AUV that is separate from data used in model training. The value of N was varied to observe the relationship between amount of sampling and classification accuracy. nEx_t examples are generated in the manner for training, nEx_v for validation and nEx_c for testing.

Model Training and Analysis

An SVM model was trained using the training set. SVM-light [33] [35], developed by Thurson Joachims, was used for the actual model training and data classification.

The parameters for the SVM model were selected using a logarithmic grid search in C, using the training set to train a model then classifying the validation set. Once a good model was selected, the test set was used to ensure that model selection did not lead to falsely positive results. Training sets were generated with different numbers of training examples and classified on the fully independent test set to confirm that the amount of data being used to train the model was appropriate.

Confidence Estimation

Confidence estimation is an essential part of target classification: while an SVM outputs the class (sphere or cylinder) and distance to the separating hyperplane in the classification margin a, that value does not translate directly into a probability of correct classification. Specifically, we want to know the probability of correct classification, given the classification margin and the amount of data collected by the vehicle $P(\tilde{y}_i = y_i | a \geq a_i, N)$, where a_i is the margin, $\tilde{y}_i$ is the estimated class, y_i is the true class and N is the number of samples collected by the AUV while circling the target. This probability was calculated empirically by using the final SVM model to classify sets of example vectors that represent different values of N. The results were converted into a lookup table for rapid confidence calculation in real-time.

5.1.3 Onboard target classification

Real-time classification of targets onboard an AUV requires a number of elements. Once the SVM model and confidence model are trained, they are used perform real-time target classification. These processes are run within MOOS-IvP, which allows nearly seamless runtime/simulation trade-off and gives a way to test signal processing on the bench with simulated or logged data.

The final processing chain (Figure 5-3), using the results from training, includes synchronous and asynchronous components and has been demonstrated in simulation and bench tests to be able to run in real time on data collected by the AUV-Unicorn using the 16-

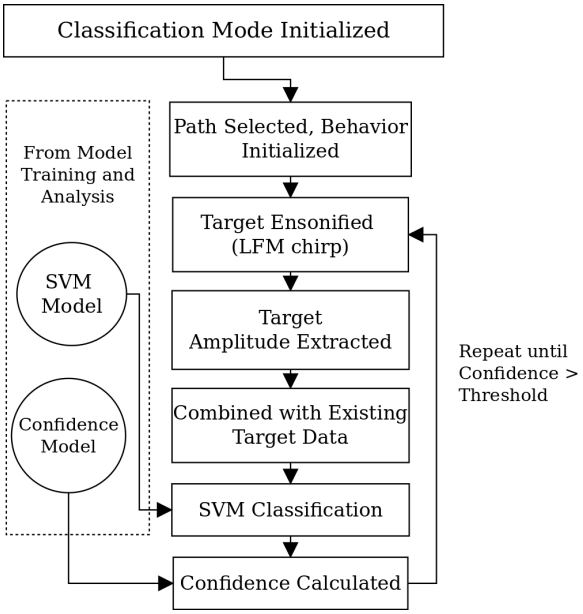

Figure 5-3: Classification processing chain run onboard an AUV.

element array.

Classification Mode Initialized

Each second, the data acquisition system records the first 0.21 s of data, which should include the direct blast from the source and target contacts that may be of interest. The target contacts are extracted from the data and tracked. Each target report includes target locations and confidence. Once a target's location has some confidence, it can be prosecuted by initiating classification.

Vehicle Behavior

To give the best classification result, the AUV is commanded to approximately circle the target. This gives sampling of all angular features.

Amplitudes Extracted

The MOOS processes used for the signal processing required to extract amplitudes in simulation and runtime are shown in Figure 6-5. On the real vehicle, data is recorded each second to a file which is then read by pActiveTargetProcess, which performs the matched filter, beamforming, and selection to choose the contact amplitude from the target of interest.

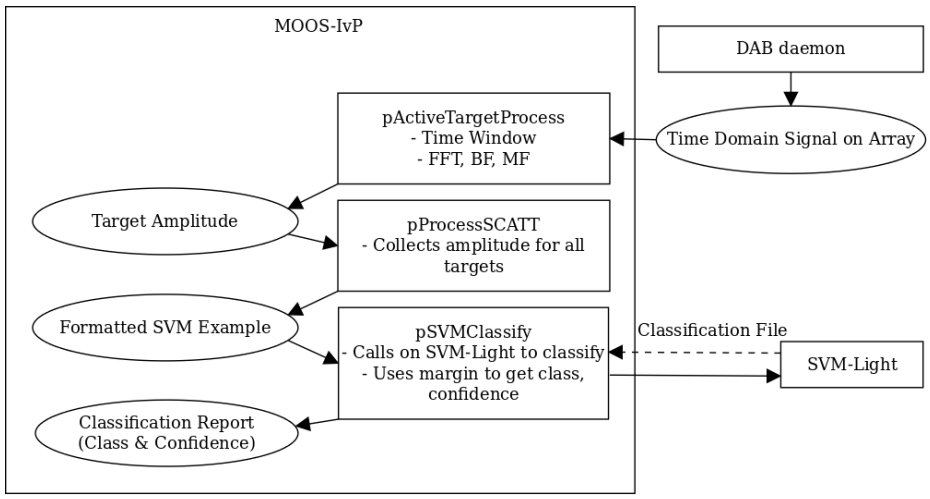

(a) Runtime classification processing chain.

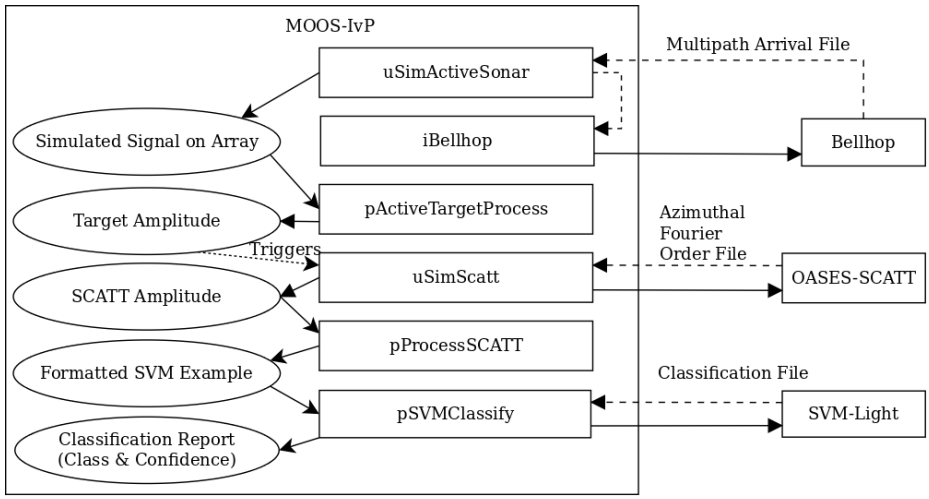

(b) Simulation classification processing chain.

Figure 5-4: Real-time classification processing chains for runtime and simulation.

Average intensity over the frequency band is used. In simulation, an acoustic simulator, uSimActiveSonar_shallow, was developed to simulate multipath bistatic acoustic arrivals on a simulated array. This multipath is combined with simulated scattering data in uSimSCATT to simulate amplitudes collected by the AUV as it passes through a scattered field.

Target Classification and Confidence Estimation

The amplitudes in simulation or runtime are converted to the correct feature space by another MOOS process, pProcessSCATT. An SVM model was specified to the SVM interface application, pSVMClassify, which then ran classification on the amplitude data. The full process runs continuously as data is collected by a real or simulated AUV, constantly up-

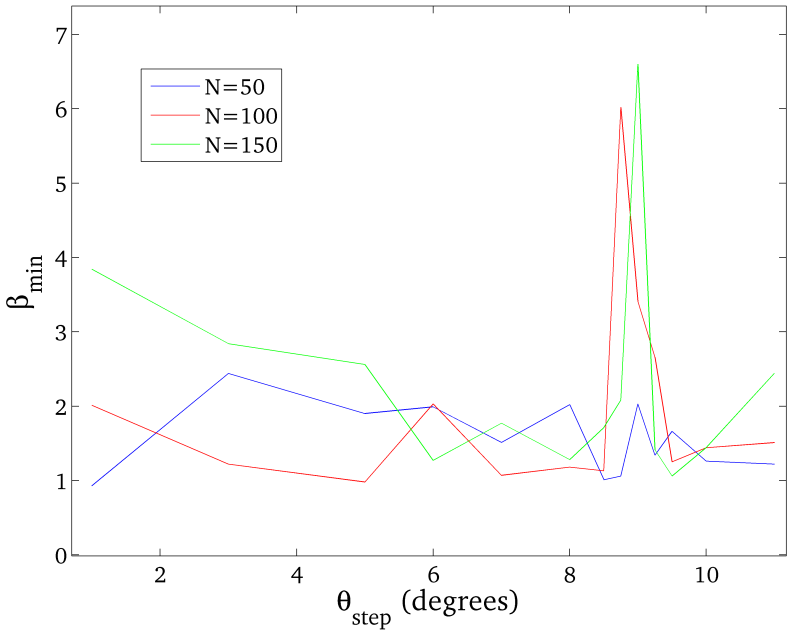

Figure 5-5: Selection of $\Delta\theta$ based on the minimum margin ratio, β_{min}, at increasing values of N. $\Delta\theta = 9^o$ was selected because it converged most quickly to $\beta_{min} = \infty$ as the accuracy reached 100%.

dating classification and confidence until a confidence threshold was met for the target.

5.2 Results

5.2.1 Feature and SVM Parameter Selection

Algorithm 1 was used to select the value for $\Delta\theta$ used in the feature representation for the SVM models for this problem. The value of $\Delta\theta = 9^o$ gave the best performance in terms of minimum margin ratio when a model was trained and validated on real data. This value also gave good performance for a model trained on simulation data and used to classify real data. The relationship between β_{min} and $\Delta\theta$ for some of the tested values of N is shown in Figure 5-5. Larger values of N are not plotted because as N increases the value of β_{min} approaches infinity as accuracy goes to 100%. The plot clearly shows the best feature space at $\Delta\theta = 9^o$.

A linear SVM model performed extremely well with the angularly dependent feature space used for classification. The minimized the complexity of the model and meant that additional parameters did not need to be selected- adjusting the value of C did not affect

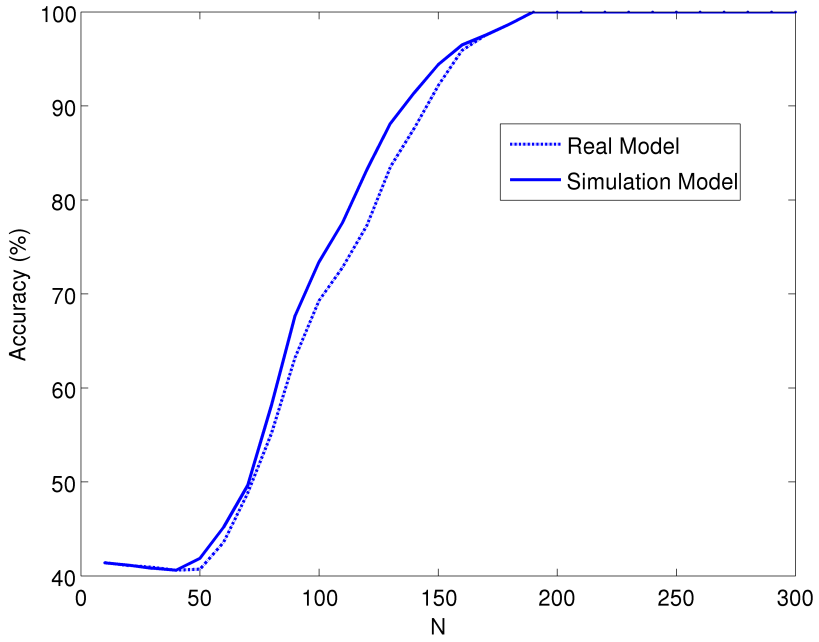

Figure 5-6: N versus accuracy for model trained on real and simulated data with feature space where $\Delta\theta = 9^o$. As N increases, the accuracy increases until it reaches 100%. This behavior is expected, as additional data improves the averaging in each feature. After $N = 190$ the accuracy goes to 100%. When $N = 190$, the vehicle has generally completed two circles of the target.

the model in this case as the complexity was at a minimum.

5.2.2 Training and Analysis Results

Two models were used in training and analysis. The first was trained based on the real bistatic data collected during the BayEx'14 experiment, the second on simulation data matched to the environment of the BayEx'14 experiment.

Training on Real Data to Classify Real Data

Data from the real experiment was turned into training examples and then a linear SVM classification model using the methodology described in Section 5.1.2. The test set was classified using the resulting trained model. The accuracy of the resulting classification was highly dependent on the value of N, which translates to the number of seconds of data acquisition. A plot of accuracy versus N is shown in Figure 5-6. Overall, the SVM model was very effective for classifying independent test example vectors once the vehicle had

completed at least one full circle around the target. With two complete circles of the target, the accuracy of the model in classifying new test examples reaches 100%.

Training on Simulation Data to Classify Real Data

As described in Section 4.4.1, the simulated scattering fields are a good match to those calculated from the real world BayEx'14 scattering data. To show empirically that this was the case, a SVM model was trained using the sphere and cylinder simulation scattering models and used to classify the same sets of example vectors used to test the SVM model trained on real data. The classification results for the real test examples were very similar using the simulated-data-based model and the real-data-based model. Figure 5-6 shows the plot of classification accuracy versus N classifying the test example set using the real and simulated SVM models. The trend for accuracy v. N is nearly identical in the two cases. The model based on simulation data slightly outperforms the model based on real data (higher accuracy with fewer amplitude samples), likely because the simulation data contains the same major features as the real data but without as much noise. The similarity of these results suggests that, at least for simple targets, a simulation approach could be used to augment real data in constructing SVM models used to classify targets in new environments. However, the power of the machine learning approach remains the flexibility to deal with targets and environments that are not easily modelled numerically or analytically by using real data to construct a model.

5.2.3 Confidence Models

The curves describing the empirically determined confidence in correct classification versus classification margin a for different values of N is shown in Figure 5-7. The general behavior shows an approximately logistic relationship between a and confidence. As N increases, the probability of correct classification from a lower output margin also increases. Once N increases past 190, the confidence of correct classification approaches 100% for all margin values, indicating no false classifications. The performance at different values of N and estimated confidence as real scattering data is collected would be used to inform vehicle behaviors during classification.

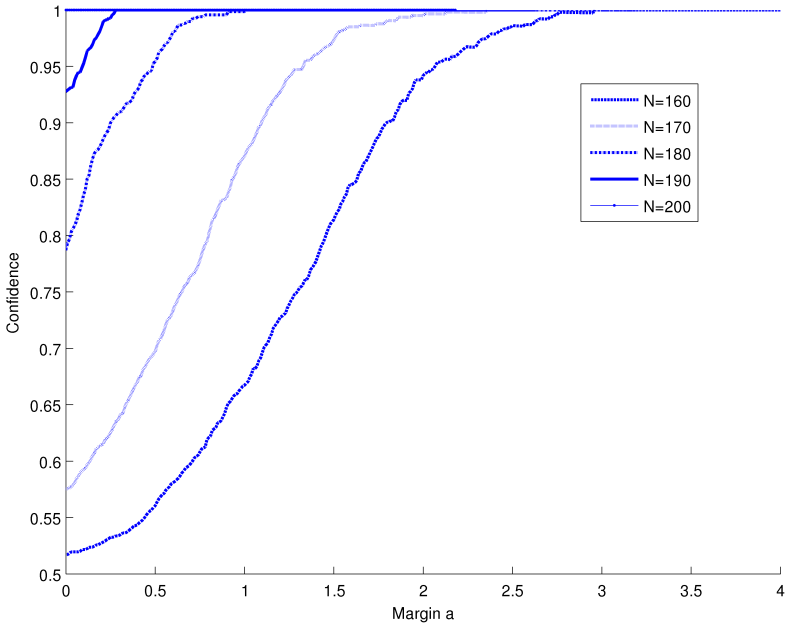

Figure 5-7: Classification confidence versus margin and N for sphere versus cylinder classification.

5.2.4 Real-time Classification

The use of real and simulated models for real-time classification was tested in simulation. uSimSCATT passed either simulated scattered field amplitudes or data from the experiment to the SVM example synthesis and classification processes, resulting in a classification and confidence. Simulation studies and bench tests with the vehicle computer show the full processing chain successfully completing each second: pActiveTargetProcess takes around 0.3s to calculate the target amplitude from an acoustic file, the incorporation of acoustic data into the existing SVM example for classification takes less than 0.05s, and the actual classification, which is only run when the vehicle exits a feature (about every 5 seconds), takes less than 0.5s. This shows the plausibility of using this method for real-time analysis and classification. These numbers were shown on the bench with the *Unicorn* computer when only the classification processing chain was running. Adding the target localization processing chain increases processing times significantly so that the acoustic data was fully processed only once every 3 seconds instead of every second. To simultaneously run localization and classification processing on *Unicorn* every second, a more powerful computer would be required.

5.3 Summary

Classification of spherical versus cylindrical targets using scattering amplitude data collected by an AUV was successfully demonstrated using real and simulated target scattering data. Furthermore, it was shown in simulation on the bench that all processes required for target classification using this methodology can be run in less than a second, which means AUV-based real-time classification and confidence estimation are plausible. While the sphere versus cylinder classification investigated here is a simplification of the target geometries of interest in mine countermeasures, this research shows the potential of the combination of sensing bistatic scattering fields with a linear array payload and applying machine learning classification of calculated acoustic amplitudes for solving the real-time target classification problem.

Chapter 6

Regression

To fully characterize a seabed target based on its bistatic acoustic scattered field, a regression process is required in addition to classification. For example, in the simple sphere versus cylinder case, the orientation of the cylinder has a large affect on the positioning of maxima and minima in the bistatic radiation pattern. In this scenario, a classification model would be trained to include a range of target aspects. Once the cylindrical nature of a target was determined, the orientation would be estimated using regression and the target re-classified using that information for greater confidence. The configuration for the estimation of the orientation of an aspect-dependent target is shown in Figure 6-1.

Environment can also have a large affect on the scattering pattern. In particular, the angle of any directional rippling in a sandy bottom can significantly impact the acoustic scattering field of aspect-dependent targets in the 1-5kHz frequency range. If the source position relative to the target is adjusted using an estimate of this ridging angle, the effect of the bottom on the target's bistatic scattering field can be minimized as discussed by Lee in his thesis [9]. A schematic of an AUV performing sampling to estimate the angle of the bottom anisotropy is shown in Figure 6-2. This effect is not significant in the frequency range used in the BayEx'14 and Massachusetts Bay experiments, but could have a large impact for the characterization of buried targets being insonified using lower frequencies.

These two problems are similar enough that the same machine learning regression methodology could be applied to both. Simulated acoustic scattered fields were generated using the scattering simulation package, and used to create training, validation and test sets. SVM regression was used to train a model, which was evaluated using validation and test example

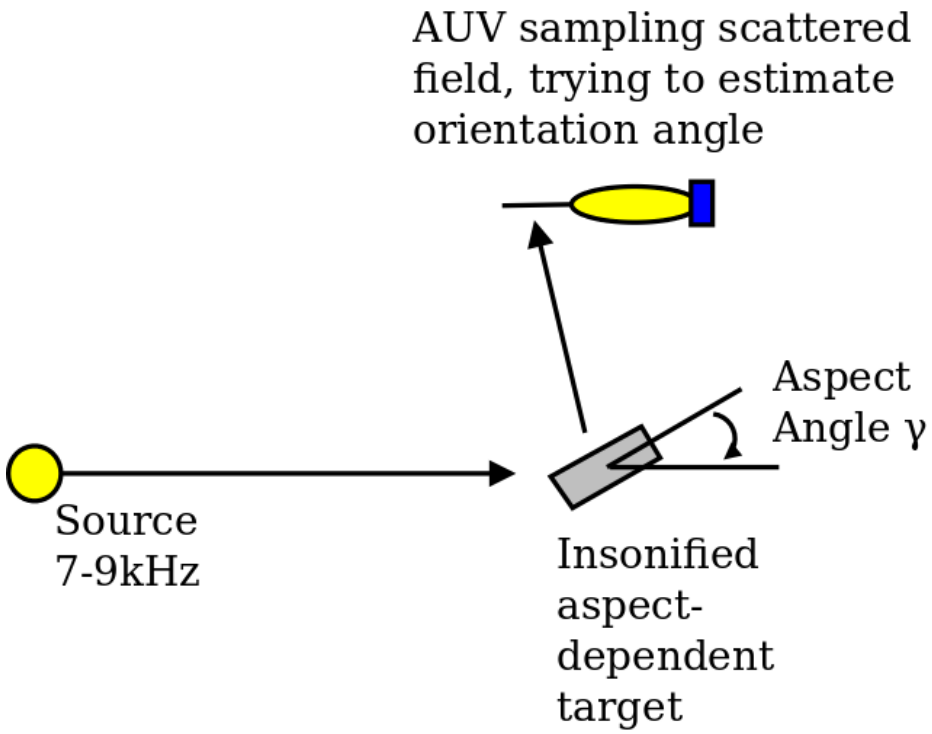

Figure 6-1: Schematic on the use of an AUV for estimation of a target's aspect using sampled bistatic acoustic scattered field data. Like in the Massachusetts Bay experiment, a ship-based source insonifies a target using a 7-9kHz signal as an AUV sampled the resulting scattered field and uses the collected amplitude data to estimate the orientation angle of the target relative to the source.

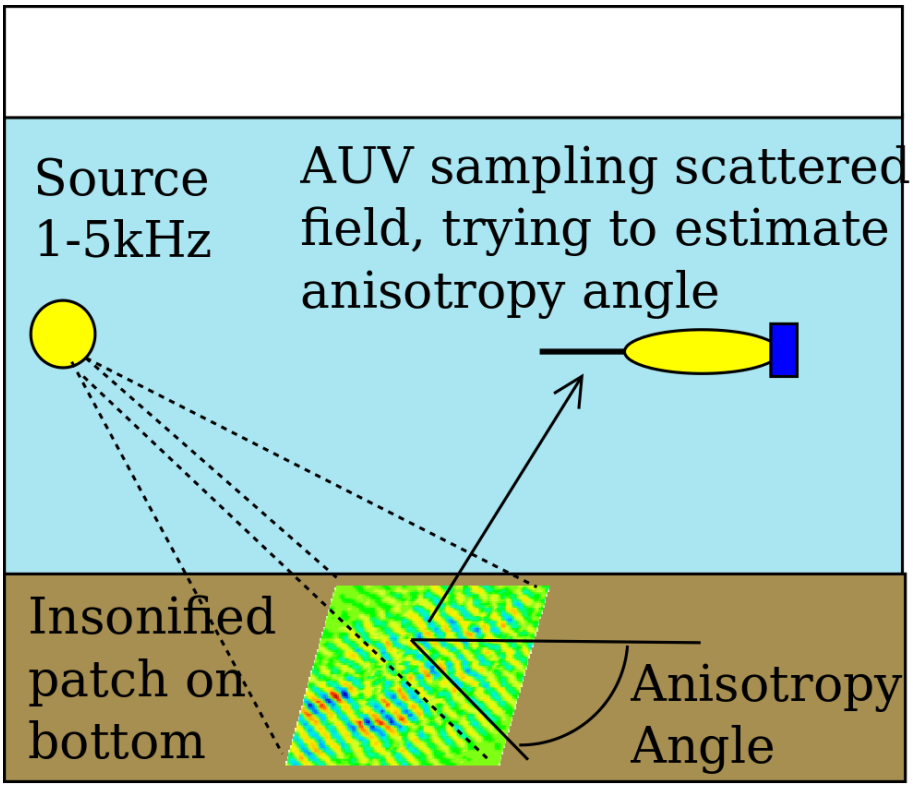

Figure 6-2: Schematic on the use of an AUV for estimation of anisotropy using sampled bistatic acoustic scattered field data. A fixed source insonifies a patch on the bottom using a 1-5kHz signal, an AUV sampled the resulting scattered field and uses the collected amplitude data to estimate the anisotropy angle of ripple field.

vectors. In the case of regression for cylinder angle estimation, the simulation model was then successfully used to estimate the two orientations of the steel pipe in the Massachusetts Bay experiment.

This chapter first describes the machine learning regression methodology for estimation of cylinder and sand ripple anisotropy angles. It then describes the data and results for regression in the cylinder orientation problem and the sand ripple anisotropy problem.

6.1 Machine Learning Regression Methodology

The variables used in this paper to describe the regression process are seen in Table 6.1.

A supervised machine learning technique called support vector machine (SVM) regression was selected to perform the angle estimations. Like for the classification case, SVMs were selected because, while training takes time and computational power, regression using an existing model is fast and computationally efficient[35]. This means that regression can be run in real-time on an AUV computer.

For training and testing SVM regression models, the simulated full bistatic data sets generated for the range of orientation or anisotropy angles were broken into randomly selected example vectors. An example vector represents the scattering amplitude data to the machine learning algorithm. For this application, each example vector represented the scattering field amplitudes an AUV collected in several passes around the insonified target or roughness patch. Independent training, validation, and test sets of these example vectors were generated. The training set was then used to train a regression model. The validation and test sets were used to test the ability of the regression model to correctly estimate cylinder orientation angle or bottom anisotropy angle.

6.1.1 Feature Space Description

In this machine learning approach, a model is trained using real or simulated scattered field data that have been converted into example vectors in a feature space representation. The feature space representation for this problem was selected based on the observation that the strongest distinction between the scattering fields of cylinders or ripple fields with different aspect angles is in the angular location of the amplitude maxima. As it circles the insonified bottom patch or target, the AUV samples each angular feature used to describe

the scattered field. Amplitudes are mapped to features using the same bistatic angle based method described for classification in Section 5.1.2. Each example vector consisted of a sequence of feature-value pairs, where each value is the median scattering amplitude sampled within the angular region defined by the feature number. This feature number, F_n, was calculated as a function of the location of a sample's angle relative to the source-target line, (θ_s), and a step size in azimuth, $\Delta\theta$ using Eq. 5.5. The sequence of features-value pairs and the associated label are combined into an example vector, represented by $(\mathbf{x_i}, y_i)$, where $\mathbf{x_i}$ is the set of feature-value pairs constructed using equation 5.5 and y_i is the true target orientation or anisotropy angle for the example, if it is known.

$$\begin{aligned} \mathbf{x_i} &= \{[F_1, A_1], ..., [F_N, A_N]\} \\ y_i &= \gamma \end{aligned} \quad . \tag{6.1}$$

The label, y_i, is the anisotropy angle or cylinder angle for the example vector, $y_i = \gamma$. The geometry of this feature space is seen in Figure B-1.

Each example vector $(\mathbf{x_i}, y_i)$ represents the data collected by a vehicle follows some path approximately circling the insonified bottom patch. The full set of example vectors, $\{\mathbf{x_i}, \mathbf{y_i}\}$, was used to construct independent training, validation and test data sets, $\mathbf{X_t}, \mathbf{X_v}, \mathbf{X_x}$.

$$\mathbf{X} = (\mathbf{x_1}, y_1), ..., (\mathbf{x_l}, y_l) \subset \chi x \mathbb{R}. \tag{6.2}$$

Where χ represents the space of the input, such that $\chi = \mathbb{R}^{n_F}$ if there are n_F features. These data sets are used to train and then test the SVM regression models.

SVM Regression

SVM regression works by maximizing the minimum distance from the normal regression function $\mathbf{w}$ to the set of training vectors. The soft-margin SVM regression formulation is used [32]:

$$\underset{\mathbf{w},\xi_i^*,\xi_i,b}{\operatorname{argmax}} \frac{1}{2}\|\mathbf{w}\|^2 + C\sum_{i=1}^{l} \xi_i + \xi_i^*$$

Subject to conditions:

$$\begin{cases} y_i - < \mathbf{w}, \mathbf{x_i} > -b \leq \epsilon + \xi_i \\ < \mathbf{w}, \mathbf{x_i} > +b - y_i \leq \epsilon + \xi_i \\ \xi_i \xi_i * \geq 0 \end{cases} \tag{6.3}$$

where $\mathbf{w}$ is the normal SVM regression function, ϵ represents the precision of the system, ξ_i and ξ_i* are slack variables that allow the optimization to deviate from ϵ in the selection of a solution, C is used to adjust the trade-off between the size of $\|\mathbf{w}\|$ and the tolerance for errors greater than ϵ, and b is the offset from the origin of the regression solution. $\mathbf{x_i}$ is the i^{th} example vector and y_i its label.

New data is then classified by taking the dot product of a new example vector, $\mathbf{x_n}$, with the normal SVM regression function $\mathbf{w}$ in χ space and adding the offset b. The output is $\tilde{\gamma}(\mathbf{x_n})$, the anisotropy angle estimate.

$$\tilde{\gamma}(\mathbf{x_n}) = < \mathbf{w}, \mathbf{x_n} > +b, \mathbf{w} \in \chi, b \in \mathbb{R}. \tag{6.4}$$

where $< \mathbf{w}, \mathbf{x} >$ represents the dot product in χ.

The SVM-Light[33] software package was used to perform the optimization.

6.1.2 Angle Estimation Method

Estimating the angle between source and aspect-dependent target or bottom ridging involves two components: a training/analysis process, which was conducted off-line to construct a model, and a real-time signal processing and regression process, which was run on a simulated vehicle.

Training and Analysis

Figure 6-3 shows a block diagram of the training/analysis process. Each example vector represents data collected by an AUV approximately circling the insonified bottom patch or target. These SVM examples were generated for this simulation study by randomly selecting

n_S, $n_S - 1$ or $n_S + 1$ points within each angular feature for all n_F features, approximating the data collected by an AUV circling the target region collecting $N = n_S n_F$ samples. The median of the samples within each angular feature is calculated to construct the example vector, so additional data from a larger value of N introduces additional averaging into the value estimates for each feature. In an experiment, the source would fire on a 1Hz schedule and the vehicle would record an acoustic data file from the array each second, calculating the scattering amplitude for the bottom patch using onboard processing. This means that the number of amplitude samples can be equated to the number of seconds of data collection.

The full set of example vectors was split into three independent data sets, such that 50% of examples were used for training set $\mathbf{X_t}$, 25% for validation $\mathbf{X_v}$ and 25% for testing $\mathbf{X_x}$ as suggested by Hastie et. al. in The Elements of Statistical Learning [34]. The training set of these example vectors was used to train an SVM model. The validation set was used to select feature space and SVM training parameters. Once feature and model parameters were set, the test data set was then used to estimate the model's prediction error on new data. The test data set was necessary because the results from regression of the validation set were used to select SVM model parameters.

In addition to the actual angle estimate, we are interested in how good that estimate is. In particular, we need to know the error bars for different confidence values: in the final system, the AUV will continue to collect data until, for example, the estimate has less than 10 degrees of error with 95% confidence. For this reason, an additional test set $\mathbf{X_c}$ (independent of $\mathbf{X_t}$ and $\mathbf{X_v}$) was created that included examples with different numbers of samples (i.e. values of N). $\mathbf{X_c}$ was used to create an confidence model to estimate the quality of a regression value in real time based on the amount of data collected by the AUV. The quantity being estimated by the confidence model is $P(D < m|N, \tilde{\gamma})$, where $m = |\gamma - \tilde{\gamma}|$ is the magnitude of the error in the estimate in degrees, D is the random variable associated with the error $d = \gamma - \tilde{\gamma}$, N is the number of amplitude datum used to construct the example vector, and $\tilde{\gamma}$ is the estimate for angle. The regression error was found to be Gaussian in nature, so the probability density function (PDF) of error for a given number of samples N was represented by a normal distribution of some mean and standard deviation, $D \sim f_D(d) = \mathcal{N}(\mu, \sigma^2)$.

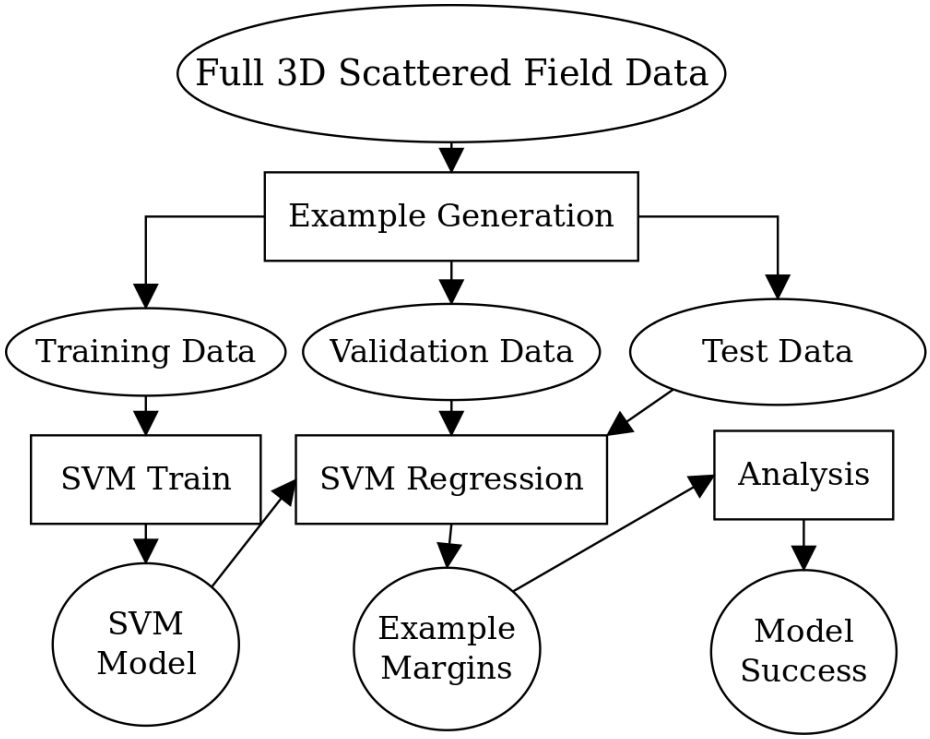

Figure 6-3: Training and Analysis Process. Real or simulated 3D scattered field data is used to generate sets of example vectors for training, validation and testing. The model trained with the training set is used along with the validation set to select SVM model parameters. The test set is used to asses model viability.

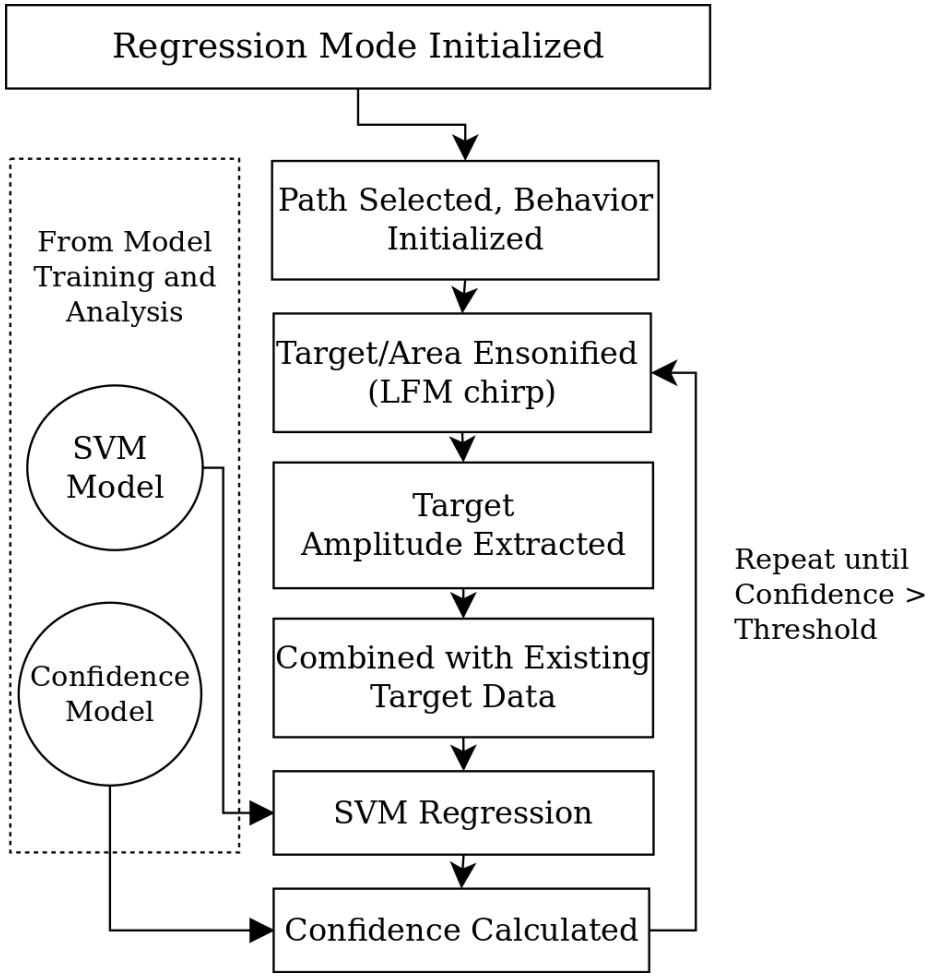

Figure 6-4: Real-time regression process. Once the regression mode is initialized on a vehicle, the SVM model produced in the training/analysis phase is used to estimate the angle and the confidence of that estimate.

6.1.3 Real-Time Regression

The regression model generated in the training and analysis phase is used by a vehicle to perform real-time angle estimation(Figure 6-4). This was carried out on simulated vehicles in the LAMSS MOOS-IvP simulation environment. In this real time regression process, the vehicle approximately circled a aspect-dependent target or insonified bottom patch until the confidence reached an error of less than 10 degrees with 95% confidence. This took around 10 minutes for cylinder estimation and 15 minutes for ripple anisotropy estimation in simulation, with one sample collected each second by the virtual vehicle, corresponding to a value of $N = 600$ or $N = 900$. New scattering amplitudes were combined with existing data into an example vector, which the regression model used to estimate the angle.

The high fidelity LAMSS MOOS-IvP[27] simulation environment, which includes physics-based vehicle dynamics, environmental parameters and acoustic simulation, was used to demonstrate real-time regression on the simulated vehicle. The high-fidelity acoustic simulation includes interfaces to BELLHOP[36] and OASES-SCATT[8]. For the simulation studies used for cylinder angle estimation, a simulated version of the LAMSS vehicle *Unicorn* with a 16 element nose array at 0.05m spacing was deployed at the site of the Massachusetts Bay experiment in Broad Sound. For the simulation studies used for bottom anisotropy estimation, a simulated version of the LAMSS vehicle *Unicorn* with a 16 element nose array at 0.05m spacing was deployed in a virtual ocean in 100m water depth off of the coast of Massachusetts. An acoustic simulator, uSimActiveSonar_shallow, was developed to simulate acoustic arrivals, including all multipath, on a simulated AUV array. uSimActiveSonar_shallow used models produced by BELLHOP to produce a time series across the simulated array. The time series included arrivals due to the direct blast from the source, source-target-vehicle arrivals and multipath with up to 3 bounces. Another process, pActiveTargetProcess, took in that time series and output an estimated amplitude for the insonified patch of bottom. Once the signal processing chain completed, uSimScatt published the scattered amplitude for the current location and geometry of the vehicle, source, and target or bottom patch based on the simulation model. An SVM model was specified to the SVM interface application, pSVMRegress, which ran real time regression on amplitude data as it was collected by the simulated AUV, constantly updating estimated anisotropy angle until all critical waypoints were sampled. Figure 6-5 shows the regression processing

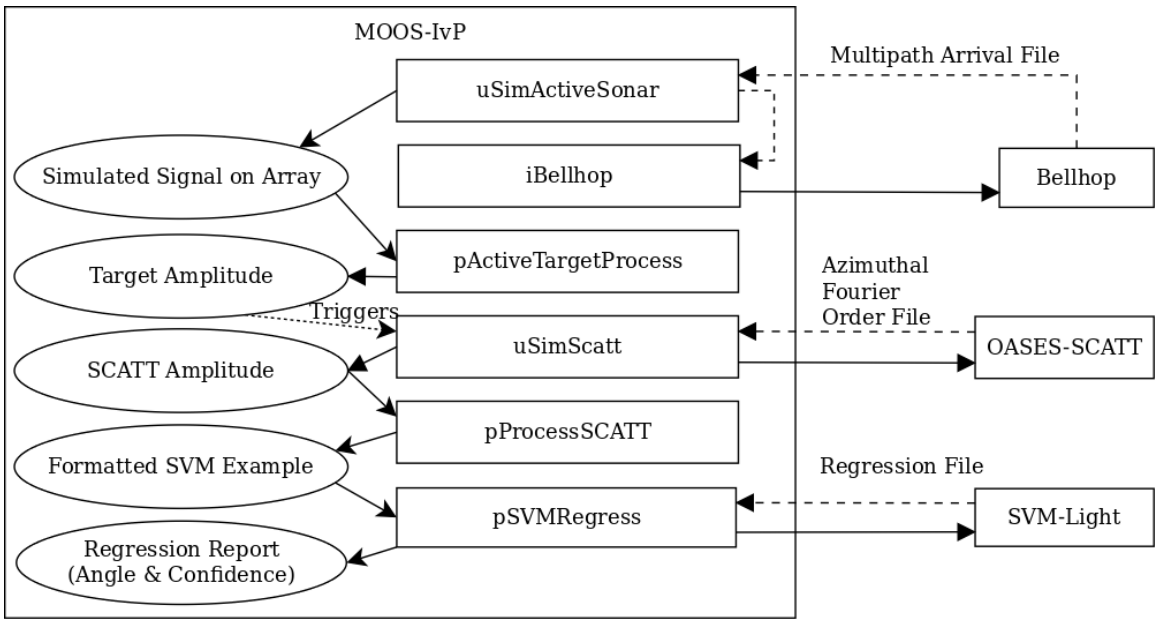

Figure 6-5: Real-time regression processing chain in MOOS-IvP simulation environment. Multipath arrivals are simulated on array by uSimActiveSonar. That data is processed in real time using pActiveTargetProcess to extract target amplitudes. When the selected target's contact is present, uSimScatt outputs the appropriate scattered field amplitude for pProcessScatt. pSVMRegress estimates the angle from the resulting example vector as new data is acquired. It also estimates the probability that that estimate has an error less than d degrees, where d is configurable.

chain used to demonstrate anisotropy estimation in real time on the simulated vehicle.

6.2 Cylinder Angle Estimation

6.2.1 Background

Zampolli et. al. describe some of the aspect-dependent monostatic scattering features from targets including pipes and cylinders [37]. Similarly, Williams et. al. explored the monostatic effects of cylinders in contact with sand sediment with aspects of 0 to 90 degrees [38]. These papers do not use this information for classification, and only look at the monostatic return, but do observe the changes in scattering strength depending on the angle between the source and the target axis. Ji et. al. looked at some of the multi-static scattering effects from aspect dependence in a tank experiment and in simulation [39]. Schmidt and Lee also discussed some of the bistatic scattering characteristics of aspect-dependent targets [7]. These sources all indicate that the effects of target orientation on the

scattering pattern are significant, which suggests that they might be used to estimate the target aspect directly.

6.2.2 Simulated Scattered Field Data

To estimate the angles of the steel pipe target in the Massachusetts Bay experiment, a regression model was trained using scattering simulations for a water-filled cylinder matching the dimensions of the cylinder in the experiment, 5 feet long by 1.5 feet diameter, in a 15m deep waveguide with a soundspeed of 1500 m/s and a fluid sand bottom. The source was approximated as 8kHz with a range of 100m to the target and a depth of 3m. The configuration for the simulated targets are shown in Table 6.2. Cylinders at rotations in 5 degree increments were used, such that $\gamma = [0, 5, ..., 175]$. Values of $\Delta\theta = 5^o$ and $n_S = 10$ were used to generate the example vectors used to train the SVM regression model, giving a total number of samples per example vectors of $N = 720$.

The scattering simulation models were only approximate matches to the conditions and target in this experiment, as discussed in Section 4.4.2. In a real scenario, the information available for model selection would be similar to what we had in the Massachusetts Bay Experiment: approximate water depth, mean soundspeed, approximate target and source locations. The target would also be unknown, and very few targets are perfect solid cylinders. The importance of the simulation modelling was not to provide a direct comparison to the real data, but to determine whether a somewhat generic, simplistic simulation of an aspect-dependent target could be used to estimate unknown characteristics of an actual target.

6.2.3 Results

The scattering data collected during the experiment was converted into example vectors of N length using the method described for classification in Section 5.1.2. The value of N was varied to assess the impact of the quantity of data collected on the quality of the angle estimate. Figure 6-6 shows the probability density function with respect to estimated angle empirically derived for different values of N for both aspects. With a value of $N = 1500$, or 25 minutes of data collection, the estimates for both target orientations converged to a solution: $\tilde{\gamma} = 110^o$ for the first target aspect and $\tilde{\gamma} = 35^o$ for the second. These results matched the location of glints and minima in the radiation patterns of the real data. The

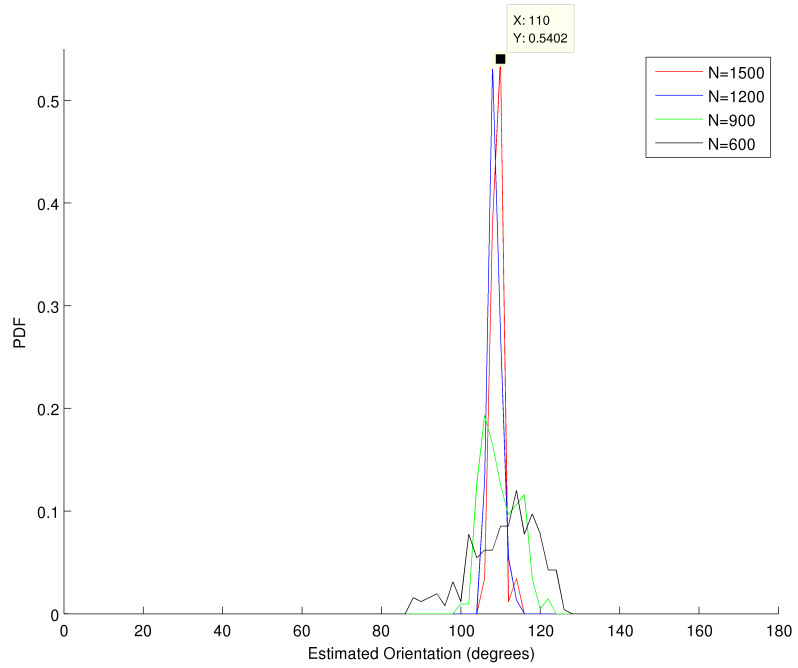

(a) Orientation 1.

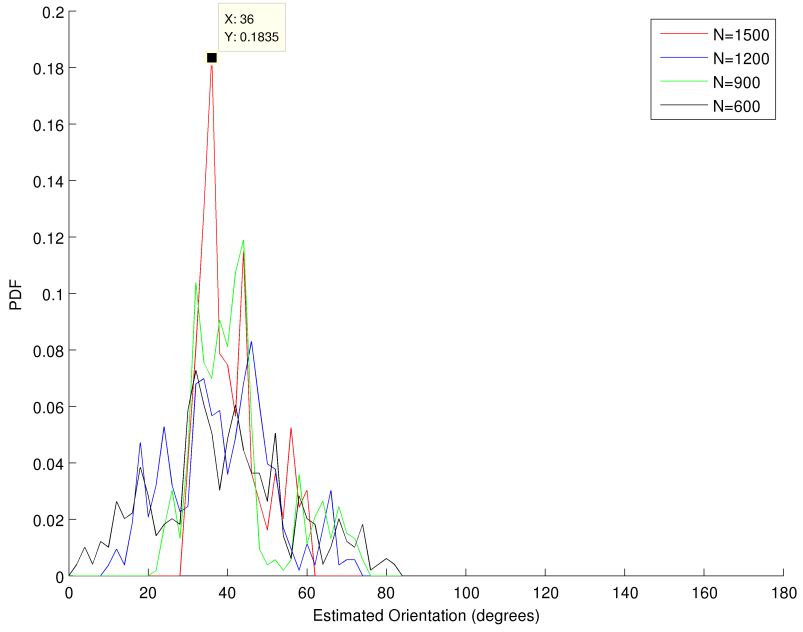

(b) Orientation 2.

Figure 6-6: Probability density function over estimated angle for varying values of N for the two target orientations. The first orientation converges to a value of $\tilde{\gamma} = 110^o$, the second to a value of $\tilde{\gamma} = 35^o$.

estimates were also 74 degrees apart, which was consistent with the expected 78 degree change in ship position between the two data sets for a target at (170,155).

6.3 Seabed Ripple Anisotropy Angle Estimation

Figure 6-7 shows the effect of bottom ridging directionality on the location of minima and maxima in the bistatic scattered field. These changes to the scattered field due to anisotropy direction can have a significant impact on target scattering [7]. The goal of this research is to produce a set of algorithms and processes to estimate the anisotropy of ripple fields using AUVs. This information could be used to enhance performance of bistatic target detection, localization and classification.

The basic configuration for this method is illustrated in Figure 6-2. A source, fixed relative to the bottom patch, insonifies a region on the bottom and an AUV samples the scattering data around that insonified patch. A model is trained using a set of example vectors mapping scattering amplitudes from a comprehensive data set to sampling location along an AUV path. This model is then used in real time by a vehicle to estimate of anisotropy angle, γ, based on scattering amplitude data.

6.3.1 Background

There are a number of papers that discuss methods for the estimation of various seabed parameters from scattered field data, including several that utilize machine learning techniques.

Schmidt and Lee [7] explored the effect of anisotropic rough bottom scattering from different directions on 3D bistatic scattering from seabed targets, and described the development of an anisotropic ripple field scattering simulation module, used here to explore the possibility of estimating bottom roughness using bistatic data.

Kevin Williams[40] constructed a model for forward scattering and collected bistatic data on a mobile receiving array and compared models to data in the forward scattering direction, but did not attempt to estimate bottom parameters using that bistatic data. Bishwajit et. al. [41] and Huang et. al. [42] discuss the use of multibeam backscatter data to determine seabed types and parameters using techniques that include Neural Networks. Dosso et. al.[43] and Steininger et. al. [44] used inversion techniques to estimate seabed roughness

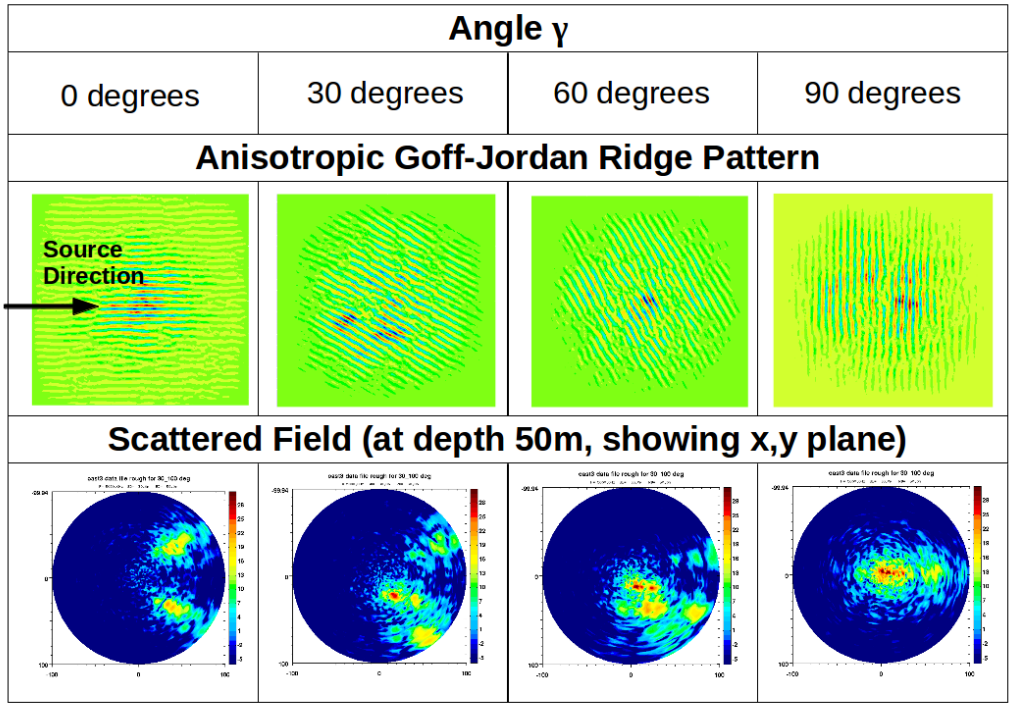

Figure 6-7: Example Anisotropic Goff-Jordan rough bottom ripple fields and resulting scattered fields.

from acoustic scattering and propagation. De et. al. [45] looked at using echo-sounder backscatter data to estimate sea floor roughness, and Manik [46] used backscatter from the sea bottom to estimate bottom properties.

These techniques focus on estimating parameters such as spectral scattering coefficients or bottom composition, and do not provide direct information on the rough interface geometry. Becker [47] examines a method for estimating the surface height power distribution of bottom roughness using backscattering strength. Several techniques also exist for eliminating the rough interface scattering noise from sidescan sonar data[48].

Unlike the method presented here, these methods utilize backscatter strength or propagation information rather than directional 3D features that show up in the bistatic scattering field. Attributes of the full three dimensional bistatic scattered field can be exploited in the estimation of bottom characteristics by insonifying a region of ocean bottom using an acoustic source and collecting acoustic data using an AUV fitted with a hydrophone array.

6.3.2 Simulated Scattered Field Data

Because real 3D bistatic scattered field data for different angles of bottom anisotropy was unavailable, simulated data was used to develop and test the anisotropy regression methods discussed in this paper. Scattered fields were modelled using the scattering simulation package with Goff-Jordan anisotropic power spectra[8].

Figure 6-8 shows the environmental and source parameters used in generating scattered field data. The source is located at 30m depth and 100m from the patch being insonified on the bottom. The environment is modelled as a waveguide, with an air layer, a 100m deep water layer, and a fluid sand bottom.

Table 6.3 shows the parameters used in the creation of the simulated scattered field data. These parameters were selected based on those chosen by Lee in his thesis [9]. The insonified area is modelled as a 20m by 20m rough patch. A Goff-Jordan Power Spectrum is used, with a root mean squared (RMS) roughness height of 0.1m, a major correlation length of 2m and a minor correlation length of 0.01m. Scattered fields are simulated for anisotropy directions between 0 and 90 degrees at 15 degree increments. A few of the simulated rough bottom patches and their resulting scattered fields can be seen in Figure 6-7.

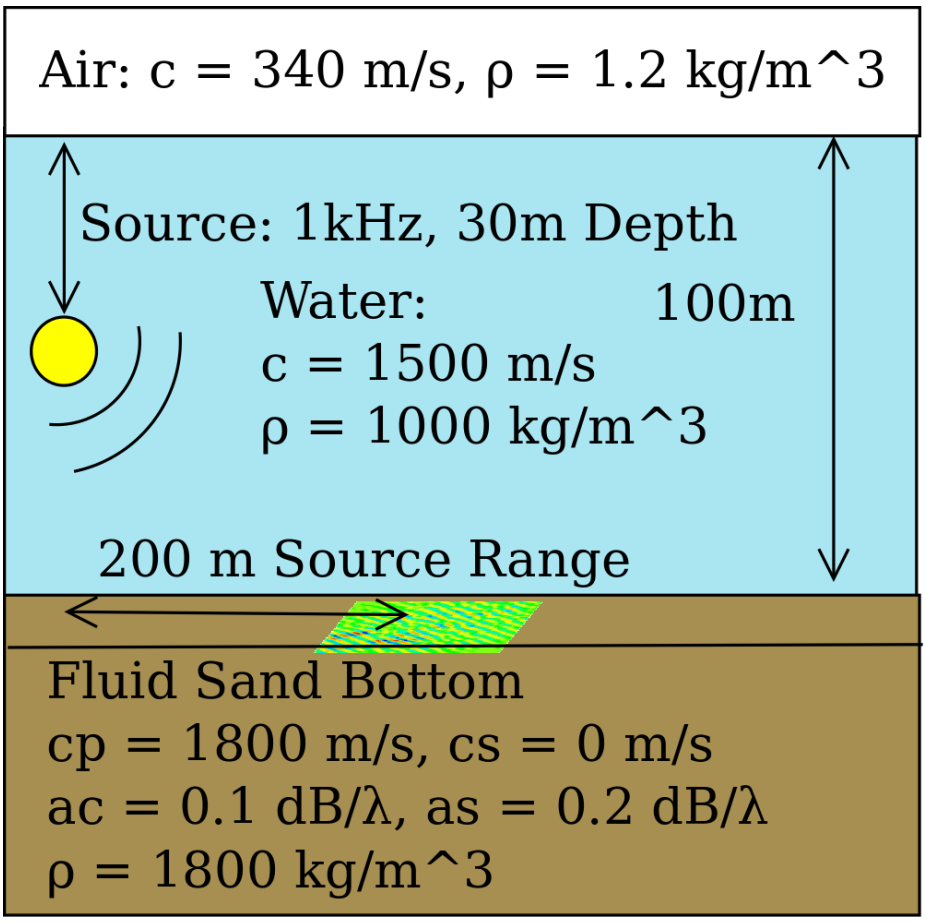

Figure 6-8: Environmental and source parameters used in rough patch scattering simulation.

6.3.3 Results

Scattered field data was simulated using the parameters in Table 6.3. The outputs of the scattering simulator are data files that contain the azimuthal Fourier orders for the scattered fields. For each field the amplitudes on a fine grid were calculated, and that amplitude data then sampled into training, validation, and test examples. 4000 example paths were used for training, 2000 for validation and 2000 for testing. Since there are seven scattered fields sampled by each path, the training set $\mathbf{X_t}$ consists of 32000 examples, the validation and test sets $\mathbf{X_v}$ and $\mathbf{X_x}$ each consist of 14000 example vectors. The training, validation and test sets were all constructed using the number of samples $N = 720$. The additional test set used for confidence estimation with varying values of N, $\mathbf{X_c}$, consisted of 12000 paths (84000 examples). These are large numbers of example vectors, but they are randomly selected from the possible AUV sampling from a grid of amplitude values. A similar grid could be constructed from real AUV-sampled data.

Feature Space Selection

The same model parameters were used to assess all values of $\Delta\theta$, and the total number of points sampled by the AUV was kept constant. For each tested value of $\Delta\theta$, a normal distribution was fit using least squares to the PDF of the estimation error d. The standard deviations of these normal distributions were compared to select the best feature space: a lower standard deviation indicates higher accuracy in angle estimation. The final value selected from a search over $\Delta\theta$ was $\Delta\theta = 5^o$, resulting $n_F = 72$ as the number of features.

SVM Model Parameter Selection

The SVM kernel used for the final model was linear, and the value for C was selected using a logarithmic search over results from the validation set. The final value was $C = 0.001$. The magnitude of the normal vector ($\|w\|$) for the trained model was 2.43, indicating the low model complexity expected from a linear model.

Regression Results from Test Set

The test set was used to asses the validity of the model selected using the validation set. Within the test set, each example vector represents an AUV path through the field, with

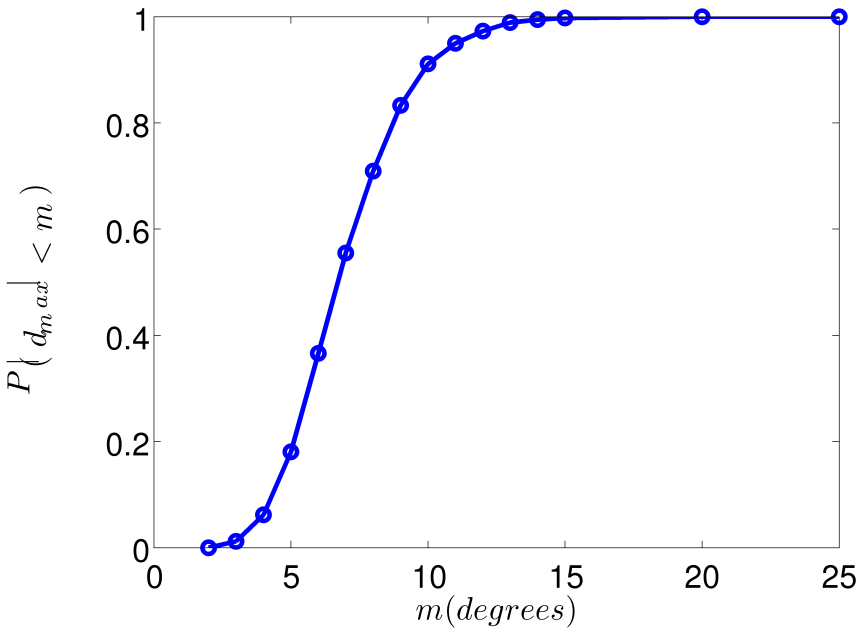

Figure 6-9: $P(|d_{max}| < m)$, calculated by finding the percentage of paths that resulted in less than m degrees error from regression of the test set $\mathbf{X}_x$. The curve shows the characteristics of a Gaussian CDF.

data collected at identical locations across all seven scattered fields. Figure 6-10 shows a plot of the probability that a paths will have less than m degrees maximum error, $P(|d_{max}| < m)$, where m is an error magnitude in degrees and d_{max} is the maximum regression estimation error based on data collected on along the same path through the scattering fields from the seven anisotropy angles. These probabilities were calculated by finding the percentage of paths in the test set $\mathbf{X}_x$ that has a regression estimation error of less than m degrees. These results show that the model was highly successful in estimating anisotropy angle in this data set, with 100% of paths resulting in a maximum estimation error d_{max} of less than 20^o, 91% showing a maximum error of less than 10^o and 18% with a maximum error of less than 5^o. The test examples have a number of samples $N = 720$, so this indicates that with 12 minutes of data collection around the insonified bottom patch, it is possible to get less than 10^o error with greater than 90% confidence. The plot also looks like the cumulative distribution function (CDF) for a Gaussian distribution. Figure 6-10 shows the true anisotropy angle versus estimated anisotropy angle for $|d_{max}| < 3^o$. Each line represents a single AUV path through the field, with data collected at identical locations across all seven scattered fields.

The confidence estimation set $\mathbf{X}_c$ included examples with differing values of N so that

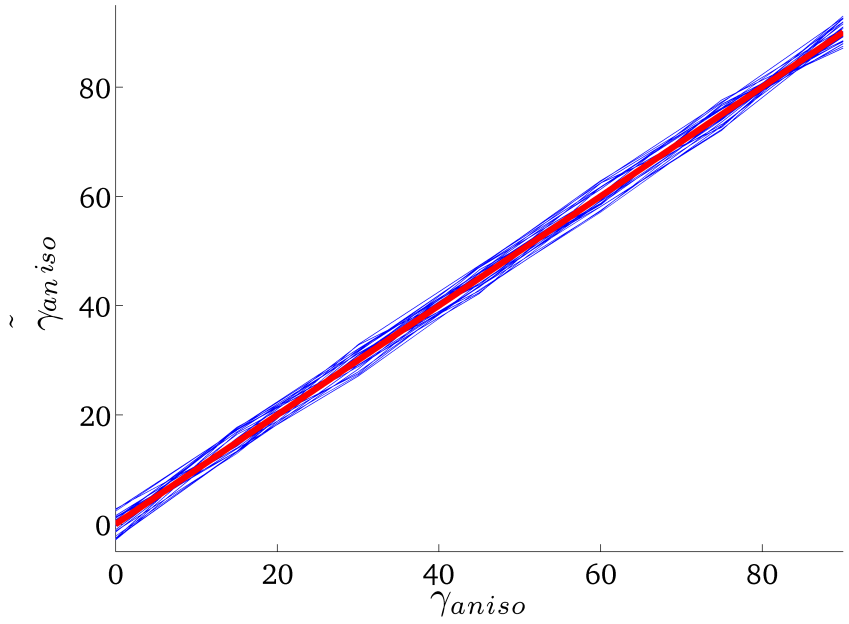

Figure 6-10: True anisotropy angle γ versus estimated anisotropy angle $\tilde{\gamma}$ for paths in test set $\mathbf{X}_x$ that resulted in maximum anisotropy error of less than 3^o. Each blue line represents the anisotropy estimation values for a single geometric sampling applied across the tested anisotropy angles. The red line represents a perfect regression result, where $\gamma = \tilde{\gamma}$.

the effect of number of samples on model accuracy could be assessed. Figure 6-11 shows the relationship between the PDF of the anisotropy error, $f_D(d)$, and the number of samples, N. These plots show approximately Gaussian distributions with standard deviations that decrease as N increases. Normal distributions were fit to these curves using least squares. Figure 6-12 shows the nearly linear relationship between $\log(\sigma)$ and $\log(N)$ and the least-squares linear regression fit of $\log(\sigma) = -0.44\log(N)+4.64$. μ was found to be approximately constant relative to theta. A model $\mathcal{N}(\sigma(N), \mu = -0.5)$ where $\log(\sigma(N)) = -0.44\log(N) + 4.64$ was compared to the error distribution for each value of N using pair-wise two-sample t-tests. In this test, the null hypothesis was that the model and the actual error distribution were drawn from the same normal distribution. All resulting p-values were greater than 0.99, indicating the likelihood that the error data were drawn from the same distribution as the model data was in excess of 99%.

Pair-wise two-sample t-tests were also used to look at the relationship between the PDF for each anisotropy angle and the model $\mathcal{N}(\sigma(N = 720), \mu = -0.5)$. The resulting p-values ranged between 0.994 and 0.998, indicating that the error distributions for the seven

anisotropy angles were drawn from the same normal distribution as the model with high probability and suggesting that $D(N, \gamma) \simeq D(N)$.

The functional relationship between N and σ was used along with a lookup table for the CDF of a standard normal distribution for calculating the confidence of an anisotropy estimate as a part of the regression processing chain.

$$F_Y(y) = P(Y \leq y) = 1/\sqrt{(2\pi)} \int_{-\inf}^{y} e^{-t^2/2} dt \tag{6.5}$$

Where $F_Y(y)$ is the CDF for a standardized angle error y and Y is the random variable associated with y. To get the probability that an anisotropy estimate $\tilde{\gamma}$ has an error less than m given the vehicle has collected N samples, the standardized value of the error m is first calculated based on estimates for $\mu(N)$ and $\sigma(N)$.

$$y = (m - \mu(N))/\sigma(N) \tag{6.6}$$

Next, a standard normal distribution lookup table is used to find the probability that the error is less than that value.

$$P(|D| < m|N) = P(Y \leq y, Y \geq -y) = 2P(Y \leq y) - 1 = 2F_Y(y) - 1 \tag{6.7}$$

This allows the AUV to quickly access confidence of a given measurement while storing a single lookup table of CDF values and the dependence of μ and σ on N. The linear relationship between between $\log(\sigma)$ and $\log(N)$ makes predicting error and confidence in angle estimate for new values of N.

Testing in MOOS-IvP Simulation Environment

The real-time regression processing was tested in the MOOS-IvP simulation environment (Figure 6-13). The SVM model, feature space, and confidence model files were specified in the configuration of pSVMRegress. A simulated vehicle was then launched, and commanded in a regression mission around a simulated rough patch 100m from the source. The full processing chain ran in real time, coming up with progressive estimates of the anisotropy angle as the vehicle circled the target, until the regression confidence reached 95%. This was repeated with different simulated source locations and different anisotropy angles. Running

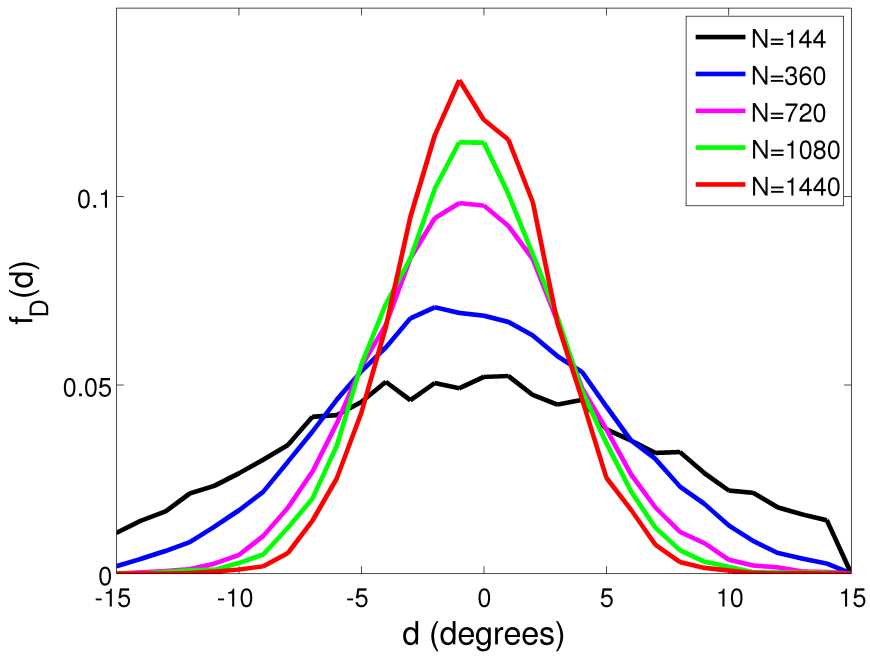

Figure 6-11: PDFs of anisotropy error, $f_D(d)$, versus anisotropy error in degrees, d, for several values of N from analysis of error data. Note that the error is clearly Gaussian in distribution and as the time spent sampling the scattered field increases, the standard deviation decreases while the mean remains approximately the same. Gaussian models were fit to this data to estimate mean and standard deviation for different numbers of samples and used to estimate confidence.

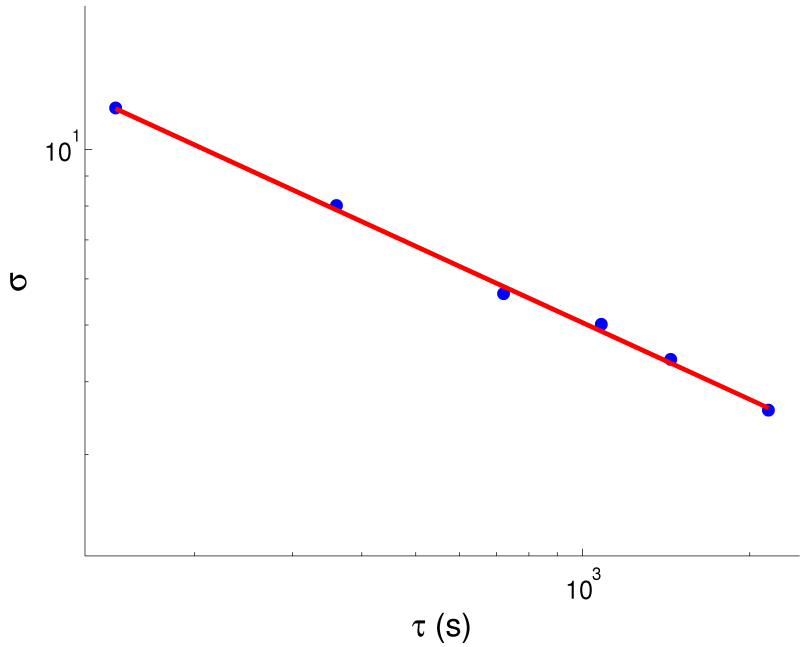

Figure 6-12: The log-log linear relationship between the number of samples N and the standard deviation of the PDF of the error, σ. The circles show the values derived from the data, and the line shows the least squares best fit of $\log(\sigma) = -0.44\log(N) + 4.64$.

the processing chain in these simulations demonstrated the plausibility of real-time ripple field anisotropy estimation with onboard processing on an AUV.

6.4 Conclusions

6.4.1 Cylinder Angle Estimation

The Massachusetts Bay Experiment was an excellent test of the target characterization technique proposed in this thesis. The source location was uncertain as it was located on a ship swinging at anchor, with a software trigger that caused a 5ms jitter in firing time relative to the CSAC PPS reference. The acoustic source was also omnidirectional, only 147dB, and far further from the targets (100m instead of 60m). The actual target location and orientation were not known during the experiment as the steel pipe was dropped off the back of the ship and the position approximately estimated via GPS (the original estimates were 15-20m off of the final estimates). Only half the sonar aperture was available as the second 24DSI12-PLL board malfunctions, so that only the first 8 channels were available for processing. Despite the challenges, the acoustic data collected during this test was,

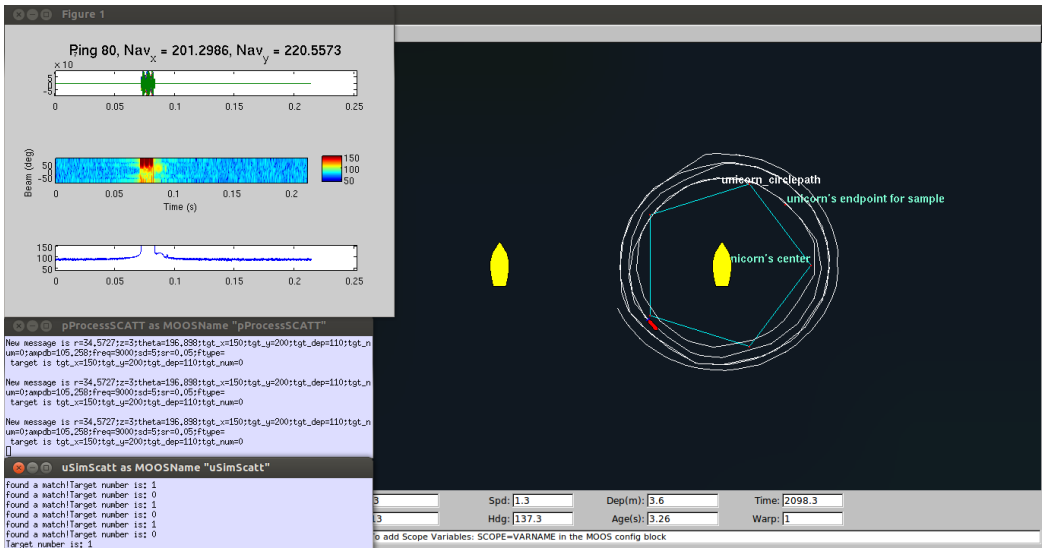

Figure 6-13: Simulated AUV circling a simulated insonifies bottom patch, with SVM Regression for estimation of anisotropy angle.

if anything, better than that collected during the BayEx'14 experiment. This could have occurred because of the slightly deeper water, the sand bottom, or the lack of clutter.

Training a SVM regression model on simulated scattered fields of cylinders of different orientations then estimating the orientation of the real pipe in the experiment was very successful. After 1400s of data collection, both orientations converged to a solution that was consistent with the change in ship position between aspects and with observed features in the scattering radiation pattern. This excellent performance was despite the fact that the simulation model was not a very good match for the experiment conditions and the fact that the scattering patterns for the 110 degree aspect do not look visually similar between real and simulated cases. The model is clearly able to pick out the important features in common, ignoring the details in scattering pattern that makes matching difficult, in this case, for a human observer. The success in estimation despite the differences between the model and real target geometry suggests that a similar method might be tried to estimate the orientation of a variety of aspect-dependent targets, including those with more complex geometries.

6.4.2 Ripple Angle Estimation

The generation of SVM regression models and use of those models in estimating the angle of bottom ridging in a real-time simulation environment was successfully demonstrated.

This work shows the potential of using the bistatic scattered acoustic field from bottom ripples to estimate anisotropy angle. There are several avenues of further work that should be pursued, given the success of this initial work. The results shown here are based on simulated scattered field data, but to confirm the viability of this methodology it should be tested using real acoustic data, either small scale or from full scale experiments. Because the software used in performing model training, analysis and real-time regression is agnostic on whether the data comes from a model, data collected by an AUV or another source, this could be done with any full bistatic data set over the range of desired anisotropy angles. It would also be valuable to explore in simulation whether the same regression and confidence models could be successfully used with changes in environment, such as sound speed, depth, and bottom composition. Overall, the simulation results show that this method has promise and warrants further investigation.

Table 6.1: Variables used to describe regression for angle estimation.

b	Offset from origin of regression solution
C	SVM trade-off variable
F_n	Feature number.
n_F	Number of features.
n_S	Number of samples per feature.
r_s	Range to target of an acoustic sample.
$\Delta\theta$	Step size in angle used to define feature space.
w	Normal SVM regression function
x_i	Example vector for SVM
y_i	Label for the example vector x_i (for cylinder angle estimation $\gamma_{cyl,i}$,for bottom angle anisotropy estimation $\gamma_{aniso,i}$)
z_s	Depth of an acoustic sample.
z_{max}	Maximum depth.
d	Angle estimation error in degrees.
d_{max}	Maximum angle estimation error for a single path, tested across all anisotropy angles.
D	Random variable that describes the distribution of the angle estimation error.
γ	Angle of anisotropy regression or cylinder rotation regression
$\tilde{\gamma}$	Estimated anisotropy angle or cylinder rotation angle
ϵ	SVM regression error tolerance
m	Magnitude of angle estimation error in degrees, $\|d\|$.
ξ_i, ξ_i*	Slack variables
θ_s	Azimuth, relative to source-target line, of an acoustic sample.
N	Number of acoustic samples taken around cylinder target or insonified rough patch.

Table 6.2: Parameters for target scattering simulations for cylinder regression.

Parameter	Description	Value
r	Cylinder radius	0.2286m
h	Cylinder height	1.5m
Roll	Roll of cylinder	90 degrees
ρ	Density of fluid inside cylinder	1000
c_p	Compressional soundspeed of fluid inside cylinder	1500
a_p	Attenuation of fluid	0.02 dB/λ
Pitch	Pitch of cylinder	[0,5,10,...,175]

Table 6.3: Parameters for simulating anisotropic ripple fields.

Parameter	Description	Value
nx	Number of grids in x direction	512
ny	Number of grids in y direction	512
sx	Length of patch in x direction (m)	20
sy	Length of patch in y direction (m)	20
c1	Major correlation length (m)	2
c2	Minor correlation length (m)	0.01
sk	Angle of anisotropy in degrees	[0,15,30,45,60,75,90]
rm	RMS roughness height (m)	0.1
window	Window type	Hanning

Chapter 7

Future Work and Concluding Remarks

7.1 Future Work

The success of AUV sampling of amplitude-based bistatic radiation patterns for characterization of simple target geometries shows the potential of this approach and opens the door for further research. Simulation studies using the MOOS-IvP simulation environment and scattering simulation interface were used to test real-time processing and classification, but the real test would be running the full processing chain on an AUV collecting data around real targets. An additional scattering experiment, allowing a full closed-loop demonstration of target localization and classification using a simulation-based SVM classification model for the environment and expected targets, would be an important addition to this work. Moving forward, it would also be extremely interesting to collect bistatic data from more complex targets and attempt classification for less regular shapes, buried targets, and clutter.

Another avenue for future work would be to look at a similar technique with a slightly different problem formulation. One of the limitations of this methodology is the aspect-dependence problem: the orientation of the target relative to the acoustic source significantly changes the scattering pattern. This makes regression for estimation of target orientation a possible and necessary part of the target characterization process. Estimating the target orientation takes 5-10 times longer than a simple shape classification. To eliminate this issue, the problem formulation could be extended from bistatic to multistatic, to a scenario

in which one AUV is used to insonify a target area while another collects bistatic data. This would be a more mobile approach and would solve the orientation-dependence problem encountered for aspect-dependent targets that requires separate classification and regression steps. The Massachusetts Bay experiment showed that a lower powered source with >10m location uncertainty did not invalidate the bistatic results, which suggests that the navigation uncertainty of a AUV-based source would not invalidate this method.

7.2 Concluding Remarks

In the air and on the ground, robotic systems maintain constant high-bandwidth communication to an operator, who assists with classification and prosecution tasks similar to those being attempted with AUVs today. The limitations of underwater communications mean that, for effective underwater missions, more of the critical decision making must be conducted onboard without the benefit of human guidance. However, many of the sensing technologies and most of the classification techniques currently being used in Mine Countermeasures follow the traditional paradigm, requiring human interaction and transfer of large amounts of data at every part of the mission from localization to classification to prosecution. The final approach presented in this thesis meets both requirements for real-time AUV-based target characterization outlined in the introduction to this thesis: an inexpensive sensing payload and a classification method that can be run in real-time on an AUV computer. While further work will be required to show applicability to different target types and environments, the feasibility of using bistatic angle dependence of target scattering amplitude for characterization of sphere and cylindrical target geometries was successfully demonstrated.

This thesis developed a sensing technique and classification methodology for seabed targets that can be run entirely on an AUV, without requiring vehicle recovery and redeployment, postprocessing of data, or human interpretation of images. While it has long been known that the radiation pattern from a target is distinctive, this work demonstrated how to collect that data in the real world using an inexpensive hydrophone nose array and process it for the classification and parameter estimation of targets. Chapter 3 described the payload design required for precision data acquisition of bistatic acoustic data. This payload was successfully used in the AUV *Unicorn* for collecting bistatic acoustic scattering data in two shallow-water scattering experiments, as described in Chapter 4. The classification

and regression methods for characterizing target geometry were demonstrated using the real data and data from scattering simulations in Chapters 5 and 6. These techniques, demonstrated successfully on simple target geometries, show great potential for fully autonomous target characterization with all signal processing, classification and confidence estimation conducted on an AUV.

Appendix A

OASES-SCATT Parameters

This appendix includes the OASES and SCATT configurations necessary for replicating the simulations described in this thesis. This includes oast .dat files, oast3 .dat files and target parameters for spherical targets, cylindrical targets, and bottom ripple patches. The .trf generation code can be run in bash after installing Scatt and Oases packages.

A.1 BayEx'14 Simulations

Below are the files, bash code and parameters used for generating sphere and cylinder scattered fields to match the BayEx'14 experiment conditions.

A.1.1 oast file: bayex.dat

```
oast data file0for space free, and source at 3_60 deg
N P E
8000 8000 1 0

9
0 340 0 0 0 0.0012 0 0
0 1524 0 0 0 1.0 0 0
1 1525 0 0 0 1.0 0 0
3 1528 0 0 0 1.0 0 0
5 1530 0 0 0 1.0 0 0
6.5 1530 0 0 0 1.0 0 0
7.5 1575 0 1 1.5 1.7 0 0
8.5 1800 0 0.1 0.2 1.8 0 0
11 1800 0 0.1 0.2 1.8 0 0
```

```
3
0 11 100 41
1763 1763
-1 1 1
0 0.06 20 0.012
0.5 6 0 0 1 0
```

A.1.2 oast3 file: bayex_sca.dat

```
oast3 data file free for 3_60 deg
N r d J f
8000 0 0.0

9
0 340 0 0 0 0.0012 0 0
0 1524 0 0 0 1.0 0 0
1 1525 0 0 0 1.0 0 0
3 1528 0 0 0 1.0 0 0
5 1530 0 0 0 1.0 0 0
6.5 1530 0 0 0 1.0 0 0
7.5 1575 0 1 1.5 1.7 0 0
8.5 1800 0 0.1 0.2 1.8 0 0
11 1800 0 0.1 0.2 1.8 0 0

100 20
3
0 11 100

1400 1E8

-1 1 1 1
0.0 0.0012 51
```

A.1.3 Target files

sphere.dat

```
0.3
0.0153
7975
5773 0.01
3100 0.02
1.2
340 0.01
```

cylinder.dat

```
0.1524
0.1524
0.9144
```

A.1.4 Sphere .trf generation code

```
oast bayex
sphcvs_3d -fluid bayex 32 1024 < sphere.dat
oast3 bayex_sca bayex
```

A.1.5 Cylinder .trf generation code

```
oast bayex
vsccvs -rigid -trapezoid bayex 32 1024 30 24 90 < cylinder.dat
oast3 bayex_sca bayex
```

A.2 Massachusetts Bay Simulations

A.2.1 oast file: mbay.dat

```
oast data file0for space free, and source at 3_100 deg
N P E
8000 8000 1 0

8
0 340 0 0 0 0.0012 0 0
0 1500 0 0 0 1.0 0 0
1 1500 0 0 0 1.0 0 0
6 1500 0 0 0 1.0 0 0
7 1500 0 0 0 1.0 0 0
14 1500 0 0 0 1.0 0 0
15 1800 0 0.1 0.2 1.8 0 0
17 1800 0 0.1 0.2 1.8 0 0

3
0 11 100 41
2154 2154
-1 1 1
0 0.1 20 0.02
```

```
0.5 6 0 0 1 0
```

A.2.2 oast3 file: mbay_sca.dat

```
oast3 data file free for 3_100 deg
N r d J f
8000 0 0.0

8
0 340 0 0 0 0.0012 0 0
0 1500 0 0 0 1.0 0 0
1 1500 0 0 0 1.0 0 0
6 1500 0 0 0 1.0 0 0
7 1500 0 0 0 1.0 0 0
14 1500 0 0 0 1.0 0 0
15 1800 0 0.1 0.2 1.8 0 0
17 1800 0 0.1 0.2 1.8 0 0

100 20
3
0 11 100

1400 1E8

-1 1 1 1
0.0 0.002 51
```

A.2.3 Target file, cylinder.dat

```
0.2286
0.2286
1.5
1000
1300 0.02
```

A.2.4 Cylinder .trf generation code (run in bash after installing Scatt and Oases packages)

(Replace "$pitch" with desired target rotation. Values [0,5,...,180] were simulated for the analysis in Chapter 6)

```
oast mbay
vsccvs -fluid -trapezoid mbay 32 1024 30 $pitch 90 < cylinder.dat
oast3 mbay_sca mbay
```

A.3 Ripple Field Simulations

A.3.1 oast file: deepaniso.dat

```
oast data file0for space rough, and source at 30_100 deg
N J E C P
1000 1000 1 0

6
0 340 0 0 0 0.0012 0 0
1 1500 0 0 0 1.0 0 0
97 1500 0 0 0 1.0 0 0
99.5 1500 0 0 0 1.0 0 0
100 1800 0 0.1 0.2 1.8 0 0
101 1800 0 0.1 0.2 1.8 0 0

30
0 110 100 41
2615 2615
-1 1 1
0 0.1 20 0.02
0 101 5 20
30 90 3
0.50 4 512 512 20 20
```

A.3.2 oast3 file: deepaniso_sca.dat

```
oast3 data file rough for 30_100 deg
N r d f
1000 0 0.0

6
0 340 0 0 0 0.0012 0 0
1 1500 0 0 0 1.0 0 0
97 1500 0 0 0 1.0 0 0
99.5 1500 0 0 0 1.0 0 0
100 1800 0 0.1 0.2 1.8 0 0
101 1800 0 0.1 0.2 1.8 0 0
```

```
100 20
30
0 110 100

1400 1E8

-1 1 1 1
0.0 0.002 51
```

A.3.3 Target file, rough.dat

Replace $< gamma >$ with the desired anisotropy angle.

```
512
512
20
20
2
0.1
<gamma>
0.1
3
1
```

A.3.4 Rough patch .trf generation code for RGJ power spectrum

```
oast deepaniso
fvdct deepaniso
mp2 -f deepaniso_mp < rough.dat
fvpcvs deepaniso_mp.dat deepaniso.dct
oast3 deepaniso_sca deepaniso_mp_deepaniso
```

Appendix B

Alternative Feature Spaces

In addition to the angularly dependent feature space discussed in Chapters 4 and 5, two more complex feature mapping schemes were explored: a cylindrical representation described by values r_{step}, z_{step}, and θ_{step}, and a representation selected via k-means clustering of the differences in amplitude in the 3D scattered field.

B.1 Uniform feature space

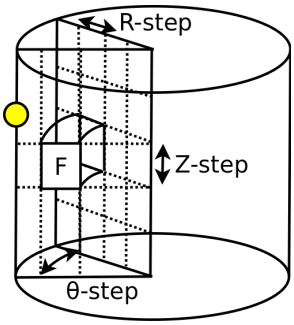

Figure B-1: Uniform feature space geometry. Values of r_{step}, z_{step} and θ_{step} are selected using a reducing grid search.

The simpler of the two features space representations is shown in Figure B-1. The space between the source and target is broken into cells that measure r_{step} x z_{step} x θ_{step}. Each example vector, (x_i, y_i), is constructed by mapping each geometric location that has been sampled by the AUV, (r_s, z_s, θ_s) and its associated value A_s, to a feature number F_n using equation (B.1) and labelled based on class. The feature number is calculated as a function

of the location of the sample (r_s, z_s, θ_s) and step sizes of range, depth, and azimuth and maximum depth.

$$\begin{aligned} F_n &= \lfloor \tfrac{z_s}{z_{step}} \rfloor n_{max,a} + \lfloor \tfrac{r_s}{r_{step}} \rfloor n_{max,\theta} n_{max,z} + \lfloor \tfrac{\theta_s}{\theta_{step}} \rfloor + 10 \\ n_{max,\theta} &= 2\pi/\theta_{step} \\ n_{max,z} &= z_{max}/z_{step} \end{aligned} \quad . \tag{B.1}$$

When multiple samples are collected from the same feature, the median amplitude is taken. For example, if there are three samples at points that map to feature F_n, the value A_n will be the median of the three amplitude values. This calculation is performed for each geometric point the AUV has sampled, such that the feature vector is composed of a number of feature-value pairs and the label y_i becomes the anisotropy angle.

$$\begin{aligned} x_i &= \{[F_1, A_1], ..., [F_N, A_N]\} \\ y_i &= \begin{cases} 1 \, if \, sphere \\ -1 \, if \, cylinder \end{cases} \end{aligned} \quad . \tag{B.2}$$

This is a rapid calculation that can easily be performed on an AUV. The values of parameters that describe the feature space, $\delta = \{r_{step}, z_{step}, \theta_{step}\}$, are selected using the process shown in Algorithm 4 in a design of experiment reducing grid search similar to that described by Staelin in "Parameter Selection for Support Vector Machines"[49] for the purposes of selecting SVM input parameters.

Algorithm 4 Calculate δ^*

$i \leftarrow 0$
$\mathbf{r_{step,0}} \leftarrow [r_{step,0,min}, r_{step,0,min} + (r_{step,0,max} - r_{step,0,min})/2, r_{step,0,max}]$
$\boldsymbol{\theta_{step,0}} \leftarrow [\theta_{step,0,min}, \theta_{step,0,min} + (\theta_{step,0,max} - \theta_{step,0,min})/2, \theta_{step,0,max}]$
$\mathbf{z_{step,0}} \leftarrow [z_{step,0,min}, z_{step,0,min} + (z_{step,0,max} - z_{step,0,min})/2, z_{step,0,max}]$
while $(max(\mathbf{r_{step,i}}) - min(\mathbf{r_{step,i}}) > 1$ **and** $max(\mathbf{z_{step,i}}) - min(\mathbf{z_{step,i}}) > 1$ **and** $max(\boldsymbol{\theta_{step,i}}) - min(\boldsymbol{\theta_{step,i}}) > 1$ **and** $\delta^*_{\mathbf{i}} != \delta^*_{\mathbf{i-1}}$ **do**
  $[r^*_{step,i}, z^*_{step,i}, \theta^*_{step,i}] = FindBestPoint(\mathbf{r_{step,i}}, \mathbf{z_{step,i}}, \boldsymbol{\theta_{step,i}}))$
  $\delta^*_{\mathbf{step,i}} = [r^*_{step,i}, z^*_i, \theta^*_{step,i}]$
  $\mathbf{r_{step,i+1}} = RefineGrid(\mathbf{r_{step,i}}, r^*_{step,i})$
  $\mathbf{z_{step,i+1}} = RefineGrid(\mathbf{z_{step,i}}, z^*_{step,i})$
  $\boldsymbol{\theta_{i+1}} = RefineGrid(\boldsymbol{\theta_{step,i}}, \theta^*_{step,i})$
  $i = i + 1$
end while

Algorithm 5 $FindBestPoint(\mathbf{r}, \mathbf{z}, \boldsymbol{\theta})$

$V_{max} \leftarrow 0$
for r in $\mathbf{r_i}$ **do**
  for z in $\mathbf{z_i}$ **do**
    for θ in $\theta_\mathbf{i}$ **do**
      $V = Value(r, z, \theta)$
      if $V > V_{max}$ **then**
        $r^* \leftarrow r$
        $z^* \leftarrow z$
        $\theta^* \leftarrow \theta$
      end if
    end for
  end for
end for
return $[r^*, z^*, \theta^*]$

Algorithm 6 $RefineGrid(\mathbf{d_i}, d_i^*)$

$\Delta = max(\mathbf{d_i}) - min(\mathbf{d_i})$
if $d_i^* + \Delta/2 \leq max(\mathbf{d_i})$**and** $d_i^* - \Delta/2 \geq min(\mathbf{d_i})$ **then**
  $\mathbf{d_{i+1}} = [d_i^* - \Delta/4, d_i^*, d_i^* + \Delta/4]$
else if $d_i^* + \Delta/2 \geq max(\mathbf{d_i})$**and** $d_i^* - \Delta/2 \geq min(\mathbf{d_i})$ **then**
  $\mathbf{d_{i+1}} = [d_i^* - \Delta/4, d_i^*, d_i^* + \Delta/2]$
else if $d_i^* + \Delta/2 \leq max(\mathbf{d_i})$**and** $d_i^* - \Delta/2 \leq min(\mathbf{d_i})$**and** $d_i^* - \Delta/2 \geq 0$ **then**
  $\mathbf{d_{i+1}} = [d_i^* - \Delta/2, d_i^*, d_i^* + \Delta/4]$
else
  $\mathbf{d_{i+1}} = [d_i^* - \Delta/4, d_i^*, d_i^* + \Delta/4]$
end if
return $\mathbf{d_{i+1}}$

B.2 K-means

The second feature space was selected using unsupervised machine learning in the form of k-means clustering to determine the geometrical mapping for r, z, θ location to feature numbers. Each point in the scattered field was first represented as a location $x_i = [x_i, y_i, z_i]$ with an associated value dA, where dA is the difference in amplitude between the sphere and cylinder data at point x. Algorithm 7 describes the process used to determine the mapping of the points, $\mathbf{X} = \{\mathbf{x_1}, ..., \mathbf{x_N}\}$, to a set of centers, $\mathbf{M} = \{\mathbf{m_1}, ..., \mathbf{m_K}\}$ using the following cost function:

$$c(\mathbf{x_i}, \mathbf{m_j}) = w_0(||\mathbf{x_i} - \mathbf{m_j}||) + w_1(||dA_{xi} - dA_{mj}||) \tag{B.3}$$

Algorithm 7 K-means feature selection

$C^* = 10000000$
for $l = 0$ **to** 100 **do**
  Randomly select K random cluster means $\mathbf{M(0)} = \{\mathbf{m_1}, \ldots, \mathbf{m_K}\}$
  repeat
    Assignment: Assign each data point $\mathbf{x_i}$ to the closest cluster mean $\{\mathbf{m_1}, \ldots, \mathbf{m_K}\}$:

$$C(i) = \underset{m_k}{\operatorname{argmin}}(c(\mathbf{x_i}, \mathbf{m_k})), s.t. 1 < k < K \tag{B.4}$$

    Update: Minimize the total variance for the cluster C with respect to $\{\mathbf{m_1}, \ldots, \mathbf{m_K}\}$, yielding a new set of means $\mathbf{m(l)}$.
  until The assignments do not change.
  if $\sum_{0<i<K} C(i) < C^*$ **then**
    $\mathbf{M}^* = \mathbf{M(l)}$
    $C^* = \sum_{0<i<K} C(i)$
  end if
end for
return $\mathbf{M}^*, C^*$

B.3 Comparison of feature spaces

The angular feature space outperformed the uniform and k-means feature spaces in all tested metrics. Figure B-2 shows plots comparing the performance of the three formulations. The extra dimensionality of the uniform feature space meant that a radial basis function kernel was required in training, adding significant complexity and decreasing robustness to

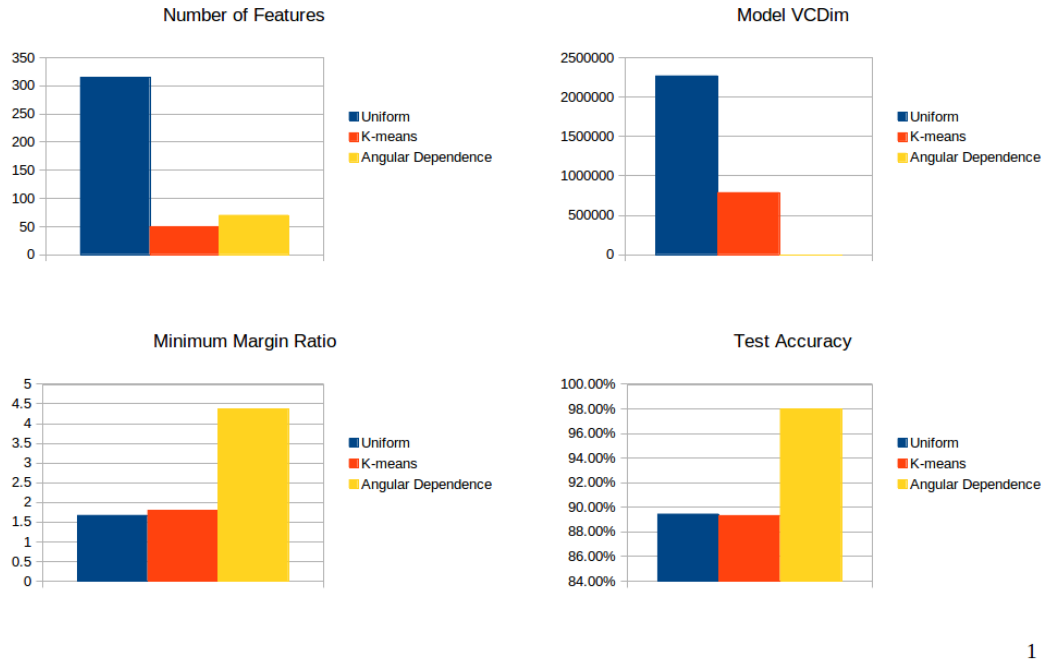

Figure B-2: Comparison of performance of three tested feature spaces.

navigation error. The K-means feature space was highly dependent on a match between the model used to train the feature space and the eventual data being classified. This resulted in poor robustness to small changes in environment and target parameters. As observed in Ch. 2, the clearest features in the bistatic scattered field are azimuthally dependent minima and maxima in the radiation pattern. These features are best captured by the angularly dependent feature space, which gives the least complexity and best classification performance of the tested feature selection methods.

Appendix C

Software for SVM Example Vector Set Generation

To facilitate the creation of SVM files for model creation, validation and testing from real or simulation data sets, the AutoGeneration code was developed. This software uses a SQLLite database backend, and performs all functions to go from a configuration to the independent training, validation and testing example vector sets used in this thesis. In simulation, the process uses configuration information to first generate appropriate OASES-SCATT simulation models then sample that data into example sets. For real data, an amplitude file describing the data collected by the AUV is written either in real time or simulation from MOOS-IvP processing of acoustic data files. This file is then used to generate training, validation and test examples.

C.1 Simulation

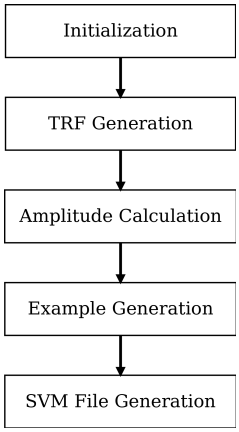

Figure C-1: Autogeneration process to produce SVM files for simulation data.

Figure C-1 shows the steps to produce the SVM files used in training and analysis using scattering simulation. The process is first initialized using a set of configuration files, OASES-SCATT called to generate azimuthal fourier order files based on the configuration, the scattering amplitude grid calculated, examples formed and finally SVM files written using independent example vector sets.

C.1.1 Initialization

From a terminal, the python script *runScriptTRFtoSVM.py* is called with two to five inputs: a configuration flag, a database name, and three optional True/False falgs that can circumvent parts of the SVM file generation procedure for expediency. For example:

```
> python runScriptTrftoSVM.py bayex14 bayexdata
```

would run the script using the "bayex14" configuration and put the data into the database "dbs/bayexdata". This database is created if it does not already exist.

The script *runScriptTrftoSVM* used hte configuration flag to determine which definitions files to use in the generation of scattering models with OASES-SCATT, the formation of test example vectors nad the compilation of training, test and validation data sets. Six file types define this set of data:

1. Geo files: describes the target.

2. Oast files: describes the environment and parameters for OASES-SCATT simulations.

3. Source file: defines the source frequency, range, and depth.

4. SVM configuration file: includes parameters for forming example vectors from data and training, validation and test sets/files from example vectors. Also describes if the data sets being created are for classification or regression and what the regression variable is.

5. Positive class file: defines the target characteristics that constitute a positive class label for classification.

6. Rough files: defines parameters for the addition of rough bottom scattering to target scattering if desired.

An example configuration block for the "bayex14" flag in *runScriptTRFtoSVM.py* is shown below:

```
if gen ==’bayex14’: #Based on actual BAYEX experiment parameters
     geo_vec = [’sphere_fluid_BAYEX.def’,’trapezoid_rigid_BAYEX.def’]
     rough_vec=[]
     src_file=’src_BAYEX.def’
     pos_class_file=’pos_class_sphere.def’
     svm_file=’svmparam_angdep_9deg.def’
     oast_file=’OastData_SVM_bayex.def’
```

Geometry File:

```
#variable definitions for fluid sphere
shape =’sphere’
space =’free’
type =’fluid’
Radius=.3
Thickness=.0153 #shell thickness
RhoShell=7975 #density of hte shell
Cp=5773 #speed of sound
Ap=.01
Cs=3100
As=.02
RhoFluid=1.2
CpFluid=340
```

```
ApFluid=.01
pitch=0
roll=0
buried=0
```

Source File:

```
freq=[8000]
sr=[60]
sd=[3]
```

SVM File:

```
#example input file for svm parameters
astep=9#azimuth step (deg)
nSinF=10 #max number of points sampled per feature
nF=40 #number of features sampled
nEx = 6000#number of examples to generate
dec_train=.5#percentage of examples to be used for training
dec_val=0.25#percentage of examples to be used for validation
sigma=0#standard dev. for zero-mean offset in x, y, z directions
```

OAST File:

```
COFF=0 #integration contour offset
DFRC=0.0 #freq increment for wide band
NL=6 #number of layers
layers =[[0,340,0,0,0,.0012,0,0],[0,1524,0,0,0,1.0,0,0],
[1,1525,0,0,0,1.0,0,0],[3,1528,0,0,0,1.0,0,0],
[5,1530,0,0,0,1.0,0,0],[6,1530,0,0,0,1.0,0,0],
[6.5,1575,0,1,1.5,1.7,0,0],[7.3,1800,0,0.1,0.2,1.8,0,0],
[11,1800,0,0.1,0.2,1.8,0,0]]

CC=1528 #compression wave speed: velocity, used to calc phase velocity
RD1=0 #first receiver depth
RD2=11 #last receiver depth
IR=41 #plot output increment
NR=100 #number of receivers
NW=-1 #number of wavenumber samples
IC1=1
IC2=1
RANGEPLOT='0 0.1 20 0.02'
TLOSSAXES='0.03077 4 0 0 1.06 0'
```

```
IF=1
ST=100 #source type
FO=20 #max fourier order
nSInR=51#number of samples in range
tarLay=7
maxd=5#max depth in m for sampling
roughLay=5
```

Positive Class File

```
#pos_class
space='free'
shape='sphere'
types='fluid'
geoid=-1
roughid=-1
```

Once the definitions files are selected the information from those files is checked and entered into appropriate tables in the database. Where multiple targets, environments or sources are specified, multiple data entries are made and used in generation of simulation models.

C.1.2 TRF Generation

With all configuration data entered into the database, the information iused to write properly-formatted files for use in generation of target scattering models with OASES-SCATT. *writeOastFiles.py* takes in the database name and writes the *oast.dat*, $oast_sca.dat$ and *target.dat* files for OASES-SCATT input (described in Appendix A). Once these files are in place, the sequence of OASES-SCATT commands to produce the azimuthal fourier order "TRF" file is run from $getTRFFiles.py$. This function uses the target parameters from the database to determine which bash script to run. For the example given in initialization, it would run free sphere model generation and free trapezoid model generation, setting up the commands to run $getSphereTarget.sh$ and $getFreeTarget.sh$. Different scripts are run for spheres versus other shapes, for free targets versus partially buried targets, and for rough patch scattering modelling.

Free sphere model generation script, $getSphereTarget.sh$:

```
#!/bin/bash

#first input: file root
#second input: geo root
#third input: target shape
#fourth input: target type
#fifth: trf file
#sixth: pitch
#seventh: roll
#eigth: buried depth (0 = 50%)
#ninth: database name (folder under trfs)

pushd temp/

oast $1
#gets spherical target data for use with oast3
which sphcvs_3d
sphcvs_3d -$4 $1 32 1024 < $2.dat
oast3 $1'_sca' $1

trffile=$5'.trf'

cp $1'_sca.trf' '../trfs/'$9'/'$trffile

popd
```

Free shape model generation code, *getFreeTarget.sh*:

```
#!/bin/bash

#get non buried target using vsccvs

#first input: file root
#second input: geo root
#third input: target shape
#fourth input: target type
#fifth: destination filename (timestamp)
#sixth: pitch
#seventh: roll
#eigth: buried depth (0 = 50%)
#ninth: database name (folder under trfs)

pushd temp/
oast $1
which vsccvs
vsccvs -$4 -$3 $1 32 1024 30 $6 $7 < $2'.dat'
```

```
oast3 $1'_sca' $1

#copy trf files:

trffile=$5'.trf'

cp $1'_sca.trf' '../trfs/'$9'/'$trffile

popd
```

The configuration used to make each scattering model is stored in the database and associated with the appropriate trf primary key.

C.1.3 Amplitude Extraction

The python script next calls on matlab to read the binary .trf files and calculate the scattering amplitudes form the contained azimuthal fourier orders at a grid in range, depth, and azimuth. That grid is written to a plain text file. Once all .trf files are converted in this way, the amplitudes are read from the output files into tables in the database.

C.1.4 Example Generation

At this point in the process, the database contains the amplitude "grids" of interest for all SVM data sets and all the meta information used to create them. The next step is to convert that data into example vectors that may be used to form independent training, validation and test sets. The process here is for the angularly dependent feature space described in Section 5.1.2, and is slightly different for the alternative feature spaces described in Appendix B. The parameters used to create example vectors using the angularly dependent feature space include *astep* (feature space step size in degrees), $NSinF$ (approximate number of points sampled per feature), nEx (total number of examples to generate).

Each example vector is pseudo-randomly generated using a "seed" value. For each feature, either $NSinF$, $NSinF - 1$ or $NSinF + 1$ random points are sampled, mimicking the behavior observed in the real-world experiments.

The final locations and amplitudes are mapped to feature numbers, and the median amplitude taken for each feature. A string of feature-value pairs is written to the database along with the seed, amplitude key, and svm configuration key. nEx such examples are

formed from each amplitude grid.

C.1.5 SVM File Generation

In the SVM File generation step, each example is assigned a label, grouped into the training, validation or test set and written to file. The values of *dec_train* and *dec_val* define the percentage of the example vectors that are used in training, validation and test sets. The label is determined for classification by the positive class file and for regression using the configured regression variable. The database was used to determine the label of each example vector. $writeSVMFile.py$ is then used on each set to write training, validation and test files used for training and analysis. These files are properly formatted for use with SVM-Light.

C.2 Real Data

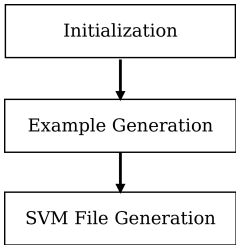

Figure C-2: Autogeneration process to produce SVM files for real data.

Generating SVM example vector sets from real data follows a slightly different procedure. Before the data sets could be converted to examples for training and analysis, the mapping of acoustic amplitudes to sampling locations had to be synthesised from the acoustic and navigation data that made up an experimental data set. This was performed either in real time (acoustic amplitudes calculated and written to file along with navigation information as AUV collects the data) or in post-processing (logs are used to replicate the processing that would have occurred in real time) within MOOS-IvP. The resulting file contained the range, depth and azimuthal dependence of the acoustic data collected in the experiment. Figure C-2 shows the process to go from this data to training, validation and test examples. The process is very similar to that for simulation data from example generation onwards. First, the acoustic amplitude data is written to the database. Example vectors are then formed using sets of N sequential amplitude datum as described in Section 5.1.2. Sets of

example vectors are written to SVM files in SVM file generation process identical to that for simulation data.

Bibliography

[1] Hansen et. al. Challenges in seafloor imaging and mapping with synthetic aperture sonar. *IEEE Transactions on Geoscience and Remote Sensing*, 49(10), October 2011.

[2] G.C. Gaunaurd and H. Oberall. Rst analysis of monostatic and bistatic acoustic echoes from an elastic sphere. *J. of the Acoust. Soc. of America*, 73(1), January 1983.

[3] R. H. Hackman and G. S. Sammelmann. Multiple-scattering analysis for a target in an oceanic waveguide. *J. Acoust. Soc. Am.*, 1988.

[4] T. K. Stanton. Sound scattering by cylinders of finite length. i. fluid cylinders. *J. of the Acoust. Soc. of America*, 83(1), January 1988.

[5] T. K. Stanton. Sound scattering by cylinders of finite length. ii. elastic cylinders. *J. of the Acoust. Soc. of America*, 83(1), January 1988.

[6] M. L. Rumerman. Contribution of membrane wave reradiation to scattering from finite cylindrical steel shells in water. *J. of the Acoust. Soc. of America*, 93(1), January 1993.

[7] H. Schmidt and J. Lee. Physics of 3-d scattering from rippled seabeds and buried targets in shallow water. *J. of the Acoust. Soc. of America*, 105(3), March 1999.

[8] MIT LAMSS. *SCATT-OASES3D UserâĂŹs manual*, revision 2 edition. http://lamss.mit.edu/lamss/docs/scatt_manual.pdf.

[9] J. Lee. *Multi-static Scattering of Targets and Rough Interfaces in Ocean Waveguides*. PhD thesis, Massachusetts Institute of Technology, 1999.

[10] K. Baik, C. Dudley, and P. L. Marston. Acoustic quasi-holographic images of scattering by vertical cylinders from one-dimensional bistatic scans. *J. Acoust. Soc. Am.*, 130(6), December 2011.

[11] S. G. Kargl et. al. Acoustic scattering from underwater munitions near a water-sediment interface. *J. Acoust. Soc. Am.*, 129(4), 2011.

[12] K. D. LePage and H. Schmidt. Bistatic synthetic aperture imaging of proud and buried targets from an auv. *IEEE Journal of Oceanic Engineering*, 27(3), July 2002.

[13] J. R. Edwards, H. Schmidt, and K. D. LePage. Bistatic syntehtic aperture target detection and imaging with an auv. *IEEE Journal of Oceanic Engineering*, 26(4), October 2001.

[14] C. Dudley and P. L. Marston. Bistatic synthetic aperture sonar images of penetrable cylinders. *J. Acoust. Soc. Am.*, 125(4), 2009.

[15] Paul Runkle et. al. Multiaspect identification of submerged elastic targets via wave-based maching pursuits and hidden markov models. *J. Acoust. Soc. Am*, 105(2), August 1999.

[16] E. J. Kaminsky and M. Barbu. Classification of cylindrical targets buried in seafloor sediments. *Proc. of IEEE Region 5 Technical Conference, Apr. 20-21. pg. 117-123.*, 2007.

[17] A.Malarkodi, D. Manamalli, G. Kavitha, and G. Latha. Acoustic scattering of underwater targets. *Proceeding of SYMPOL 2013, pg. 127-132.*

[18] F. Ingenito. Scattering from an object in a stratified medium. *J. Acoust. Soc. Am.*, 1987.

[19] J. Heidemann, Y. Wei, J. Wills, A. Syed, and L. Yuan. Research challenges and applications for underwater sensor networking. *IEEE Wireless Communications and Networking Conference, Las Vagas, NV.*, 2006.

[20] General Standards Corporation. 4dsi12, 12-channel 24-bit delta-sigma pmc analog input board. *[Online] vailable: http://www.generalstandards.com/specs/24dsi12_spec.pdf.*

[21] Advantech. Pcm-3363. *[Online] http://downloadt.advantech.com/ProductFile/PIS/PCM-3363/Product%20-%20Datasheet/PCM-3363_DS%2801..15.14%2920140205144952.pdf*, 2014.

[22] Symmetricom. Leading edge technology enables a chip scale atomic clock. *[Online] http://www.ecnmag.com/sites/ecnmag.com/files/legacyimages/WP_LeadingEdgeTechnology_CSAC.pdf*, 2012.

[23] Generic nmea gps receiver. *[Online] Available: http://www.eecis.udel.edu/ mills/ntp/html/drivers/driver20.html.*

[24] Linuxpps. *[Online] http://linuxpps.org/wiki/index.php/Main_Page*, 2013.

[25] A. G. Piersol. Time delay estimation using phase data. *IEEE Transactions on Acoustics, Speech and Signal Processing.*, (3), June 1981.

[26] Sea-Bird Electronics Inc. Microcat c-t recorder, sbe 37-sm. *[Online]. Available: http://www.seabird.com/pdf_documents/Datasheets/37SMbrochureMar14.pdf*, 2014.

[27] Michael Benjamin, Henrik Schmidt, Paul Newman, and John Leonard. Nested autonomy for unmanned marine vehicles with moos-ivp. *Journal of Field Robotics.*, November 2006.

[28] T. Schneider and H. Schmidt. Goby-acomms version 2: extensible marshalling, queuing, and link layer interfacing for acoustic telemetry. *9th IFAC Conference on Manoeuvring and Control of Marine Craft, Arenzano, Italy*, 2012.

[29] S. Petillo and H. Schmidt. Exploiting adaptive and collaborative auv autonomy for detection and characterization of internal waves. *IEEE JOE special issue on Marine Vehicle Autonomy.*, January 2014.

[30] Lubell ll916c underwater speaker. http://www.lubell.com/LL916.html.

[31] F.B. Jensen, W.A. Kuperman, M. B. Porter, and H. Schmidt. *Computational ocean acoustics*. Springer, second edition, 2011.

[32] Vladimir N. Vapnik. *The Nature of Statistical Learning Theory*. Springer, 1995.

[33] T. Joachims. Svm-light main page. *[Online] http://svmlight.joachims.org/*.

[34] T. Hastie, R. Tibshirani, and J. Friedman. *The Elements of Statistical Learning- Data Mining, Inference and Prediction.*, section 7.1, pages 221–222. Springer, second edition, 2009.

[35] T. Joachims. *Making large-Scale SVM Learning Practical. Advances in Kernel Methods - Support Vector Learning.* B. SchÃűlkopf and C. Burges and A. Smola (ed.), MIT-Press, 1999.

[36] Michael B. Porter. The bellhop manual and userâĂŹs guide. *Heat, Light, and Sound Research, Inc. La Jolla, CA, USA. [Online] http://oalib.hlsresearch.com/Rays/HLS-2010-1.pdf.*, January 2011.

[37] M. Zampolli et. al. Low- to mid-frequency scattering from elastic objects on a sand sea floor. *J. of Comp. Acoustics*, 20(2), 2012.

[38] K. L. Williams et. al. Acoustic scattering from a solid aluminum cylinder in contact with a sand sediment: Measurements, modeling, and interpretation. *J. Acoust. Soc. Am.*, 127(6), June 2010.

[39] Y. H. Ji et. al. Multi-static scattering characteristics of submerged objects with experimental investigation. *J. Acoust. Soc. Am.*, 134(5), November 2013.

[40] K.L. Williams and D.R. Jackson. Bistatic bottom scattering: model, experiments, and model/data comparison. *J. Acoust. Soc. Am*, 103(1), January 1998.

[41] C. Bishwajit and K. Haris. Seafloor roughness estimation employing bathymetric systems: An appraisal of the classification and characterization of high-frequency acoustic data. *AIP Conf. Proc.*, 1495(1), November 2013.

[42] Z. Huang, J. Siwabessy, S. Nichol, T. Anderson, and B. Brooke. Predictive mapping of seabed cover types using angular response curves of multibeam backscatter data: Testing different feature analysis approaches. *In Continental Shelf Research*, July 2013.

[43] S. E. Dosso, P. L. Nielsen, and C. H. Harrison. Bayesian inversion of reverberation and propagation data for geoacoustic and scattering parameters. *J. of the Acoust. Soc. of Am.*, 125(5), May 2009.

[44] G. Steininger, J. Dettmer, S.E. Dosso, and C.W. Holland. Trans-dimensional joint inversion of seabed scattering and reflection data. *J. of the Acoust. Soc. of Am.*, 133(3), March 2013.

[45] C.C. De and B. Chakraborty. Model-based acoustic remote sensing of seafloor characteristics. *IEEE TRANSACTIONS ON GEOSCIENCE AND REMOTE SENSING*, 49(10), October 2011.

[46] H.M. Manik. Seabed identification and characterization using sonar. *Advances in Acoustics & Vibration*, 2012, 2012.

[47] K.M. Becker. Effect of various surface-height-distribution properties on acoustic backscattering statistics. *IEEE Journal of Oceanic Engineering*, 29(2), April 2004.

[48] Huo Guanying, Li Qingwu, Wang Min, Fan Xijian, and Fan Xinnan. Side-scan sonar image despeckling based on bayesian estimation in curvelet domain. *Chinese J. of Sci. Instrument*, 32(1), January 2011.

[49] Carl Staelin. Parameter selection for support vector machines. *HP Laboratories Israel. Ref No: HPL-2002-354.*, November 2003.